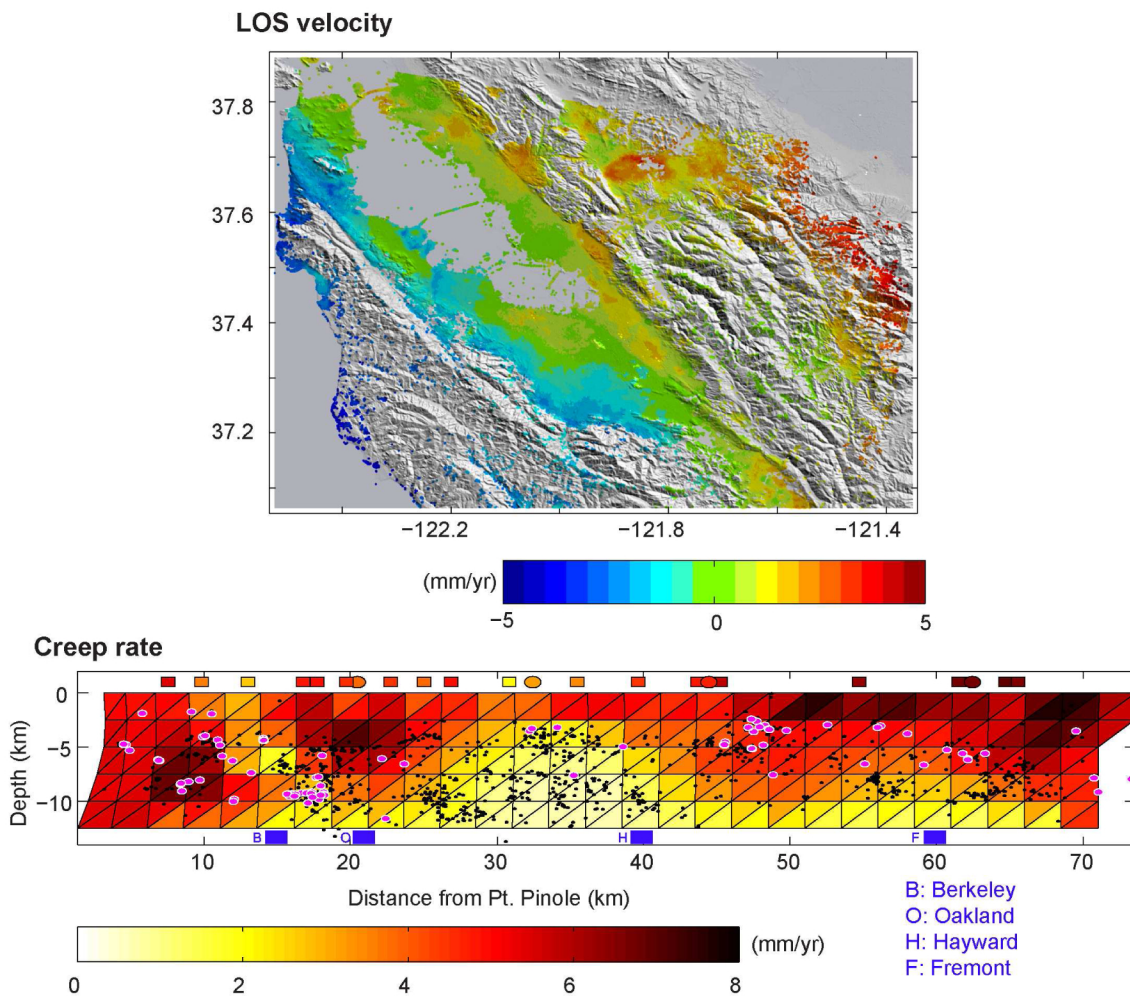


Berkeley Seismological Laboratory



Annual Report
July 2011 - June 2012

Berkeley Seismological Laboratory
Annual Report
July 2011 - June 2012

Cover Picture

From Research Section 4: This model of creep, movement on the Hayward Fault with no accompanying earthquake, suggests that the creep rate near the surface is faster along the southern section of the fault. At greater depth, the situation is reversed, with higher rates in the north than in the south. Given the fact that most of the Hayward fault has accumulated a deficit of 30%-90% of its long-term slip budget, we estimate that seismic moment for a M_w ~6.3-6.8 has accumulated since the last big event in 1868.

Contents

1	Director's Report	1
1	Highlights	1
2	Facilities Review	2
3	BSL Personnel News	4
4	Acknowledgements	4
2	Research Studies	5
1	Episodic Tremors Highlight Slow Slip Events in Central California	6
2	Searching for Small Deformation Signals in Laser Strainmeter Data Associated with Seismic Tremor in Parkfield	8
3	TremorScope: Imaging the Deep Workings of the San Andreas Fault	10
4	Time-dependent Model of Creep on the Hayward Fault from Joint Inversion of 18 Years of InSAR and Surface Creep Data	12
5	Landslide Risk Assessment (LSRA): GPS Instrumentation and Remote Sensing Study of Slope Movement in the Berkeley Hills, California.	14
6	Investigating Fault Slip and Rheology Along the San Andreas Fault in the San Juan Bautista Region	16
7	Aseismic Slip and Fault Interaction from Repeating Earthquakes in the Loma Prieta Aftershock Zone	18
8	Surface Slip during Large Owens Valley Earthquakes from EarthScope Lidar	20
9	Testing the Temporal Persistence of Slip Rate Along the Little Lake Fault, Eastern California Shear Zone	22
10	Examining the Mechanical Behavior and Evolution of the Southern San Andreas Fault System through Determination of Late Quaternary Slip Rates and Distinct Element Simulations	24
11	Investigating Fault Slip Budget in the Mendocino Triple Junction	26
12	Incipient Faulting near Lake Pillsbury, CA	28
13	Measurements of PBO Borehole Seismometer Orientations	30
14	Spatiotemporal Behaviors in Earthquake Multiplets at the Geysers Geothermal Field, CA	32
15	A systematic analysis of seismic moment tensor for seismicity at The Geysers Geothermal Field, California	34
16	Joint Inversion of Seismic and Geodetic Data for the Source of the 4th March 2010 M_w 6.3 Jia-Shian, SW Taiwan, Earthquake	36
17	Deciphering the Mystery of the Great Indian Ocean Earthquakes	38
18	Source Spectral Variation and Yield Estimation Derived from High Frequency P and S Coda	40
19	Regional Moment Tensor Inversion for Shallow Sources: the Effects of Free-Surface Vanishing Traction	42
20	ShakeAlert: A Unified EEW System for California	44
21	ElarmS Earthquake Early Warning	46
22	Earthquake Early Warning with GPS Data	48
23	GPS Rapid Response to Moderate Earthquakes: A Case Study of the Alum Rock Earthquake	50
24	Using Smartphones to Detect Earthquakes	52
25	Probing the Deep Rheology of Tibet: Constraints from 2008 M_w 7.9 Wenchuan, China Earthquake	54
26	Global Waveform Tomography with the Spectral Element Method: A Second-Generation Upper-Mantle Model	56
27	The DNA12 Seismic Velocity Model	58
28	Trust but Verify: a spot check for the new stratified model of upper mantle anisotropy beneath North America	60
29	3-D Seismic Velocity Structure of the Hawaii Hotspot from Joint Inversion of Body Wave and Surface Wave Data	62

30	Azimuthal anisotropy in the Pacific upper mantle	64
31	Anisotropic Upper Mantle Shear-wave Structure of East Asia from Waveform Inversion	66
32	An Exceptionally Large ULVZ at the Base of the Mantle near Hawaii	68
33	Do "double SS precursors" mean double discontinuities?	70
34	Inversion of Receiver Functions without Deconvolution	72
35	Surface-Wave Methods for Monitoring Subsurface Properties in Permafrost Soils	74
3	BSL Operations	76
1	Berkeley Digital Seismic Network	78
2	California Integrated Seismic Network	88
3	Northern Hayward Fault Network	94
4	Parkfield Borehole Network (HRSN)	103
5	Bay Area Regional Deformation Network	114
6	Northern California Earthquake Data Center	120
7	Data Acquisition and Quality Control	130
8	Northern California Earthquake Monitoring	136
9	Outreach and Educational Activities	142
	Glossary	144
	Appendix I Publications, Presentations, Awards, and Panels 2011-2012	146
	Appendix II Seminar Speakers 2011-2012	156
	Appendix III Organization Chart 2011-2012	159

Chapter 1

Director's Report

1 Highlights

It is a great pleasure to present this year's Berkeley Seismological Laboratory (BSL) Annual Report. This is my first report as Director of the lab and it is exhilarating to see the wide range of BSL activities captured in these pages. The BSL today fosters both an active solid Earth research program and a cutting-edge geophysical observing facility. Spanning both of these realms, BSL provides an environment in which the extramural research program is strengthened and broadened by the facility, and the facility continues to push the boundaries of terrestrial observations in response to research needs. The contributions to this report are divided along these two lines. The research accomplishments are covered in Chapter 2, and progress in the development of our facilities is contained in Chapter 3. But first, I would like to highlight some of this year's activities.

The beginning of a new directorship provides an opportunity to reaffirm the BSL mission. After a review of the BSL's goals, priorities, and activities, we have developed the following mission statement consisting of four central tenets.

BSL's Mission: Sound science, serving society

Fundamental research: *Support fundamental research into all aspects of earthquakes, solid earth processes and their effects on society through the collection, archival and delivery of high quality geophysical data and through fostering a dynamic research environment that connects researchers across disciplines to geophysical observation systems.*

Hazard information: *Provide robust and reliable real-time data and information on Northern California earthquakes to government, public and private institutions, and to the public, in partnership with the US Geological Survey, CalEMA and other collaborating institutions.*

Broad education: *Enable the broad consumption of earthquake information and solid earth science through education and outreach to all sectors of society. Educate and train students at all levels through classes and research opportunities.*

Professional operation: *Create a productive professional working environment to enable efficient and robust operation and management of the geophysical facilities and career development of the staff and students.*

The basic research covered in Chapter 2 spans many topics in geophysics, seismology and tectonics. There are a total of 35 two-page summaries that range from micro-earthquake studies along the well-established San Andreas Fault to incipient faulting elsewhere; from aseismic slip on faults to great earthquake studies; from the structure of the deepest mantle to the properties of permafrost; from global seismic velocity structure to regional rheology. In addition to the two-page summaries, you will also find a list of publications and presentations about this research in Appendix I.

One of the exciting new developments during 2011-12 was a two-pronged effort to design and build a full prototype earthquake early warning system for California. This is being done thanks to generous funding by the Gordon and Betty Moore Foundation. In partnership with Caltech, the University of Washington and the USGS, we are now developing new algorithms to rapidly characterize the extent of faulting during large magnitude earthquakes. This will complement the current point-source methodologies that are the basis of the demonstration warning system that is running today. The second prong is the creation of BSL Earthquake Research Affiliates Program. It is designed to nurture partnerships between the BSL and the users of earthquake information. The program allows us to develop hazard products, including early warning, that are designed to fulfill the specific needs of private and public institutions and companies. The program currently has four members who are receiving earthquake alerts from the demonstration system. They are evaluating how their institution would respond to earthquake alerts in the future to reduce the impacts of earthquakes. You can find more information on the early warning effort in Chapter 2, Sections 20, 21, 22, 23, and 24.

The Gordon and Betty Moore Foundation has also funded our Tremorscope project. This project will in-

stall and operate a network of eight high-quality stations in the Cholame region south of Parkfield, CA, where seismic tremor has been found in the deep roots of the San Andreas fault zone. The network will be made up of four surface stations with broadband seismometers and accelerometers, and four borehole installations with geophones downhole, as well as digital broadband sensors and accelerometers. By the end of June 2012, all but two of the 8 stations were permitted, and the first two surface stations were installed and sending data. We evaluated data from these two sites to develop improvements to installation procedures before installing the other two surface sites. Over the next year, we expect to install and begin operating the remaining surface stations, as well as the borehole sites.

The BSL received significant funding from the USGS, in the framework of the American Recovery and Reinvestment Act (ARRA), to upgrade the recording systems at many of the Berkeley Digital Seismic Network (BDSN) broadband and borehole stations over the past three years. These upgrades are now completed at both our broadband and borehole stations. With the exception of two borehole sites installed under the auspices of Caltrans and several locations where we digitize other geophysical parameters such as electric and magnetic field strength, we now have new data loggers at all stations. All the broadband/strong motion sites now have some model of the Quanterra Q330 data logger, and the borehole sites have the 8-channel Basalt data logger.

In the last year, the BSL also completed work under the ARRA program to upgrade the Bay Area Regional Deformation (BARD) network's infrastructure, processing flow, and website. This included upgrading equipment at nearly half of the BARD GPS stations and installing six new stations (GASB, JRSC, MCCM, MNRC, PTRO, and WDCB), all co-located with BDSN seismometers. All BARD stations are now streaming data at 1 Hz. The upgraded receivers allowed us to make our real-time GPS data streams available more easily to the wider community. The real-time data streams also facilitate our in-house, real-time, high-rate processing of GPS data to produce station displacement estimates that can be used to inform real-time earthquake products, including Earthquake Early Warning systems. Daily processing and time-series generation for BARD backbone stations was re-established and the BARD webpage upgraded to provide more information (<http://earthquakes.berkeley.edu/bard>). More information about BARD can be found in Chapter 3, Section 5.

2 Facilities Review

The Berkeley Seismological Laboratory (BSL) is an Organized Research Unit (ORU) on the UC Berkeley cam-

pus. Its mission is unique in that, in addition to research and education in seismology, geophysics, and earthquake-related science, it is responsible for providing timely information on earthquakes to the UC Berkeley constituency, to the general public, and to various local and state governments, and private organizations. The BSL is therefore both a research center and a facility/data resource, which sets it apart from most other ORUs. A major component of our activities is focused on developing and maintaining several regional observational networks, and participating, along with other agencies, in various aspects of the collection, analysis, archival, and distribution of data pertaining to earthquakes, while maintaining a vigorous research program on earthquake processes and Earth structure. In addition, the BSL staff spends considerable time on public relations activities, including tours, talks to public groups, response to public inquiries about earthquakes, and an informational web presence (<http://earthquakes.berkeley.edu/>).

UC Berkeley installed the first seismograph in the Western Hemisphere at Mount Hamilton (MHC) in 1887. Since then, it has played a leading role in the operation of state-of-the-art seismic instruments and in the development of advanced methods for seismic data analysis and interpretation. Notably, the installation, starting in 1927, of Wood-Anderson seismographs at four locations in Northern California (BKS, ARC, MIN, and MHC) allowed the accurate determination of local earthquake magnitude from which a unique historical catalog of regional earthquakes has been maintained to this day, providing crucial input to earthquake probabilities studies.

Over the years, the then Berkeley Seismographic Stations (BSS) continued to keep pace of technological improvements. The first centrally telemetered network using phone lines in an active seismic region was installed by BSS in 1960. The BSS was the first institution in California to operate a 3-component "broadband system" (1963). It played a major role in the early characterization of earthquake sources using "moment tensors" and source-time functions. The BSS also made important contributions to the early definitions of detection/discrimination of underground nuclear tests and, jointly with UCB Engineering, to earthquake hazards work.

Starting in 1986, the BSS acquired four state-of-the-art broadband instruments (STS-1), while simultaneously developing PC-based digital telemetry. These two developments laid the groundwork for the modern networks we operate today. As telecommunication and computer technologies made rapid progress, in parallel with broadband instrument development, paper record reading was abandoned in favor of automated analysis of digital data. One paper-based helicorder does remain operational, primarily for the press and visitors to view.

Today, the BSL's networks can be divided into three

groups of instrumentation that are deployed at a total of 70 sites across central and northern California. The instrumentation types predominantly consist of broadband plus strong motion seismic, borehole seismic, and GPS, and are often co-located when appropriate. Data from all instrumentation streams continuously into the BSL's real-time monitoring system providing for earthquake notification and characterization, and also into the archive where it can be accessed immediately by researchers around the world for scientific study.

The Berkeley Digital Seismic Network (BDSN) is our regional seismic network of about 40 sites where both broadband and strong motion seismic instrumentation is installed. This network is the backbone of the BSL's operations, feeding the necessary data for real-time estimation of location, size and rupture parameters for earthquakes in central and northern California. This network has been steadily growing since the 1990's and consists of very high quality, low noise sites, making the data ideal for a range of research efforts. The array can be used to study local or global earthquake sources, and provides data for investigation of 3D crustal structure in California and its effects on regional waveform propagation, which in turn affect the intensity of ground shaking in larger earthquakes. Recent additions to the network include an ocean bottom seismometer in the Monterey Bay (MOBB) providing real-time data via an undersea cable (operated in collaboration with MBARI), and also the Tremorscope stations along the Cholame section of the San Andreas Fault just south of Parkfield.

The real-time data is also Berkeley's contribution to the California Integrated Seismic Network (CISN), which is a federation of networks that jointly provide all real-time earthquake information in the state. Since 1996, the BSL and the USGS in Menlo Park have closely cooperated to provide the joint earthquake notification program for Northern California. This program capitalizes on the complementary capabilities of the networks operated by each institution to provide rapid and reliable information on the location, size and other relevant source parameters of regional earthquakes. The real-time earthquake information is made available through the BSL's website (<http://earthquakes.berkeley.edu>).

The BSL's borehole networks represent the second grouping of instrumentation. The High Resolution Seismic Network (HRSN) was installed in 1987 and now consists of 12 operating sites. Additional borehole sites will soon be added as part of the Tremorscope project. These instruments have led to wide-ranging research into earthquake processes due to their high sensitivity, low noise, and proximity to micro-earthquakes, clusters and tremor sources along the highly studied Parkfield section of the San Andreas Fault. In the Bay Area, the Hayward Fault Network also includes 15 borehole instruments that have been installed progressively since the 1990s. Again, the

goal of this network is to collect high signal-to-noise data for micro-earthquakes along the Hayward Fault to gain insight into the physics that govern fault rupture and its nucleation.

The third instrumentation type is GPS. The BSL operates the Bay Area Regional Deformational (BARD) Network consisting of 32 primary sites, 18 collocated with BDSN seismometers. All sites record with a 1 Hz sample rate and telemeter the data to BSL in real-time. Continuous GPS data tracks the motion of the tectonic plates and allows us to assess the strain buildup along faults as well as its release either through creeping episodes or through earthquakes. The application of GPS data feeds to real-time earthquake information is also a relatively new development. Very rapid processing now generates displacement waveforms that in turn support the development of improved real-time earthquake analysis methods for significant earthquakes.

The BSL's IT group is active in the development of new software for the collection, archival and real-time analysis of the various geophysical data streams that we collect. In 2009, the new AQMS seismic network software package was rolled out following a multi-year development effort by the BSL in collaboration with other CISN partners. This software provides all the real-time processing components needed by regional seismic networks and is now being rolled-out across the US. The development of real-time GPS processing software is a current area of focus for the lab along with development and implementation of earthquake early warning algorithms that can process the data quickly enough to provide alerts to people a few seconds to tens of seconds before shaking is felt.

Archival and distribution of data from the BSL and other regional geophysical networks is performed at the Northern California Earthquake Data Center (NCEDC), operated at the BSL in collaboration with USGS Menlo Park. The data reside on a mass-storage device (current holdings ~60 TB), and are accessible online (<http://www.ncedc.org>). In addition to BSL network data, data from the USGS Northern California Seismic Network (NCSN), and other Northern California networks, are archived and distributed through the NCEDC. The NCEDC also maintains, archives and distributes various earthquake catalogs.

Finally, the field engineering team is responsible for maintaining our existing ~70 geophysical observatories across Northern California, and designing and installing new sites. Of particular note is the completion in 2011 of the ARRA-funded upgrades. These urgently needed equipment upgrades replaced aging dataloggers at almost all BSL observatories, providing for more robust and more rapid transmission of data from the sites to the BSL real-time system. The group is now focused on the design and installation of the new Tremorscope borehole and surface stations just south of Parkfield along the

Cholame section of the San Andreas Fault.

All of these operations are supported by an operations and research staff of 10, an IT staff of 7, an engineering staff of 5, and an administrative support group shared with the Department of Earth and Planetary Science consisting of 7. In addition, there are currently 5 Postdoctoral Scholars and 14 PhD graduate students associated with the lab, along with 10 affiliated faculty.

Core University funding to our ORU provides salary support for one staff scientist (shared by three researchers), one IT staff member, one engineer, our operations manager, and two administrative assistants, and represents about one fifth of the total infrastructure support budget. The remaining support comes from extramural grants and contracts, primarily from the USGS, DOE, NSF, and the State of California, through its Emergency Management Agency (CalEMA). Currently, grants from the Gordon and Betty Moore Foundation contribute significantly to our operations as do the contributions from the members of our Earthquake Research Affiliates Program.

3 BSL Personnel News

Four new PhD graduate students joined the lab in the fall of 2011: Sierra Boyd, Cheng Cheng, Brent Delbridge, and Qingkai Kong. Also, Thomas Bodin, a new Miller Postdoctoral Fellow, and H. Serdar Kuyuk, a Postdoctoral Fellow, joined the lab. One PhD student, Aurelie Guilhem, graduated in December 2011. Her dissertation was titled “Analysis of unusual earthquake and tremor seismicity at the Mendocino Triple Junction and Parkfield, California.” Postdoctoral Fellow Colin Amos also departed from the lab.

As usual, a stream of visitors spent various lengths of time at the lab. Jamie Barron, Morgan Guinois, Matthias Meschede, and Sergei Ventosa all visited from Institut de Physique du Globe de Paris, France, at various times. Simona Colombelli from the University of Naples spent 8 months at the lab working on earthquake early warning, and Jiajun Chong from the University of Science and Technology of China spent a summer working on waveform inversion in the Tibetan region.

The BSL staff remained mostly stable during this year following the significant changes of the previous few years. Administrative support continues to be provided through a shared services model with the Department of Earth and Planetary Science under the leadership of manager Judith Coyote. The IT and research staff also remained mostly stable. Tom Weldon left the research staff and we are pleased to welcome Clay Miller who joined the BSL as a Staff Research Associate.

Finally, in June 2012, Bill Karavas left the BSL. Bill was the lead engineer for the BSL networks for almost 20 years. During that time Bill led the effort to build

the BDSN and much of the BARD network. He was also involved in supporting the borehole networks for the last few years. The quality of the BSL data, used by researchers around the world, would not be what it is without Bill’s careful oversight of all engineering operations for the last two decades and we are very grateful to Bill for his efforts during that time.

4 Acknowledgements

I would like to thank our technical and administrative staff, scientists and students for their efforts throughout the year and their contributions to this annual report. Individual contributions to activities and report preparation are mentioned in the corresponding sections, except for the appendix sections, which were prepared by Jennifer Taggart.

I also wish to especially thank the individuals who have regularly contributed to the smooth operation of the BSL facilities: Mario Aranha, Doug Dreger, Aaron Enright, John Friday, Peggy Hellweg, Ivan Henson, Ingrid Johanson, Bill Karavas, Clay Miller, Josh Miller, Pete Lombard, Bob Nadeau, Doug Neuhauser, Charley Paffenbarger, Jennifer Taggart, Taka’aki Taira, Stephen Thompson, Bob Uhrhammer, Tom Weldon, and Stephane Zuzlewski, and, in the administrative office, Marion Banks, Matt Carli, Judith Coyote, Dawn Geddes, and Gretchen vonDuering. I also wish to thank our undergraduate assistants, Cora Bernard, Jennifer Taing and David Tang, for their contributions to our research and operations activities.

I am particularly grateful to Jennifer Taggart and Peggy Hellweg for their help in putting together this annual report and bringing it to completion.

The Annual Report of the Berkeley Seismological Laboratory is available on the web at http://earthquakes.berkeley.edu/annual_report.

Chapter 2

Research Studies

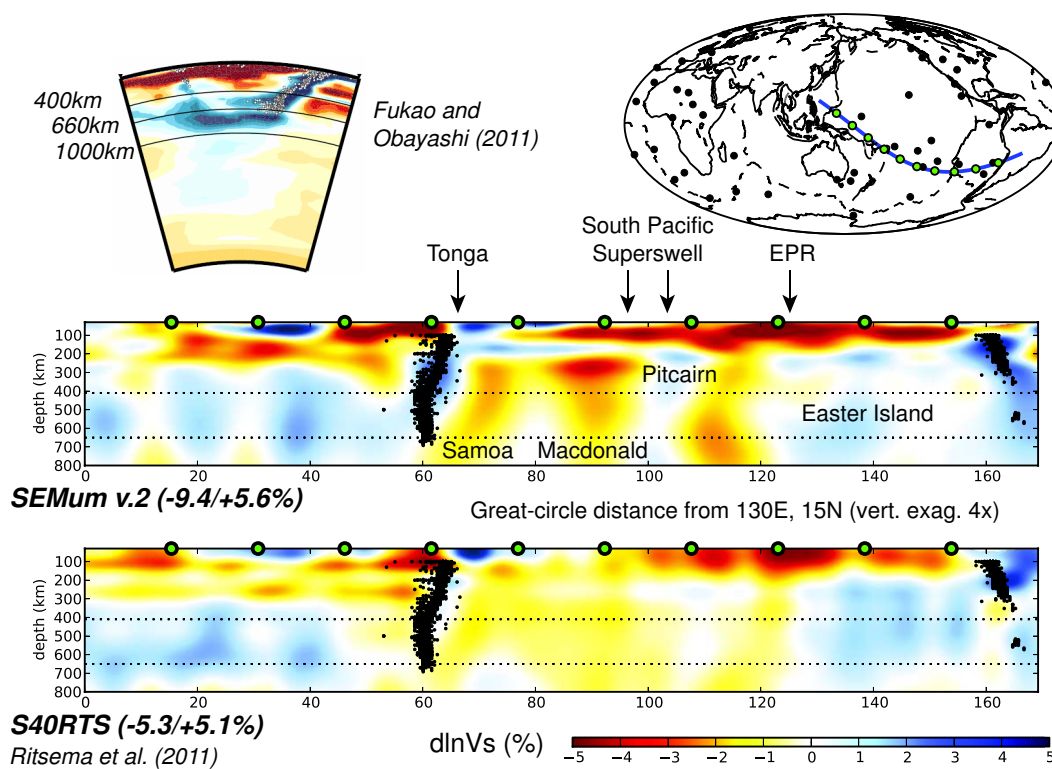


Figure 2.1: Upper mantle Earth structure beneath the South Pacific, imaged using seismic waves. Deep seismicity highlights subducted slabs, the remains of tectonic plates. The authors' second-generation, global upper-mantle model has been refined to improve interpretation of shallow upper-mantle structure under the oceans. From Research Section 26.

1 Episodic Tremors Highlight Slow Slip Events in Central California

Aurélie Guilhem and Robert M. Nadeau

1.1 Introduction

We present evidence that recurring episodes of non-volcanic tremors (NVT) along the San Andreas fault (SAF) near Parkfield, California are reminiscent of seismic events associated with episodic tremor and slip (ETS) and slow slip events (SSE) observed in subduction zones. They show systematic differences between aperiodic and periodic recurrences that are related to the 2004 M6.0 Parkfield (PKD) earthquake and the long-term SAF slip rate. After constraining their locations, duration, and response compared to repeating earthquake activity along the SAF, we propose a simple SSE model for the 52 PKD episodes observed in almost 10 years. We suggest that ~ 10 -day period SSEs correspond to slips of ~ 7.8 mm, occurring on a SAF parallel patch that is ~ 25 km long and between 15 km and 30 km depth.

1.2 Recurrence and size of the episodes

Figure 2.2 shows the updated catalog of NVT detections occurring along the SAF near PKD between 27 July 2001 and 21 March 2011. 2791 tremor bursts are reported, corresponding to continuously elevated signals of 3 to 21 minutes. During this time period, we automatically identified 52 episodes of tremors (Figure 2.2) lasting on average 10 days. The episodes' recurrence times, which range between 30 and 130 days, vary during the nearly 10 years of detection with periodic and aperiodic patterns (Figure 2.2). Before the 2004 PKD earthquake the episode recurrence is irregular. Between the 2004 PKD earthquake and 2009, recurrence intervals progressively lengthen at a rate of ~ 17.5 days/year (Figure 2.2). Since 2009, however, the irregularity in recurrence has returned.

The episode sizes also change after the PKD earthquake. We find that before the fore-tremor, there was in average about 68 minutes of tremors per episode. Episode size increased to about 120 minutes between the PKD mainshock and 2009. But, similarly to what is observed with the recurrence times, after 2009 the episodes sizes returned to levels more comparable to those seen before the fore-tremor, with an average of about 86 minutes of tremors per episode.

1.3 Location of the episodes

NVTs near PKD concentrate in two regions along the SAF: Monarch Peak and Cholame. By comparing their spatio-temporal activity in the two regions we find that the NVTs that compose the episodes are located near

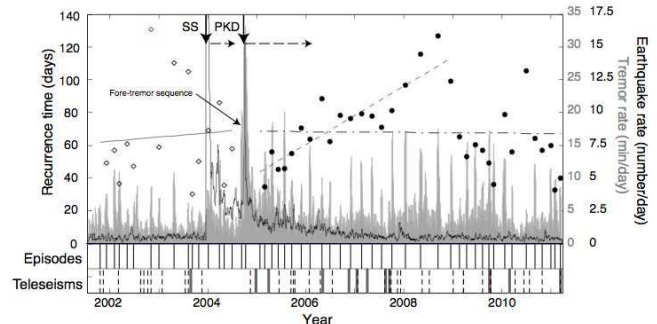


Figure 2.2: Tremor activity (gray) between 2001 and 2011 and recurrence times of episodes before (diamond) and after (dot) the 2004 Parkfield (PKD) earthquake. The overlying line shows the M1.4+ earthquake activity within 100 km of Parkfield. Times of the episodes are indicated by the vertical, continuous lines. Bottom: times of M7.5+ earthquakes.

Cholame, between 15 and 30 km depth, and on the western side of the SAF (Figure 2.3), along an ~ 25 km segment.

We also use the locations of 88 low-frequency earthquake (LFE) families reported by *Shelly and Hardebeck* (2010) to help provide additional constraints on the location of the NVT episodes. Because of the strong association between NVT and LFE activities, we make the assumption that the LFEs that are consistent in activity with NVT episodes occur within the source region of the NVT episodes. To identify them, we compare the timing of the NVT and LFE episodes between 2005 and 2010, using a measure of correlated episodicity, beta, for each of the 88 LFE families. Figure 2.3 shows that the LFE families that mimic the NVT episodes are also located along the same 25-km segment of the SAF (high beta values).

1.4 Source characteristics of the SSEs

It is possible to try to estimate the size of these SSEs. We compare the cumulative duration of the tremor activity to the cumulative slips inferred from groups of repeating earthquakes observed along the SAF in the creeping section, in the PKD coseismic zone, and in an intermediate region NW of the PKD rupture. We find that this last group better mimics the tremor activity both before and after the PKD earthquake. From their corresponding cumulative slip, we infer that the SSEs would correspond

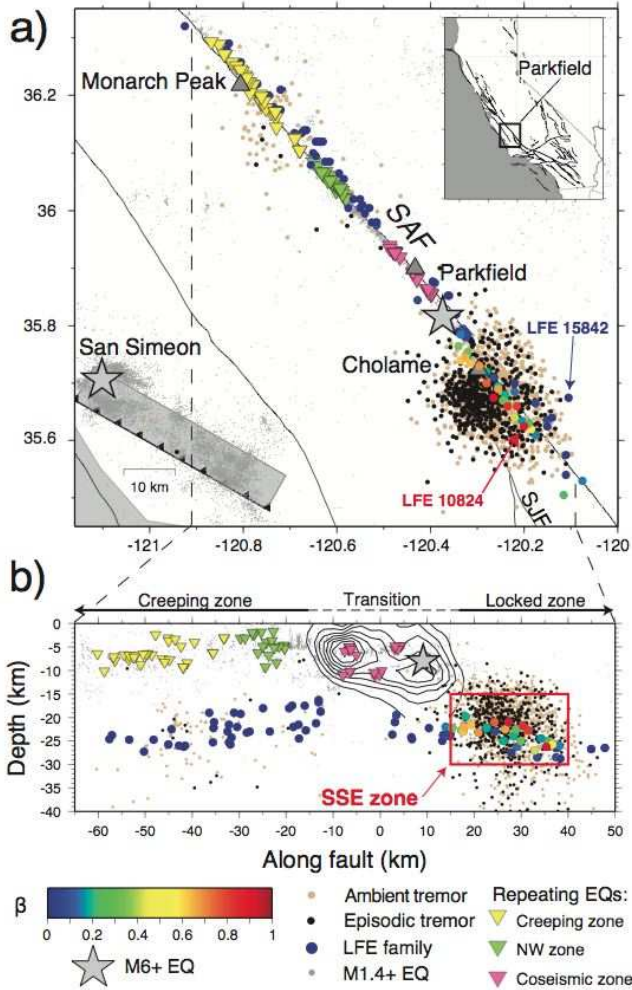


Figure 2.3: Location of well-located NVT activity (black dots: episodic, brown: non-episodic), LFEs (colored dots), and REQs (inverted triangles) in central California. The LFE families (circles) are color-coded by their beta coefficient (warm color: similar behavior, cold color: different). a) Map view. b) Cross-section view.

to slips of ~ 8 mm during 10 day periods. Combined with the estimates of the size of their source region, they correspond to $M_w 5.2$ events on average.

We also use an empirical linear relationship from Aguiar *et al.* (2009) that links the moment release of geodetically observed Cascadia SSEs to the cumulative duration of tremors during ETS events. From ~ 89.5 hours of SAF NVT activity recorded between 2001 and 2011, this gives a cumulative moment magnitude of 6.4. And each individual 10-day NVT/SSE episode ranges between $M_w 5.0$ and 5.4, with an average at $M_w 5.2$. Assuming correct area and displacement estimates, our results also suggest very little bias between the NVT duration determinations of Aguiar *et al.* (2009) and this study.

Furthermore, it is possible to explore parameters linked to strain release and stress drop that are important for inversion of the SSE deformation. We find that the strain release is on the order of $4e-7$, over 24 times smaller than those that have been used in previous unsuccessful searches for geodetic signals associated with tremors in the region (Smidth and Gomberg, 2009). Finally, this implies an average stress drop of ~ 12 kPa for the SAF SSEs. This is 2 to 3 orders of magnitude smaller than for regular earthquakes, but this is consistent with NVT observations in the region and in other tremor regions.

1.5 Discussion

Our results open perspectives for further study of SSEs, and changes in the behavior of the SAF episodic tremors can give information on variations in the state of stress in the deep fault zone. This study emphasizes the importance of studying the SAF NVTs with the goal of estimating the fault stress regime and its changes through time. SAF NVTs provide information on small changes in the properties of the fault that other geophysical techniques have yet to successfully illuminate.

1.6 Acknowledgements

Supported by the U.S. Geological Survey through award G10AC00093 and by the National Science Foundation through awards EAR0738342 and EAR0910322.

1.7 References

- Aguiar, A.C., T.I. Melbourne, Scrivner, C.W., Moment release rate of Cascadia tremor constrained by GPS, *J. Geophys. Res.*, 114, B00A05, 2009.
- Shelly, D. R., Hardebeck, J. L., Precise tremor source locations and amplitude variations along the lower-crustal central San Andreas fault, *Geophys. Res. Lett.*, doi:10.1029/2010GL043672, 2010.
- Smith, E.F., Gomberg, J., A search in strainmeter data for slow slip associated with triggered and ambient tremor near Parkfield, California, *J. Geophys. Res.*, 114, B00A14, 2009.

2 Searching for Small Deformation Signals in Laser Strainmeter Data Associated with Seismic Tremor in Parkfield

Brent Delbridge and Roland Bürgmann

2.1 Introduction

It has been hypothesized that shear dislocation on the plate interface accompanies deep tremor and low frequency earthquakes (LFE's) (e.g. *Wech and Creager, 2007; Ide et al, 2007; Shelly, 2007*). We hope to test this claim on tremor and LFE's on the San Andreas fault (SAF) through rigorous statistical examination of the laser strainmeter data from two long baseline instruments near Chalome, CA . It has also been shown that slow slip accompanies tremor in several subduction zones, however, there has not been an observation of deformation associated with the observed tremor in a transform fault setting such as the SAF, despite the ubiquitous presence of tremor and low frequency earthquakes (*Shelly et al, 2007; Nadeau et al, 2005*). It is believed that the strain rate is too small to be detectable by GPS, and previous studies attempting to use borehole strainmeters in Park-

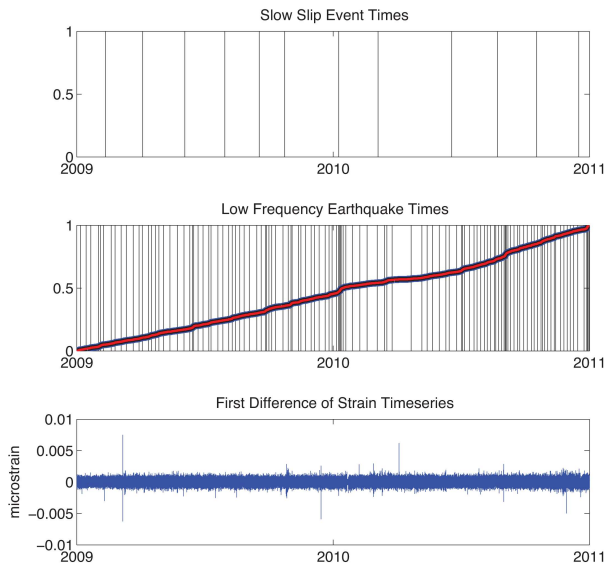


Figure 2.4: The top panel plots vertical lines to represent the times of peak correlation within large tremor bursts, which have been interpreted as slow slip events by Guilhem and Nadeau. The second panel shows the times of every thousandth LFE event as a vertical line, while the continuous curve represents a normalized cumulative count of all LFE events in the selected time period. In the bottom panel we show the first difference of processed data where non-tectonic signals have been removed using the barometric pressure, tides, and optical anchors.

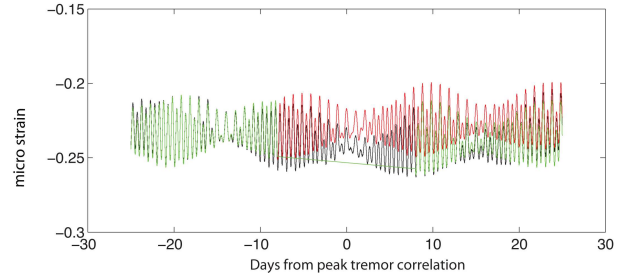


Figure 2.5: The black curve is the raw strainmeter data, the green curve is the fit to the data excluding the window about the peak correlation time, and the red curve is the model that is removed from the data.

field have failed to detect any observable strain associated with tremor swarms triggered by passing surface waves (*Smith et al, 2009*). This study hopes to go beyond that work and take advantage of the large number of LFE observations to lower drastically the signal to noise ratio. Additionally, we hope to observe strain associated with newly identified large tremor swarms that are inferred to as slow slip events (SSE's) with moment magnitudes exceeding 5 (*Guilhem et al, in press*). These slow slip events have durations of ~ 5 -10 days, far too long to be observed with traditional seismometers, and the deformation is far below the detection level of GPS. However we believe that Laser strainmeter (LSM) is particularly well suited to observe these signals, due to the relatively low detection level at periods of 10^5 to 10^6 seconds (*Agnew, 2003*).

2.2 Data

We have three different types of datasets to utilize in this analysis: high rate time series, a dense point process series, and a sparse quasi-periodic point process. These correspond to the laser strainmeter records, locations and times of low frequency earthquakes, and recently identified clusters of tremor which are believed denote otherwise aseismic slow slip events respectively. We do not believe these data to be independent. Below we show the times of the inferred SSE events, a normalized cumulative count of LFE events, and the first difference of a sample strainmeter record. The strain timeseries is not raw data, but derived data. We have taken the calibrated signal and removed known physical signals such as tides, barometric effects, corrections due to the vac-

uum pressure, and local corrections calculated from the instrument’s optical anchors. This derived data is what we will view as a signal plus noise and a seasonal component.

Methodology

In order to observe the small offsets and temporal correlation of LFE deformation in the straindata we employ an empirical correction to the data. The corrections we use are intended to facilitate stacking of the data. We first select 25 days on either side of each time shown in the top panel of 2.4. Since we suppose that there is deformation happening around this time, we do not use the 5 days surrounding the selection times. From the remaining 40 days we perform a least squares inversion to fit the diurnal and semidiurnal tides, simultaneously with a linear trend and step function. The step function here is not used to estimate an offset but rather to prevent any bias in the linear fitting. The coefficients for the tidal amplitudes and linear fit are then used to create a model of the tides and drift over the entire 50 day window and are removed from the data. An example this procedure is show in Figure 2.5.

2.3 Problem Formulation

Let the strain timeseries be denoted by $Y(t)$, the slow slip point process times by τ_i^{SSE} , and the low frequency earthquake times by τ_j^{LFE} . We will denote the response in the strain timeseries due to a tectonic point processes as $F(\tau_i^{SSE})$ and $G(\tau_j^{LFE})$ respectively.

$$Y(t) = \sum_i F(\tau_i^{SSE}) + \sum_j G(\tau_j^{LFE}) + trend + seasonal + noise \quad (2.1)$$

Though since the signal associated with the LFE process is *a priori* believed to be below our level of detection, we most likely believe the data to be

$$Y(t) = \sum_i D^{SSE}(\tau_i^{SSE}) + trend + seasonal + noise. \quad (2.2)$$

The goal of this study is to find the deformation associated with each point process. Or in other words, is the signal we derive from the strainmeter after accounting for the seasonal signal and trend correlated with either of our candidate point processes.

2.4 References

Agnew D, Wyatt F, Long-Base Laser Strainmeters: A Review, *Scripps Institution of Oceanography Technical Report*, 2003

Guilhem A, and Robert N, Episodic tremors and deep slow-slip events in Central California, *Earth and Planetary Science Letters*, under review.

Ide S, Shelly D, Beroza G, Mechanism of deep low frequency earthquakes: Further evidence that deep non-volcanic tremor is generated by shear slip on the plate interface, *Geophys. J. Int.*, 34, 3, 2007.

Nadeau R, Dolenc D, Nonvolcanic tremors deep beneath the San Andreas fault, *Science*, 307, 5708, 2005.

Shelly D, Beroza G, Ide S, Non-volcanic tremor and low-frequency earthquake swarms, *Nature*, 446, 7140, 2007.

Wech AG, Creager KC, Cascadia tremor polarization evidence for plate interface slip, *Geophys. Res. Lett.*, 31, 22, 2007.

3 TremorScope: Imaging the Deep Workings of the San Andreas Fault

Roland Bürgmann, Richard Allen, Pascal Audet, Douglas Dreger, Robert Nadeau, Barbara Romanowicz, Taka'aki Taira, Margaret Hellweg

3.1 Introduction

Until recently, active fault zones were thought to deform via seismic earthquake slip in the upper, brittle section of the crust, and by steady, aseismic shear below. However, in the last few years, this view has been shaken by seismological observations of seismic tremor deep in the roots of active fault zones. First recognized on subduction zones in Japan and the Pacific Northwest, tremor has also been found to be very active on a short section of the San Andreas to the southeast of one of the most densely monitored fault segments in the world, near Parkfield (*Nadeau and Dolenc, 2005*). This deep ($\sim 20\text{-}30$ km) zone of activity is located right below the nucleation zone of the great 1857 Fort Tejon earthquake. Thus, understanding the temporally and spatially complex faulting process in this zone may help us better understand the conditions that lead to such large ruptures.

3.2 The Project Plan

The tremor source region is south-east of existing seismic networks around Parkfield, along the San Andreas Fault. We are adding eight seismic stations, the TremorScope (TS) network, in this area to complement existing instrumentation.



Figure 2.6: Installation of seismic vault at TremorScope station THIS.

Six of eight planned sites for the TS network have been permitted and the first two two surface stations installed. Figure 2.6 shows installation of the seismometer vault at station THIS. Surface installations have a broadband seismometer, an accelerometer and a digitizer. The borehole sites, with a hole about 300 m deep will have an accelerometer at the surface. Downhole will be a cemented, three-component set of gimbaled, 2 Hz geophones. Three boreholes will be equipped with a Guralp downhole sensor package, consisting of a three-component broadband seismometer, a three-component accelerometer and a digitizer. At all locations, data will be logged onsite and forwarded to Berkeley for real-time processing. The data will be used in real-time earthquake monitoring (see Operational Section 8), as well as for tremor studies. The first data are in. Figure 2.7 shows triggered tremor from the M8.6 earthquake of April 11, 2012, in the recording of station TSCN. This tremor was also apparent at HRSN stations.

3.3 Perspectives

Data from the TremorScope project will improve earthquake monitoring in the region south of Parkfield. Insights from the project will also contribute to understanding tremor and slip in other regions of the world where such phenomena have been observed, but are not nearly as accessible. Should a great San Andreas earthquake occur during this experiment, the network would also provide unprecedented and exciting insights into the seismic rupture process.

3.4 Acknowledgements

This work is funded by grant 2754 from the Gordon and Betty Moore Foundation.

3.5 References

Nadeau, R., and D. Dolenc (2005), Nonvolcanic tremors deep beneath the San Andreas fault, *Science*, 307, 389, doi:10.1126/science.1107142.

Mw8.6 Off the West Coast of Northern Sumatra 2012 April 11

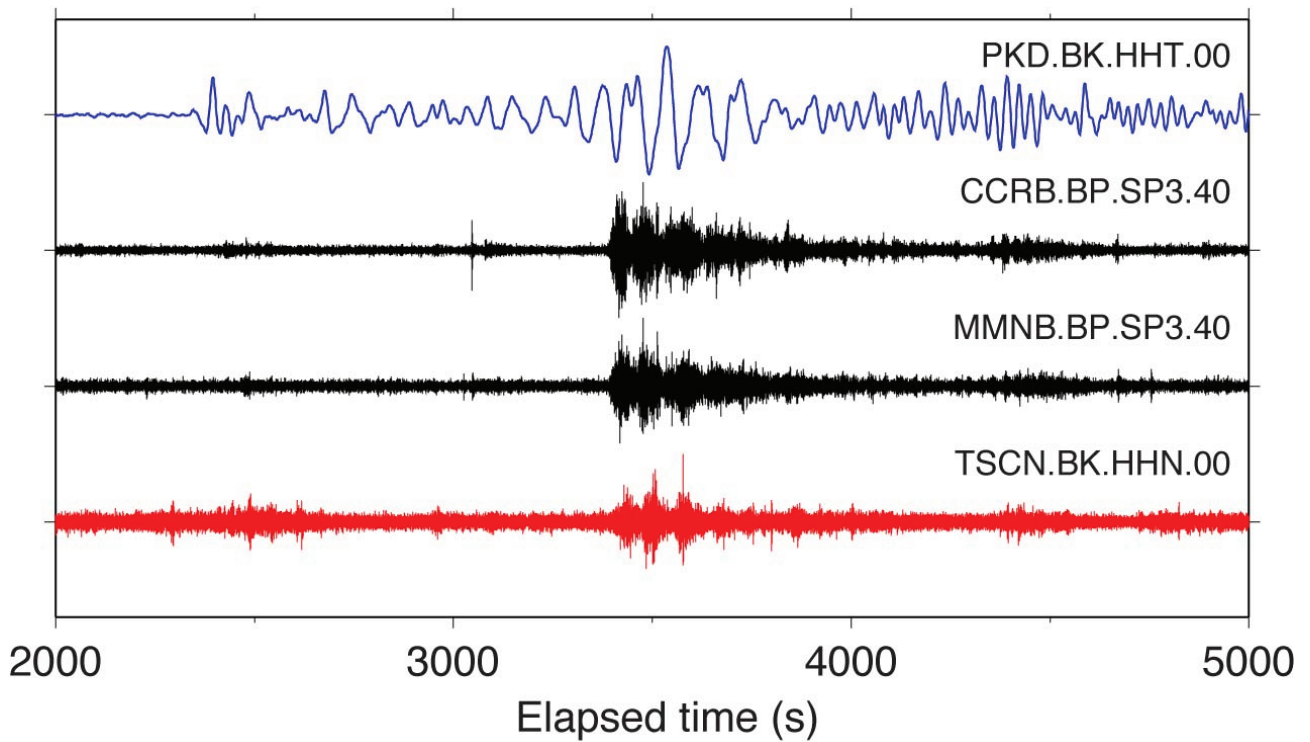


Figure 2.7: Triggered tremor in the surface waves of the April 11, 2012, M8.6 earthquake which occurred off the West Coast of Northern Sumatra. Tremor is apparent in the records of HRSN stations CCRB and MMNB as well as at TremorScope station TSCN.

4 Time-dependent Model of Creep on the Hayward Fault from Joint Inversion of 18 Years of InSAR and Surface Creep Data

Manoochehr Shirzaei, Roland Bürgmann

4.1 Introduction

Spatial and temporal variations of aseismic fault creep represent important factors in realistic estimation of seismic hazard due to their influence on the size and recurrence interval of large earthquakes along partially coupled faults. To solve for a time-dependent model of creep on the Hayward fault, we invert 18 years of surface deformation data (1992 - 2010), obtained by interferometric processing of 52 and 50 synthetic aperture radar (SAR) images acquired by the ERS1/2 and ENVISAT satellites, respectively, and surface creep data obtained at more than 25 alignment and creepmeter stations. To jointly invert the residual InSAR displacement time series and the surface creep data and to obtain a time-dependent model of creep on the Hayward fault, we use an iterative re-weighted L2-norm minimization approach combined with a linear Kalman filter. The time-dependent model constrains a zone of high slip deficit (low creep rate) that may represent the locked rupture asperity of past and future $M \approx 7$ earthquakes.

4.2 Approach

In this research, we include 18 years of InSAR data collected by the ERS-1, ERS-2 and Envisat satellites. A total of 831 interferograms are processed from 102 images collected between 1992 and 2011. These are processed into a time series of surface range change and used as input in the time-variable modeling. The time history of the creep on Hayward fault is obtained by time-dependent joint inversion of the InSAR time series and surface creep data. To this aim, we employ a method consisting two main operators: (i) a L1-norm minimization operator and (ii) a recursive filter, Kalman Filter (KF), to generate time series of the creep. These two operators are combined in an iterative manner (*Shirzaei and Walter, 2010*). The InSAR data are complemented by observation of surface creep obtained from alignment array measurements (*Lienkaemper, et al., 1991; Lienkaemper and Galehouse, 1997*) and creepmeter data (*Bilham and Whitehead, 1997*) along the Hayward fault.

4.3 Observations and Results

Figure 2.8a shows a map of the LOS velocities of the obtained InSAR time series. Major components of the resolved signal include displacement due to plate motions and elastic strain accumulation across the San Andreas fault system, and non-tectonic land subsidence and re-

bound. Here, we focus on the discontinuity along the Hayward fault that is an indicator for shallow fault creep and comprises shorter wavelength features compared to the long term interseismic deformation components (e.g., [*Schmidt, et al., 2005*]). The time-dependent creep rate model of the Hayward fault for 1992-2010 is shown in Figure 2.8b. The darker colors indicate more right-lateral creep. In Figure 2.8b, the location of the creepmeters and alignment arrays and their associated observations of actual surface creep are shown for comparison with the creep model. There is very good agreement between the model and surface creep observations. Our results show that the upper 3-4 km of the Hayward fault from 45 to 70 km distance, creeps faster than the northern section (km 0 - 30). In the north, the faster creep occurs at a depth of 5 - 10 km. A large locked patch that creeps at < 1 mm/yr is constrained at 25 - 45 km, in agreement with earlier works (*Simpson, et al., 2001; Malservisi, et al., 2003; Funning, et al., 2005; Schmidt, et al., 2005*) but not with the model result of *Evans, et al. (2012)*.

4.4 Conclusion

We present a spatiotemporal model of creep on the Hayward fault. To this end we explored an 18-year-long time series of InSAR deformation and surface creep data. Our time-dependent creep model reveals a persistent accumulation of slip deficit (more than 90% of the geologic slip rate) along a buried ~ 25 -km-long and ~ 7 -km-wide section of the fault. These results suggest that the creep rate is faster at shallow depths along the southern Hayward fault compared to the northern fault section, which has higher rates at depth. This variation may reflect changes in the regional stress field and/or material heterogeneities along the Hayward fault. Given the fact that most of the Hayward fault accumulates a slip deficit of 30%-90% of its long-term slip budget, we estimate a seismic moment accumulation of $M_w \sim 6.3$ -6.8, respectively, due to rupturing only the large central locked zone or rupture propagation to the entire 70 km of the Hayward fault including the area of low deficit, since the last big event in 1868.

4.5 References

Bilham, R., and S. Whitehead (1997), Subsurface creep on the Hayward fault, Fremont, California, *Geophys. Res. Lett.*, 24, 11, 1307-1310.
Evans, E. L., J. P. Loveless, and B. J. Meade (2012), Geodetic constraints on San Francisco Bay Area fault slip rates and

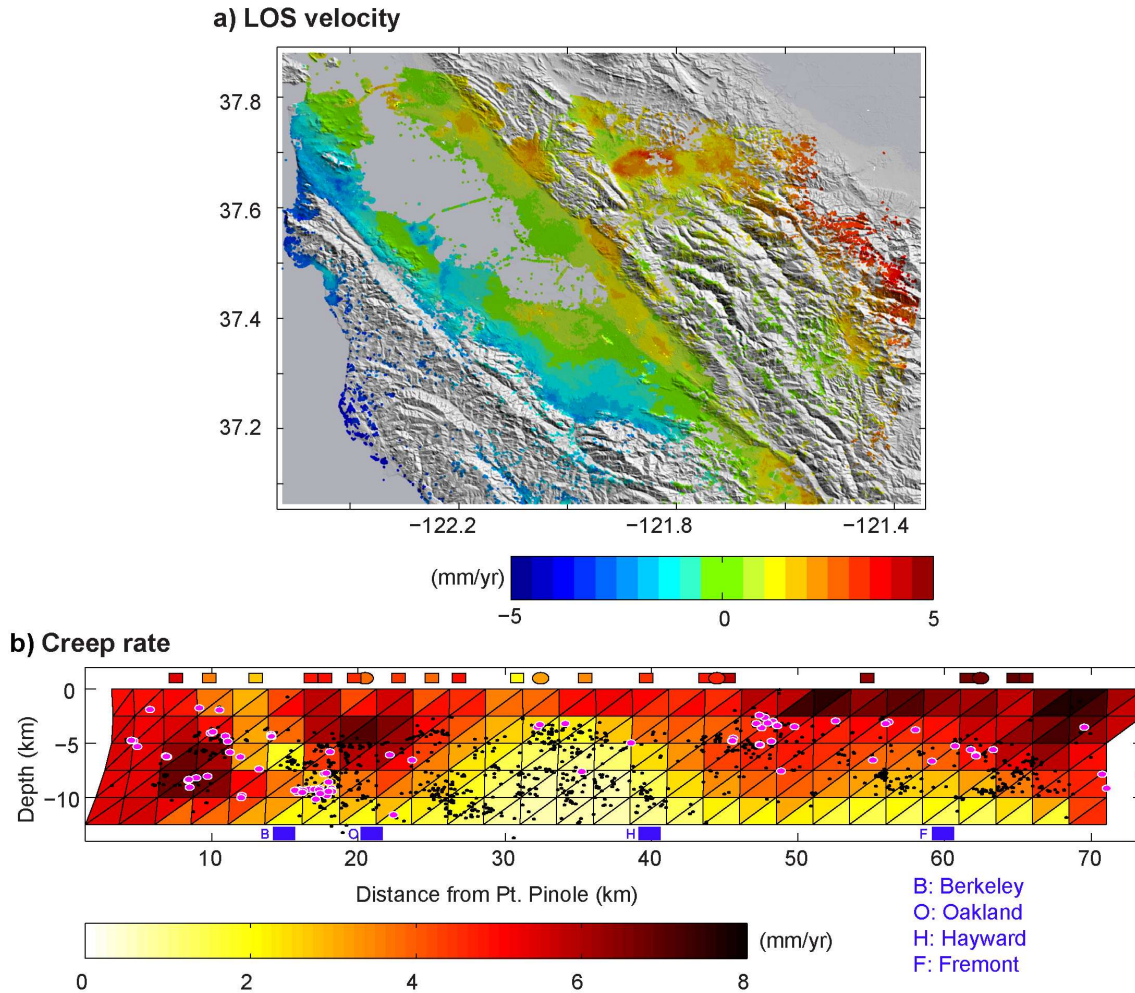


Figure 2.8: a) The LOS velocity from 1992-2010 InSAR time series. Red and blue colors indicate movement toward and away from the satellite, respectively. The satellite incidence angle and heading angles are 23° and 188° . b) Average right-lateral creep rate along the Hayward fault. In addition to microseismicity shown by black dots, the magenta circles show the location of repeating events. Average 1992-2010 rates from surface measurements are shown by symbols on top with same color scale. (See color figure on cover.)

potential seismogenic asperities on the partially creeping Hayward fault, *Journal of Geophysical Research-Solid Earth*, 117.

Funning, G., R. Bürgmann, A. Ferretti, F. Novali, and D. A. Schmidt (2005), Kinematics, asperities and seismic potential of the Hayward fault, California from ERS and RADARSAT PS-InSAR, *EOS, Transactions American Geophysical Union*, 86, 52.

Lienkaemper, J. J., G. Borchardt, and M. Lisowski (1991), Historic creep rate and potential for seismic slip along the Hayward fault, California, *J. Geophys. Res.*, 96, 18261-18283.

Lienkaemper, J. J., and J. S. Galehouse (1997), Revised long-term creep rates on the Hayward fault, Alameda and Contra Costa counties, California, Open-File Rept. 97-690, 618 pp, U.S. Geol. Surv.

Malservisi, R., C. Gans, and K. P. Furlong (2003), Numerical modeling of strike-slip creeping faults and implications for the Hayward fault, California, *Tectonophysics*, 361, 1-2, 121-137.

Schmidt, D. A., R. Bürgmann, R. M. Nadeau, and M. d'Alessio (2005), Distribution of aseismic slip rate on the Hay-

ward fault inferred from seismic and geodetic data, *J. Geophys. Res.*, 110, B8.

Shirzaei, M., and T. R. Walter (2010), Time-dependent volcano source monitoring using interferometric synthetic aperture radar time series: A combined genetic algorithm and Kalman filter approach, *J. Geophys. Res.*, 115, B10421, doi:10.1029/2010JB007476.

Simpson, R. W., J. J. Lienkaemper, and J. S. Galehouse (2001), Variations in creep rate along the Hayward fault, California, interpreted as changes in depth of creep, *Geophysical Research Letters*, 28, 11, 2269-2272.

5 Landslide Risk Assessment (LSRA): GPS Instrumentation and Remote Sensing Study of Slope Movement in the Berkeley Hills, California.

Julien Cohen-Waeber (Civil and Environmental Engineering), Roland Bürgmann, Nicholas Sitar (Civil and Environmental Engineering)

5.1 Introduction

The objective of this study is to characterize slope deformation as a result of static and dynamic forces, using the most current geodetic technologies that measure active ground surface displacement. New and improved methods for geodetic and remote data collection, such as continuous GPS, and Interferometric Synthetic Aperture Radar (InSAR) allow for a level of primary site characterization and eventual landslide risk assessment that was previously not possible. These technologies need to be incorporated into current practice and tested. Active landsliding across the Lawrence Berkeley National Laboratory (LBNL) site and the greater Berkeley Hills region, California, has been the object of many investigations over recent decades, though the mechanisms of currently mobile, slow moving slides are still poorly understood. Previous studies suggest that a trend in landslide mobility is associated with regional climate and active tectonic conditions in addition to the local geologic setting. A first focus of this project is therefore to study the spatial and temporal distribution of active Berkeley Hills landsliding in relation to local precipitation and ground shaking events by a careful observational program. This program includes the instrumentation of individual landslides with permanent continuously streaming GPS stations, and regional monitoring of slope surface deformation by InSAR time series analysis. Subsequently, the mechanisms of some of these slow moving landslides will be modeled, integrating our surface observations with previous subsurface investigations and monitoring.

5.2 Setting

As part of the northwest trending California Coast Range geomorphic province, the Berkeley Hills are an uplifted block of Jurassic to Tertiary sedimentary, volcanic and metamorphic rock formed during regional transpression related to the active plate margin 1-2 million years ago. Now largely overlain by Quaternary colluvial and alluvial deposits, this generally highly fractured, intensely weathered, moderately soft rock is prone to landsliding. In addition to the geologic setting, studies suggest a trend in Berkeley Hills landslide mobility associated with regional climate and active tectonic conditions (*Alan Kropp and Associates, 2002; Hilley et al., 2004; Quigley et al., 2010*). Today, over 500 landslide-related geologic and geotechnical investigation reports are available for LBNL

and the Berkeley Hills alone, and form a solid background to this project.

5.3 Methodology

Two state of the art geodetic sensing technologies form the primary modes of data acquisition in this project: high rate, continuously streaming, Global Positioning Systems (GPS) and space-borne Interferometric Synthetic Aperture Radar (InSAR). These methods are complementary in that GPS provides discrete ground surface displacement measurements with millimeter scale accuracy and precision, while InSAR time series analysis produces spatial averages at decameter resolution with sub-centimeter precision. Combining these methods allows for spatial and temporal distribution analysis of ground surface displacements due to landsliding in relation to local precipitation and ground shaking events. By incorporating these surface observations with previous investigations and monitoring, the landslide mechanisms can then be modeled.

5.4 Project Status

The first phase of this project has been to instrument individual landslides with autonomous, continuously streaming GPS stations, collecting readings at 1Hz for average daily solutions and a 5Hz buffer in the case of seismic activity. Each device has been specifically designed for permanent installation as a stand-alone station and made to capture actual landslide displacement at depth. Anchored on deep-seated reinforced concrete foundations to avoid the effects of surficial disturbance, the stations are solar powered and equipped with a wireless antenna for remote access. Since January 2012, five such stations have been successfully installed at LBNL and one at the University of California Blake Garden on the Blakemont Landslide. Four additional sites in the Berkeley Hills are in the process of being developed. With the concurrent development of this GPS network, InSAR time series analysis has also begun. Satellite-based Radar images for InSAR time series analysis are available for the Berkeley Hills region dating back to 1992 and have already been the object of several studies as shown in *Hilley et al. (2004)* and *Quigley et al. (2010)*.

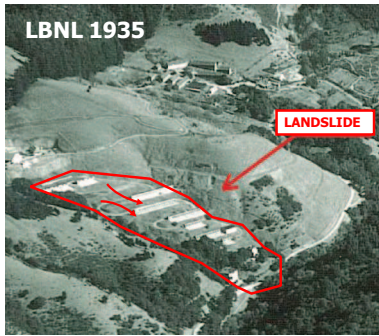


Figure 2.9: 1935 air photo depicting LBNL landslide.

5.5 Preliminary Results

Since January 2012, the first 6 continuously streaming GPS stations (LRA 1-6) have been producing daily solutions. Highlighted here are stations LRA 1-3 located on the same landslide at LBNL. While historical ground surface displacement related to this landslide has yet to be characterized and quantified, it is well defined as shown in the 1935 air photo in Figure 2.9 and has been the object of extensive subsurface investigations. Already, a clear signal at each of these 3 stations is apparent, showing down-slope displacements of up to 2cm and directly related to local precipitation. Time histories of daily solutions at stations LRA 1-3, from mid January through mid May 2012 are illustrated in Figure 2.10 and plotted against cumulative rainfall (solid line). Here, the daily solutions for each station's North and East baselines (circles and triangles respectively) are taken with respect to a fixed station (P224) several kilometers to the South and are shown to be moving down-slope to the west and southwest, accelerating during rainfall events.

5.6 Acknowledgements

We gratefully acknowledge our financial support from the Lawrence Berkeley National Laboratory, Earth Science Division Director's Fund.

5.7 References

Alan Kropp and Associates, Blakemont Area Geologic Study, Geologic Hazard Abatement District study, El Cerrito and Kensington CA., 2002.

Hilley, G.E., R. Bürgmann, A. Ferretti, F. Novali, and F. Rocca, Dynamics of Slow Moving Landslides From Permanent Scatterer Analysis, *Science*, 304, 1952-1955, 2004.

Quigley, K. C., R. Bürgmann, C. Giannico, and F. Novali, Seasonal Acceleration and Structure of Slow Moving Landslides in the Berkeley Hills, *Calif. Geol. Surv. Spec. Report 219, Proceedings of the Third Conference on Earthquake Hazards in the Eastern San Francisco Bay Area; edited by Keith Knudsen*, 169-178, 2010.

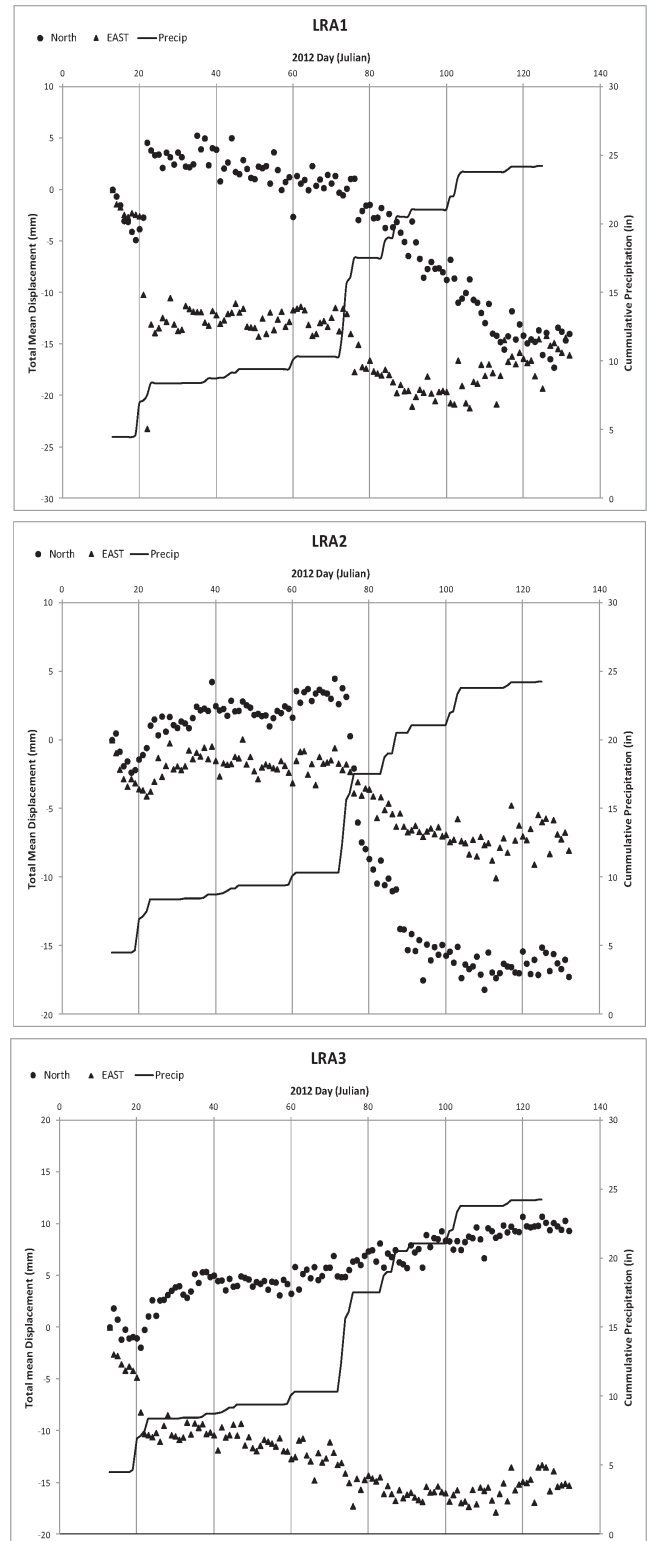


Figure 2.10: Displacement time histories of stations LRA 1-3 with respect to a reference GPS station (P224) to the south. Deviation from the North (circles) and East (triangles) baselines indicates down slope movement to the west and south-west, accelerating during periods of significant precipitation (line).

6 Investigating Fault Slip and Rheology Along the San Andreas Fault in the San Juan Bautista Region

Taka'aki Taira, Roland Bürgmann, Robert M. Nadeau, Douglas D. Dreger

6.1 Introduction

An improved understanding of the connection between seismic behavior and fault-zone rheology at depth is an essential step toward understanding the underlying mechanics of the faulting process. Spatially and temporally varying aftershock activities following large earthquakes are expected to be sensitive to stress-change magnitudes from the mainshock and spatial variations in rheological properties where aftershocks occur. A detailed analysis of aftershock sequences with the estimation of stress transfer from a mainshock therefore has the potential to illuminate the spatial variation in fault-zone rheology at seismogenic depth. We investigate the seismicity along the northernmost creeping section of the San Andreas fault near San Juan Bautista, California where an abundance of historical seismic and geodetic data is available.

6.2 Fault-Zone Rheology Inferred from Temporal Behavior of Aftershock Activity

We systematically examine spatiotemporal behaviors of the aftershock sequences following the 12 August 1998 M_w 5.1 San Juan Bautista (SJB) earthquake utilizing continuous seismic data. With the availability of over 20 years of historical seismic data (1984-2011), we make use of waveform data from about 13,000 SJB local earthquakes occurring within a 15 km radius of the epicenter of the 1998 SJB mainshock as template events to identify previously undetected aftershocks. This analysis resolves details of the aftershock activity in a zone at a depth of 9 km about 7 km northwest of the 1998 SJB mainshock (the blue rectangle shown in Figure 2.11). This aftershock zone is marked by one of the highest changes in seismicity rate. The aftershock zone experienced a cluster of earthquakes in the first month of the postseismic period. Except for this postseismic period, the background seismicity rate in this zone has been stable at low level (0.015/day). We infer that the aftershock activity revealed from our analysis was induced by the coseismic stress change from the 1998 SJB mainshock.

Our analysis indicates that the aftershock activity in this zone exhibits a delayed peak (~ 20 hours after the 1998 SJB mainshock) in the rate of aftershocks, preceded by a period of a very low rate of aftershocks just after the mainshock (Figure 2.12). Subsequently, the rate of aftershocks shows power-law decay with time for about one month, and then there was no clear aftershock activity in this zone. There is no larger aftershock that

could have initiated this sequence around the onset time of the observed delayed peak. This temporal behavior of aftershock activity is different from the predicted aftershock decay based on the model of *Dieterich* (1994). Instead, our observation is more consistent with the decay rate of aftershocks occurring in the transition zone between locked and stable slip, as simulated numerically by *Kaneko and Lapusta* (2008).

We find that the aftershock zone is located near the base of the seismogenic depth (9.2 km) inferred from the depth above which 95 percent of background seismicity occurs. We infer that the San Andreas fault at the SJB region below the seismogenic depth is loaded by deep-seated slip with a long-term slip rate of 2.3 cm/year. Thus, we expect a depth variation in frictional properties near the base of the seismogenic depth or the aftershock zone due to the transition zone from fault locking to fault creep, which would also support the idea that the spatial variation in frictional properties leads to the observed delayed peak and subsequent quiescence in the rate of aftershocks.

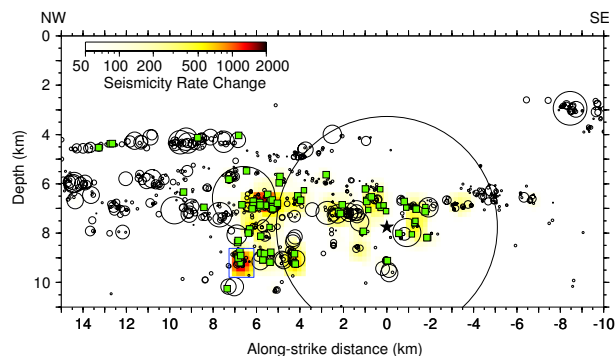


Figure 2.11: Cross-section view of seismicity rate change derived from the numbers of earthquakes occurring before (200 days) and after (30 days) the 1998 SJB mainshock. Black circles are microearthquakes occurring in the first 1000 days of the postseismic period of the 1998 SJB mainshock. Green squares are the identified short-lived (~ 1 month) repeating earthquake sequences or multiplets. Circle sizes are proportional to earthquake rupture sizes. The blue rectangle indicates the aftershock zone exhibiting a delayed peak in the rate of aftershocks (Figure 2.12). Also shown is the hypocenter of the 1998 M_w 5.1 SJB earthquake (star).

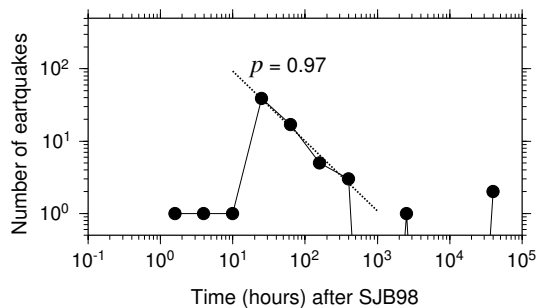


Figure 2.12: Number of earthquakes in the aftershock zone (the location is shown as the blue rectangle in Figure 2.11) following the 1998 SJB mainshock (SJB98). The peak in the rate of aftershocks is observed at about 20 hours after the mainshock. Subsequently, the rate of aftershocks decayed with the slope of $\sim 1.0/\text{time}$ in a 1-month period, followed by seismic quiescence.

6.3 Spatiotemporal Pattern of Characteristically Repeating Earthquakes

Our analysis with continuous seismic data identifies the number of characteristically repeating microearthquake sequences associated with the 1998 SJB mainshock (Figure 2.11). The majority of these sequences have earthquakes occurring within the first 1 month of the post-seismic period. In other words, they reflect short-lived, accelerated repeater recurrences activated by the 1998 SJB mainshock. This temporal pattern could indicate that these sequences are located at rheological boundaries between stable and unstable sliding in which the coseismic stresses were accumulated, rather than that they represent small asperities surrounded by creeping areas. The sequences are localized in the northwest of the 1998 SJB hypocenter. Our kinematic slip inversion of the 1998 SJB mainshock suggests northwest directivity of the rupture propagation (see below and Figure 2.13). We expect larger stress concentrations from the 1998 SJB mainshock in the region northwest of the hypocenter, compared with those in southeast region. Thus, the spatiotemporal pattern of short-lived repeating earthquake sequences will delineate the spatially- and temporally-varying stress transfer induced by the 1998 SJB mainshock.

6.4 Rupture Process of the 1998 M_w 5.1 San Juan Bautista Earthquake

Kaneko and Lapusta (2008) showed that a nonuniform coseismic stress change from a mainshock can play an important role in triggering aftershock activity following Omori's law for a certain period of time and then disappearing. A model of the stress transfer from the 1998 SJB mainshock is therefore essential. We estimate the slip distribution of the 1998 M_w 5.1 SJB earthquake using

a kinematic source inversion with an empirical Green's function (eGf) approach (Dreger, 1994). We use a M 3.1 foreshock occurring 8 minutes before the mainshock to extract the moment rate function (MRF) of the mainshock through the deconvolution process. The MRFs obtained from distributed broadband stations indicate northward directivity (Figure 2.13a). Our preliminary result shows the 1998 SJB mainshock has a concentrated slip patch with a radius on the order of 50-100 m, with peak slip of about 40 cm (Figure 2.13b). Our next step is to evaluate the spatial variation in Coulomb stress change based on our fault slip model and to explore the variability of fault frictional properties along the San Andreas fault in the SJB region.

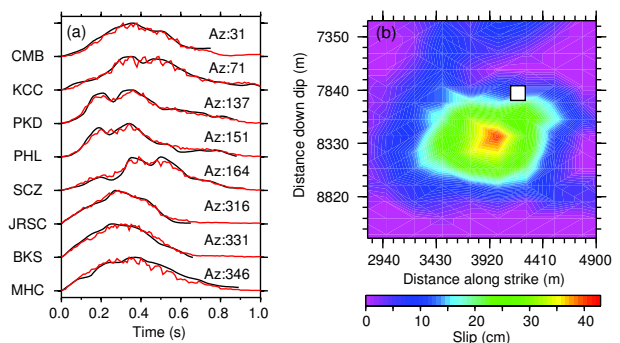


Figure 2.13: (a) Moment rate functions (MRFs) obtained by empirical Greens function deconvolution (black lines). The MRFs show that the pulse width narrows at stations JRSC and BKS (northwest from the 1998 SJB mainshock), indicating rupture directivity to the northwest. Also shown is the synthetic data (red lines) from the slip model shown in Figure 2.13b. (b) Slip distribution obtained for the 1998 M_w 5.1 SJB earthquake from the inversion of the eight MRFs shown in Figure 2.13a. The hypocenter is plotted as the white square.

6.5 Acknowledgements

We thank R. Turner, P. Audet, and I. Johanson for discussion, and the Northern California Earthquake Data Center (NCEDC) for data collection and distribution. This work is supported by the National Science Foundation EAR-0951430.

6.6 References

- Dieterich, J. H., A constitutive law for rate of earthquake production and its application to earthquake clustering, *J. Geophys. Res.*, *99*, 2601-2618, 1994.
- Dreger, D. S., Empirical Green's function study of the January 17, 1994 Northridge, California earthquake, *Geophys. Res. Lett.*, *21*, 2633-2636, doi:10.1029/94GL02661, 1994.
- Kaneko, Y., and N. Lapusta, Variability of earthquake nucleation in continuum models of rate-and-state faults and implications for aftershock rates, *J. Geophys. Res.*, *113*, B12312, doi:10.1029/2007JB005154, 2008.

7 Aseismic Slip and Fault Interaction from Repeating Earthquakes in the Loma Prieta Aftershock Zone

Ryan C. Turner, Robert M. Nadeau, and Roland Bürgmann

7.1 Introduction

Along creeping sections of the San Andreas and other faults, small asperities in the fault zone load and fail in characteristic repeating earthquake sequences. By calculating their slip based on moment magnitude, they can be used as sub-surface creepmeters. Here, we use these virtual creepmeters to examine and compare slip rates on both the northwestern end of the creeping section of the San Andreas fault (SAF) near San Juan Bautista and the creeping section of the nearby Sargent Fault (SF). While creep on the SAF increases dramatically in response to the 1989 Loma Prieta earthquake (LP), the SF shows very little response, consistent with static stress change models that put this section of the fault in a stress shadow. After about ten years, the SAF creep rate falls back closer to plate rates and begins creeping coherently in time with the SF, indicating a mutual driving force in the system.

7.2 Activities

The main study area was comprised of two rectangular swatches aligned along the strike of the SAF (Figure 2.14). The study areas overlap with and extend to the northwest the existing catalog of repeating earthquake sequences and, for the sake of capturing the local extent of the repeaters, extend beyond the creeping section of the central SAF. The areas were chosen to include neighboring sub-parallel faults in the search for repeating earthquake activity, particularly the Sargent Fault (SF) which is known to have documented aseismic dextral creep (*Prescott and Burford, 1976*). Repeating earthquake sequences were identified by the method of *Nadeau and McEvilly (2004)*. The repeater catalog was also extended to the southeast and now includes the entire central creeping region of the SAF.

7.3 Findings

Before the LP earthquake, the slip rates on the SAF and SF do not appear to have had much correlation (Figure 2.15c). After October 1989, the LP rupture clearly has a large influence on the SAF slip rate southeast of about 160 km in our strike-parallel coordinate system, inducing strong rate increases of both pre-existing repeaters and non-repeating aftershocks. The SAF slip rate peaked at 20 cm/year before gradually falling back closer to the interseismic rate of 1cm/yr (Figure 2.15). Meanwhile, the SF creep rate inferred from the repeaters does

not experience any such excursion but does begin gradually increasing, a trend it follows for the next nine years. About 10 years after LP, the SAF and SF begin slipping in a correlated manner, their slip rates rising and falling with similar timing and amplitude.

On the SF, LP aftershocks occur almost exclusively to the northwest of the repeaters, consistent with the creeping-to-locked transition zone being at the edge of a LP stress shadow at about 156 km in our strike-parallel coordinate system. This is contrasted with the aftershock activity on the SAF, which overlaps with the northwestern SAF repeaters. So, while there was an increase in seismicity on the northwestern SF as reported by *Reasenber and Simpson (1997)*, that increase did not extend into the creeping section of the SF as it did on the SAF.

The static stress changes associated with LP dramatically accelerated slip on the SAF, consistent with measurements of increased surface creep (*Behr et al., 1997*). That we do not see a dramatic increase in slip rate on the SF seems to agree with the static stress changes on the SF associated with LP (*Simpson and Reasenber, 1994*).

7.4 Acknowledgements

Background seismicity data taken from Felix Waldhauser's Double-difference Earthquake Catalog for Northern California (1984-2009) - (NCAeqDD.v200912.1). This work is supported through National Science Foundation grant EAR-0951430. Data provided by the Northern California Earthquake Data Center (NCEDC).

7.5 References

- Behr, J., R. Bilham, P. Bodin, K. Breckenridge, and A. G. Sylvester, Increased Surface Creep Rates in the San Andreas fault Southeast of the Loma Prieta Mainshock. *U.S.G.S. Professional Paper 1550-D*, pages D179-D192, 1997.
- Nadeau, R. M. and T. V. McEvilly, Periodic Pulsing of Characteristic Microearthquakes on the San Andreas fault, *Science*, 303, 220-222, 2004.
- Prescott, W.H. and R. O. Burford, Slip on the Sargent Fault, *BSSA*, 66(3): pages 1013-1016, June 1976
- Reasenber, P. A. and R. W. Simpson, Response of Regional Seismicity to the Static Stress Change Produced by the Loma Prieta Earthquake, *U.S.G.S. Professional Paper 1550-D*, pages D49-D71, 1997.
- Simpson R. W. and P. A. Reasenber. Earthquake Induced Static Stress Changes on Central California Faults, *U.S.G.S. Professional Paper 1550-F*, pages F55-F89, 1994.

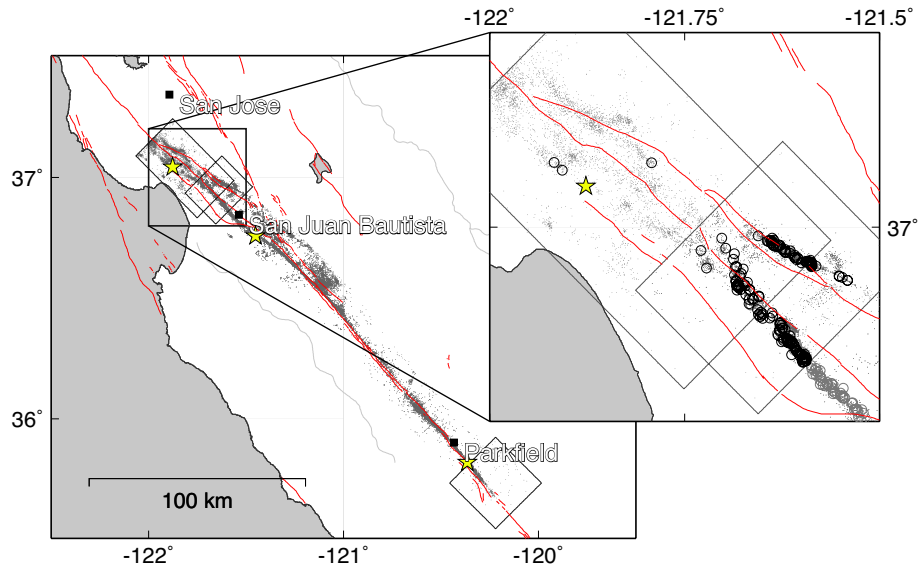


Figure 2.14: Background seismicity in gray points, newly discovered repeaters in black circles (inset). Boxes show extensions of existing catalog. Stars show epicenters of LP EQ and 2004 Parkfield event.

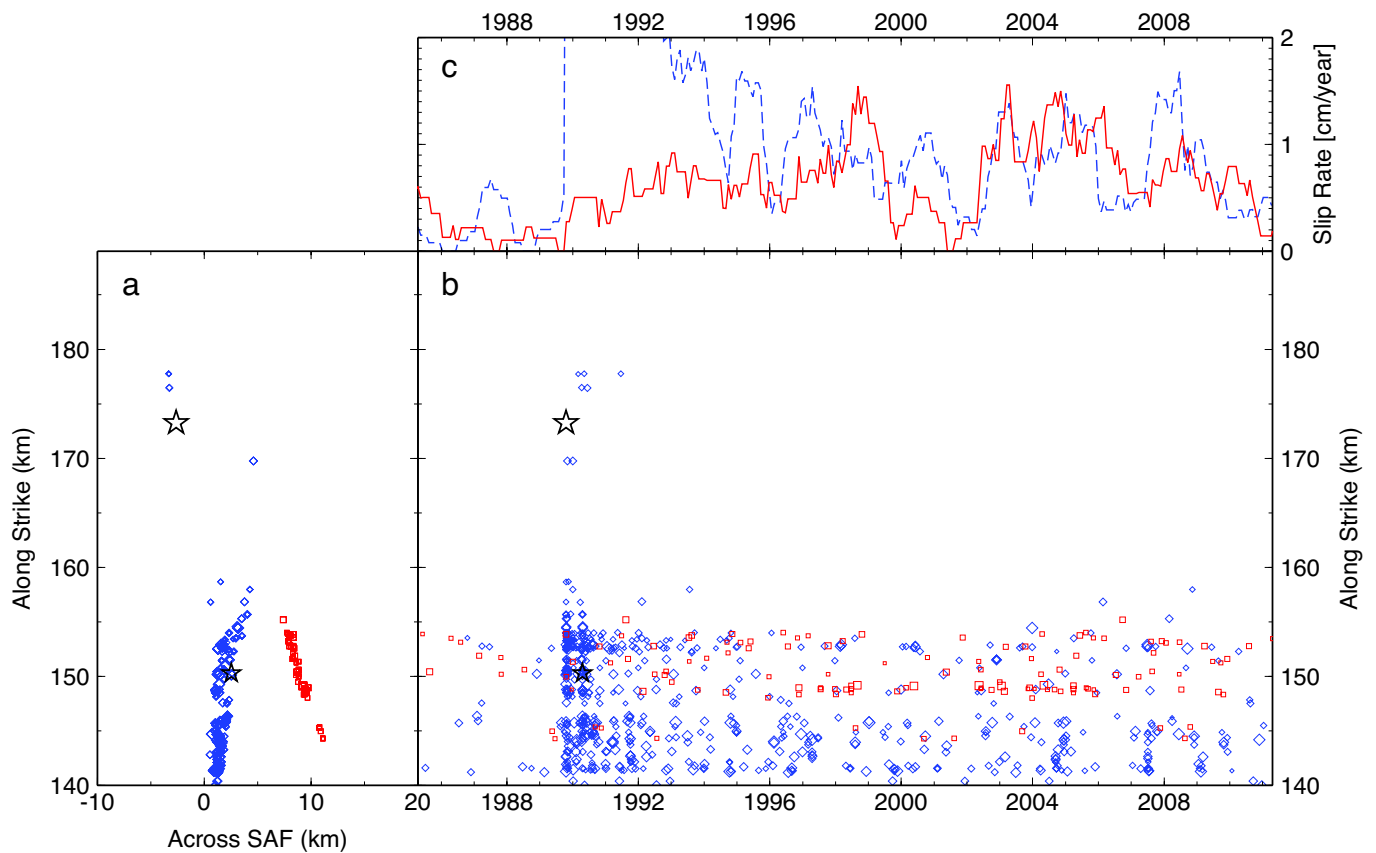


Figure 2.15: a) Repeaters in map view where the y-axis is the distance along strike from Parkfield and the x-axis is the distance from the general strike of the SAF. b) Repeaters in time, along strike. c) Slip rates in cm/yr, calculated from repeating earthquake sequences. Slip rates on the SAF immediately after LP are well off this scale, maxing out at ~ 20 cm/yr. Blue/diamond/dashed events are on the SAF, red/square/solid on the SF.

8 Surface Slip during Large Owens Valley Earthquakes from EarthScope Lidar

Elizabeth Haddon (SFSU), Colin Amos, Roland Bürgmann

8.1 Introduction

The moment magnitude (M_w) 7.4-7.9 Owens Valley earthquake of 1872 is one of the three largest historic earthquakes to impact the state of California. Despite a rupture length of less than 120 km (Amos *et al.*, 2012), ground motions associated with this event were similar or stronger at regional distances compared to large San Andreas earthquakes (Hough and Hutton, 2008). Recent availability of high-resolution lidar topography spanning the surface rupture enables reevaluation of the amount and extent of surface slip during the 1872 and earlier events. These refined paleoseismic parameters allow better characterization of the estimated moment release associated with Owens Valley surface ruptures.

8.2 Methods

We capitalize on the 2007 EarthScope lidar topographic dataset to locate, assess and measure laterally displaced geomorphic features using high-resolution (50 cm) bare-earth topography and analysis tools recently developed and described in Zielke *et al.* (2012). We compile over fifty new measurements of lateral offset, and, where possible, test the precision of lidar-based methods by comparing our results to the published measurements of surface slip during the 1872 event (Figure 2.16). Assuming that channel incision generally occurs on shorter timescales than earthquake events, the smallest offsets correspond to the 1872 event. Similarly, progressively larger-offset groups are attributed to earlier surface ruptures.

8.3 Findings

Our preliminary findings shed light on the history and size of paleoearthquakes on the Owens Valley fault. The cumulative density of lateral offset measurements is distinctly peaked at values corresponding to the most recent event and earlier surface ruptures. Our results suggest that the horizontal displacement for the 1872 Owens Valley earthquake averaged 4.9 ± 1.1 m (Figure 2.16). This value is similar to, albeit smaller than, previous estimates based on field measurements (6 ± 2 m; Beanland and Clark, 1994). A subsidiary peak at ~ 8 m may reflect slip variability during the 1872 rupture, or a smaller event with a poorly understood spatial extent. A more prominent peak occurs at 12.5 ± 1.2 m, possibly corresponding to the penultimate earthquake (PE), which occurred at ca. 10 ka (Bacon and Pezzopane, 2007). If so, the total slip distribution implies a similar rupture length for

1872 and the PE (Figure 2.17). A less-distinct peak of cumulative offsets that cluster at 17.7 ± 1.8 m may represent the antepenultimate event (APE, Figure 2.16). This event implies a similar magnitude of surface slip (ca. 5 m) to the 1872 surface rupture. Taken together, our results imply some variability in the amount of surface slip during Owens Valley surface ruptures, although it appears that large earthquakes repeatedly rupture the same fault extent.

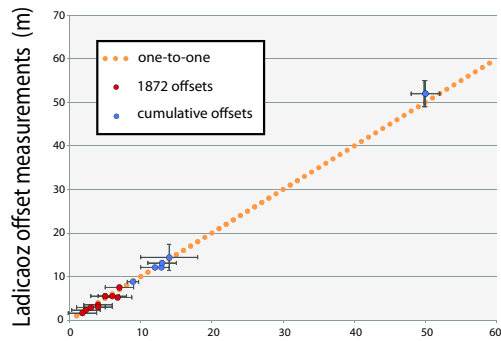
The revised average value of lateral offset of 4.9 ± 1.1 m favors an estimated M_w 7.6 for the 1872 Owens Valley using the scaling relationships of Wells and Coppersmith (1994) and a fault width of ~ 20 km (Hough and Hutton, 2008). As such, anomalously high ground motions observed at regional distances may result from attenuation differences (Bakun, 2006; Hough and Hutton, 2008) or differences in the energetics of Owens Valley surface ruptures in comparison with San Andreas events.

8.4 Acknowledgements

This research is supported by Southern California Earthquake Center Award 12140.

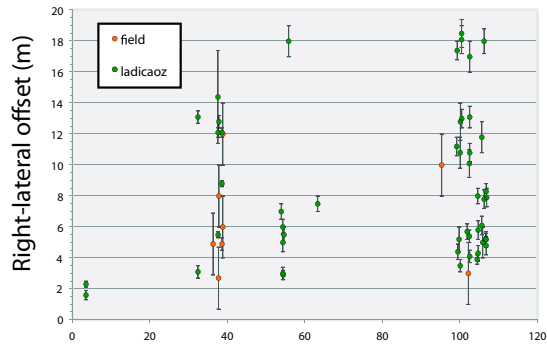
8.5 References

- Amos, C. B., Lutz, A., Unruh, J. R., Jayko, A. S., and Mahan, S. A., 2012, Refining the southern extent of the 1872 Owens Valley earthquake rupture - Paleoseismic investigations at Sage Flat and Haiwee Meadows, California, Final Technical Report to the U.S. Geological Survey National Earthquake Hazards Reduction Program, Award Number G09AP00133.
- Beanland, S., and Clark, M.M., 1994, The Owens Valley fault zone, eastern California, and surface faulting associated with the 1872 earthquake: *U.S. Geological Survey Bulletin* 1982, 29 p.
- Bacon, S. N., and Pezzopane, S. K., 2007, A 25,000-year record of earthquakes on the Owens Valley fault near Lone Pine, California: Implications for recurrence intervals, slip rates, and segmentation models: *Geological Society of America Bulletin*, v. 119, no. 7-8, p. 823-847.
- Bakun, W. H., 2006, MMI attenuation and historical earthquakes in the Basin and Range province of western North America: *Bull. Seismol. Soc. Am.* 96, 2206-2220.
- Hough, S. E., and Hutton, K., 2008, Revisiting the 1872 Owens Valley, California, earthquake: *Bulletin of the Seismological Society of America*, v. 98, no. 2, p. 931-949.
- Wells, D., and K. Coppersmith, 1994, New empirical relationships among magnitude, rupture length, rupture width, rupture area, and surface displacement: *Bull. Seismol. Soc. Am.* 84, 974-1002.
- Zielke, O., Arrowsmith, J. R., 2012, LaDiCaoz and LiDARimager - MATLAB GUIs for LiDAR data handling



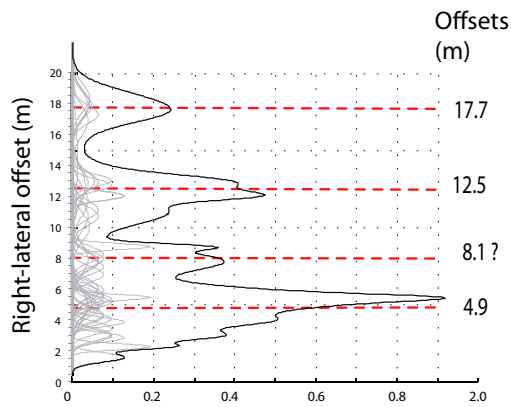
A

Field offset measurements (m)



B

Distance from southern rupture boundary (km)



C

Cumulative kernel offset density

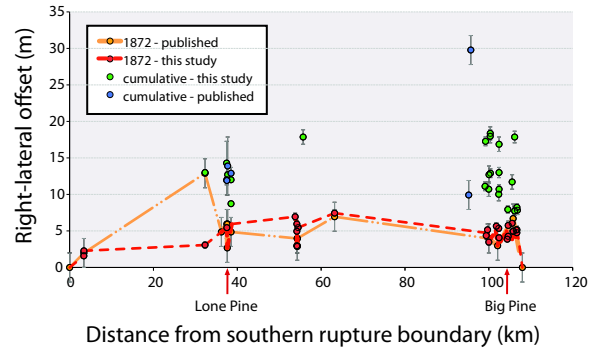


Figure 2.17: Surface slip distribution associated with the 1872 event (red line). Our measurements suggest average dextral slip of 4.9 ± 1.1 m in 1872. The orange line represents the slip distribution as determined by previous field investigations.

and lateral displacement measurement: *Geosphere*, February 2012; v. 8; no. 1; p. 206-221.

Figure 2.16: (A) Plot of lidar field-derived lateral offset measurements. Lidar measurements were made using the LaDi-CaOZ MATLAB graphical user interface. (B) Compiled lateral offset measurements spanning the length of the OVF. (C) The cumulative density of offset measurements is distinctly peaked at 4.9 ± 1.1 m, corresponding to surface slip during the 1872 event. Other peaks may correspond to cumulative offset from earlier events.

9 Testing the Temporal Persistence of Slip Rate Along the Little Lake Fault, Eastern California Shear Zone

Colin Amos, Sarah Brownlee (Wayne State), Dylan Rood (LLNL), Roland Bürgmann, G. Burch Fisher (UCSB), Paul Renne (BGC), Angela Jayko (USGS)

9.1 Introduction

In the eastern California shear zone (ECSZ), short-term interseismic strain rates measured from geodesy outpace longer-term geologic measurements of fault slip-rate by a factor of about two. This discrepancy characterizes slip rates both summed across the zone as a whole (Oskin *et al.*, 2008) and along individual structures. An early InSAR study in the northern Mojave Desert (Peltzer *et al.*, 2001) exemplifies the latter through demonstration of rapid interseismic deformation focused on the Little Lake and Blackwater faults (Figure 2.18). The magnitude of this strain suggests up to 7 mm/yr of dextral strike slip, despite modest Quaternary slip-rates of 0.5 mm/yr for the Blackwater fault (Oskin and Iriondo, 2004). Conversely, the sinistral Garlock fault, a cross-cutting conjugate to the Little Lake - Blackwater faults displays the opposite sense of rate discrepancy. There, geodetic data indicates that interseismic strain accumulates at a slower average rate than suggested by older, offset geologic markers (Figure 2.19). A potential explanation for this mismatch is that the Garlock and Little Lake-Blackwater faults undergo alternating periods of relatively slow and fast fault slip, corresponding with earthquake clusters along each zone (Dolan *et al.*, 2007). As such, understanding the nature of short and long-term variations in fault slip-rate in the ECSZ has clear implications for seismic hazards in southern California, as well as for interactions and interconnectivity among fault networks within zones of distributed shear.

9.2 Methods

Here, we test the persistence of rapid, decadal strain accumulation along the Little Lake fault (Figure 2.18) through combination of new geologic fault slip-rates and InSAR measurements. Geologic constraints exploit a series of fluvial landforms spanning the Little Lake fault, emplaced during intermittent outflows of the Pleistocene Owens River. New geologic mapping and ground-based lidar surveying of these features provide fault-slip measurements for landforms of varying age. Geochronologic control on these features relies on new $^{40}\text{Ar}/^{39}\text{Ar}$ dating of Quaternary basalts and ^{10}Be exposure dating of outwash boulders on Late-Pleistocene terrace surfaces. New measurements of interseismic strain spanning the Little Lake - Blackwater and Garlock faults utilize an updated catalog of ERS and Envisat data spanning the last decade and a half.

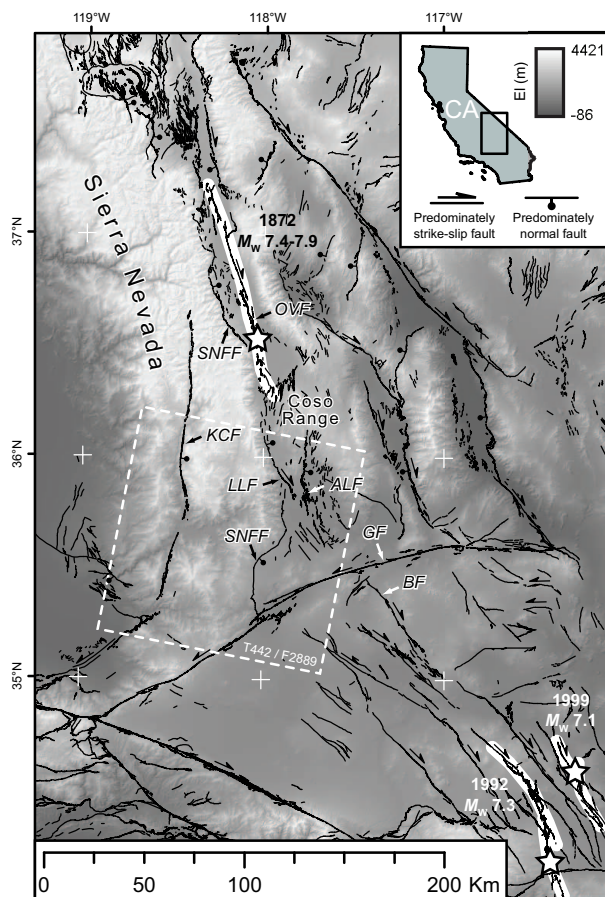


Figure 2.18: Overview of active faults and regional topography of the eastern California shear zone (ECSZ) and southern Walker Lane belt (WLB). Labeled faults are abbreviated as follows: ALF-Airport Lake fault, BF-Blackwater fault, GF-Garlock fault, KCF-Kern Canyon fault, LLF-Little Lake fault, OVF-Owens Valley fault, SNFF-Sierra Nevada frontal fault. Major historical earthquake surface ruptures in the ECSZ and WLB are outlined in white, with stars denoting epicentral locations. Radar scene T442/F2889 is outlined by the dashed white box.

9.3 Findings

Geologic slip rates measured from displaced landforms along the Little Lake fault suggest modest, sustained dextral slip averaging ca. 0.7 mm/yr over the past ca. 65 to 200 ky (Figure 2.19). This rate agrees well with Qua-

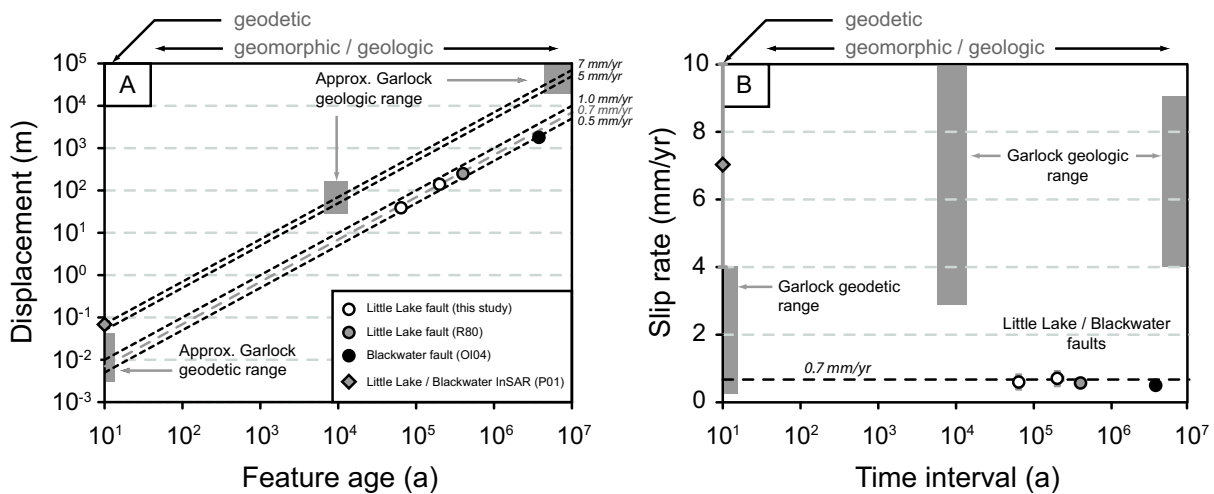


Figure 2.19: Compiled dextral displacements (A) and corresponding fault slip rates (B) as a function of age for the Little Lake, Blackwater, and Garlock faults. Linear regressions in (A) indicate constant slip rates through time. Geodetic measurements represent interseismic deformation measured from InSAR and GPS. See *Ganev et al. (2012)* for a summary of Garlock fault measurements. References in legend: OI04 - *Oskin and Iriondo (2004)*; P01 - *Peltzer et al. (2001)*; R80 - *Roquemore (1980)*.

ternary averaged slip rates along the Blackwater fault, and is substantially slower than geologic slip rates for the Garlock structure. As such, our data suggests that temporal variations in slip, if they occur, happen at shorter time scales than 10^4 - 10^5 years. Although feasible at the time scale of individual earthquakes or earthquake clusters (10^3 yr), our preliminary InSAR results demonstrate similar, modest rates of interseismic strain accumulation along the Little Lake fault. Taken together, our work suggests that relatively rapid strain measured in earlier InSAR studies is transient over decadal periods and does not reflect long-term oscillations between the Little Lake-Blackwater and Garlock faults. Future work will better constrain recent rates of interseismic strain accumulation in this area using InSAR and will investigate the possibility that short-term interseismic strain transients reflect fault interaction and acceleration following nearby earthquakes in the ECSZ (Figure 2.18).

9.4 Acknowledgements

This research was supported by NSF Postdoctoral Fellowship Award EAR0847990 to Amos.

9.5 References

- Dolan, J. F., Bowman, D. D., and Sammis, C. G., 2007, Long-range and long-term fault interactions in Southern California: *Geology*, v. 35, no. 9, p. 855-858.
- Ganev, P. N., Dolan, J. F., McGill, S. F., and Frankel, K. L., 2012, Constancy of geologic slip rate along the central Garlock fault: implications for strain accumulation and release in southern California: *Geophysical Journal International*, in press.

Oskin, M., and Iriondo, A., 2004, Large-magnitude transient strain accumulation on the Blackwater fault, Eastern California shear zone: *Geology*, v. 32, no. 4, p. 313-316.

Oskin, M., Perg, L., Shelef, E., Strane, M., Gurney, E., Singer, B., and Zhang, X., 2008, Elevated shear zone loading rate during an earthquake cluster in eastern California: *Geology*, v. 36, no. 6, p. 507-510.

Peltzer, G., Crampe, F., Hensley, S., and Rosen, P., 2001, Transient strain accumulation and fault interaction in the Eastern California shear zone: *Geology*, v. 29, no. 11, p. 975-978.

Roquemore, G., 1980, Structure, tectonics, and stress-field of the Coso-Range, Inyo-County, California: *Journal of Geophysical Research*, v. 85, no. NB5, p. 2434-2440.

10 Examining the Mechanical Behavior and Evolution of the Southern San Andreas Fault System through Determination of Late Quaternary Slip Rates and Distinct Element Simulations

Kimberly Blisniuk, Roland Bürgmann, Juli Morgan (Rice University), Tom Fournier (Rice University), Warren Sharp (Berkeley Geochronology Center)

10.1 Introduction

To better understand the processes driving the kinematic and mechanical evolution of the southern San Andreas Fault System (SAFS) we combine (1) geologic field mapping of offset landforms, (2) Quaternary geochronology to obtain precise estimates of fault slip rates, and (3) distinct element models (DEM) to simulate the behavior and interactions of faults within the system. The southern San Andreas fault zone of the SAFS is an ideal structure to investigate and model processes of crustal deformation because a high rate of strain is localized on a relatively simple set of faults, the Mission Creek and Banning faults. Furthermore, it is the most poorly understood section of the southern SAFS with respect to slip rate and timing of past large-magnitude earthquakes; therefore, its seismic hazard is difficult to quantify. Nonetheless, the seismic hazard that it presents is likely to be high since this section of the fault system is the only major section that has not ruptured in historic time. The last earthquake to rupture occurred over 300 years ago c. 1690. Accordingly, the long lapse time since the last surface rupture implies that this section of the SAFS is in the late phase of its earthquake cycle, and that strain accumulated over the past 300 years is likely to be relieved in a large-magnitude earthquake.

10.2 Preliminary Field Observations and Sample Collection

Four study sites located on the southern San Andreas fault zone have been identified to constrain geologic slip rates. At these sites, we have conducted detailed geomorphic mapping and initial sample collection from: (1) 2 of 3 channels completely beheaded from Pushawalla Canyon offset by the Mission Creek fault (Figure 2.20); (2) offset late Pleistocene and Holocene alluvial fan deposits (assessed based on surface and soil characteristics) on the Mission Creek fault at Dell Wash, just south of Pushawalla Canyon (Figure 2.20); (3) a late Pleistocene fan deposit offset by the Banning fault located between Thousand Palms Canyon and Pushawalla Canyon (Figure 2.20); and (4) an offset Holocene alluvial fan deposit (assessed based on surface and soil characteristics) offset along 2 strands of the Mission Creek fault at Thermal Wash (not shown).

10.3 Geochronology

Multiple Quaternary dating techniques, namely, surface exposure using cosmogenic ^{10}Be isotopes and U-

series of pedogenic carbonate clast-coatings, will be applied to reliably constrain fault slip rates. The combination of these methods can significantly improve the reliability of landform dating because exposure ages from cosmogenic isotopes can be biased by post-depositional surface processes and inherited nuclides, while U-series dating of pedogenic carbonate provides minimum ages for alluvium because carbonate accumulation ensues after deposition of the host material. However, the factors controlling precision and accuracy of the two techniques are relatively independent. Thus, combining them can significantly improve the reliability of landform dating and ultimately yield more accurate slip rates.

10.4 Distinct Element Models

To illustrate the potential of DEMs, scaled 2-D simulations of a fault zone comprising two fault strands (1 km long, spaced 0.6 km across) are shown in Figure 2.21. In the model, $\sim 15,000$ particles with radii of 3 to 4 m are confined between two horizontal walls, and interparticle bonds with an interparticle friction of 0.3 are applied at the contacts, except along two prescribed fault surfaces (F1 and F2 in Figure 2.21) within the domain. Moving the top and bottom walls in opposite directions, under constant confining pressure, imposes right-lateral shear strain on the zone. As expected, shear deformation is localized onto the prescribed fault surfaces. The two fault strands exhibit rapid temporally variable activity as slip transfers between them; slip along the fault surfaces also varies spatially, as a function of fault locking and release, which is directly correlated with increasing and decreasing differential stress. In this scaled system, individual fault strand inactivity can persist for as long as 30 increments (i.e., ~ 13.5 m of relative wall displacement). In a general sense, the duration of fault inactivity is proportional to the applied normal stress, reflecting its influence on fault locking. This shows that 2-D DEMs may be a useful tool to evaluate the observed patterns of fault system behavior, as they permit the tracking of fault evolution and associated local stress field changes, which can highlight specific mechanical processes governing deformation across the SAFS.

10.5 Acknowledgements

This project is funded by NSF's Earth Science Postdoctoral Fellowship program awarded to Kimberly Blis-

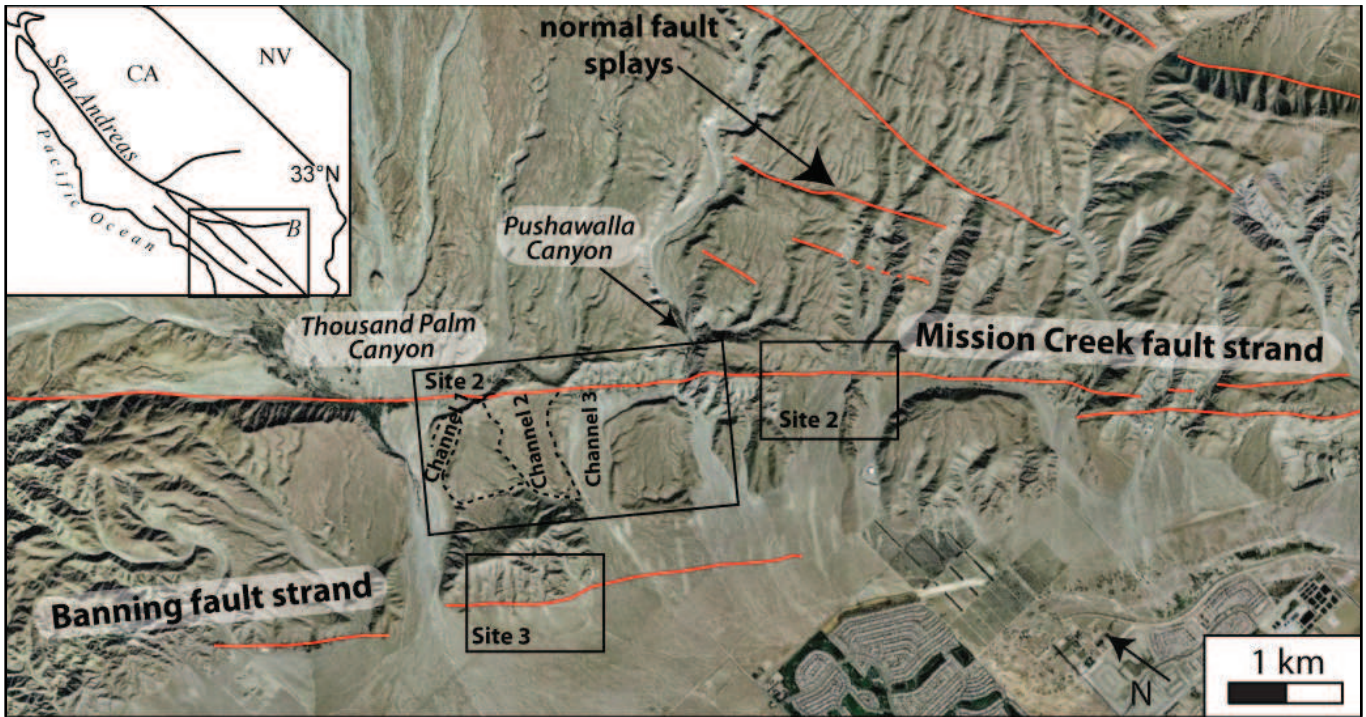


Figure 2.20: Preliminary interpretation of a GoogleEarth image of sites 1 through 3 (Indio Hills/Thousand Palms Oasis) showing the location of dextrally offset channels and alluvial fans along the Mission Creek and Banning faults of the southern San Andreas fault zone.

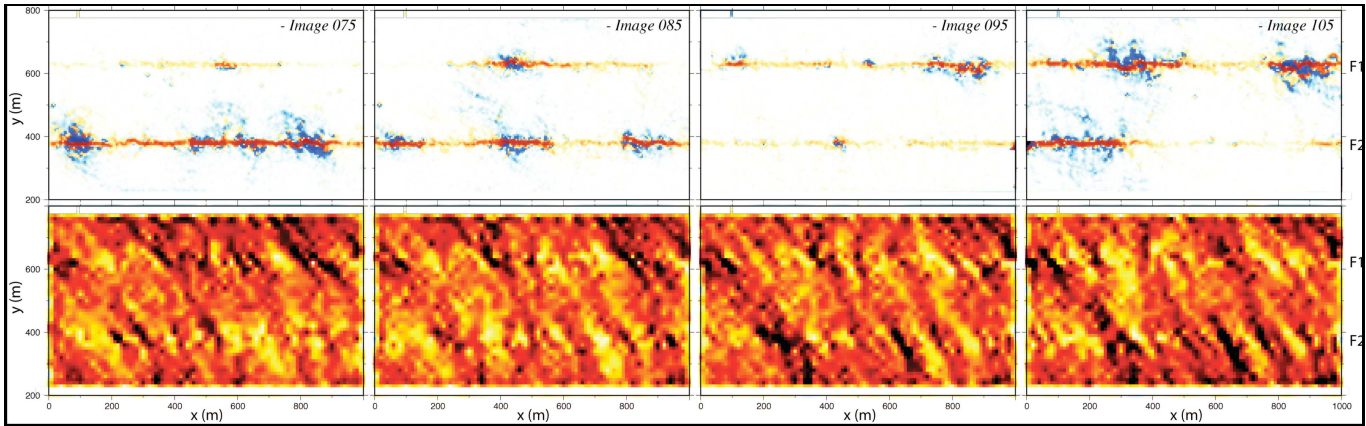


Figure 2.21: Sequence of incremental strain (top panels) and differential stress (bottom panels) distributions in a simulated two fault system, undergoing right lateral shear at a constant far-field strain rate, under a confining pressure of 30 MPa. Images record incremental slip over 0.45 m of relative wall displacement (0.075 % shear strain), but are plotted at intervals of 4.5 m displacement. Red and blue colors denote right- and left-lateral shear strain, respectively, with color intensity scaled with slip magnitude. Right-lateral slip is localized onto the fault surfaces, but shows significant variations over time, and transfer of slip between fault strands. Blue "bursts" adjacent to the fault surfaces indicate earthquake-like slip events on the fault strand as locked zones are released, causing rebound of the adjacent wall rocks. Inclined zones of high differential stress (hotter colors) support compressive stresses within the domain, and correlate with locked zones along the faults. Stress releases correspond with fault rupture events (Images courtesy of J. Morgan and T. Fournier).

niuk under grant number NSF EAR-0757608

11 Investigating Fault Slip Budget in the Mendocino Triple Junction

Taka'aki Taira

11.1 Introduction

High-quality seismic and geodetic data from dense networks have revealed that the Mendocino Triple Junction (MTJ) Zone, California experiences a wide variety of transient fault slip, including earthquakes, slow slip events, and tectonic tremors (Figure 2.22a). Detecting these transient deformation fields with estimations in the locations of responsible deformation areas is a fundamental first step in addressing the slip budget in the MTJ zone. Additionally, an analysis of historical seismic data continuously recorded by broadband seismic stations identifies characteristically repeating earthquake sequences along the Mendocino Fracture Zone. Spatiotemporal properties in these sequences would allow us to infer aseismic fault slip surrounding the sequences.

11.2 Transient Deformation in 2008

Geodetic measurements of the MTJ zone with GPS arrays detected an aseismic slip episode with the west component of displacement up to 8 mm (Figure 2.22b). GPS time series have suggested that this aseismic slip episode may have nucleated near Weaverville, CA in March 2008 and propagated to the northwest over a 2-month period. At the same time, broadband seismic records have revealed that an area of northernmost California (e.g., Yreka) experienced an episode of tectonic tremors. Tectonic tremor observed consists of intermittent weak seismic signals at relatively low frequency (1-5 Hz). An array of broadband stations (~ 30 stations) was temporally deployed at the Cape Mendocino area in 2007-2009 through the Flexible Array Mendocino Experiment (e.g., *Porritt et al.*, 2011). These Mendocino broadband data significantly improve detectability of tectonic tremor signals and enhance the spatial resolution in the locations of tectonic tremors. We systematically analyzed high-quality broadband data to identify and locate tectonic tremors. Following *Ide* (2012), we used a waveform-envelope correlation method to detect tectonic tremors. Our analysis showed that a slow migration occurs parallel to the strike of the subducting slab at an average velocity of about 3-4 km/day (Figure 2.23). The observed temporal correlation between the aseismic slip transient and the tectonic tremor activity may suggest that a single mechanism is mainly responsible for nucleating these transient deformations. We also note that toward the end of the transient deformations (e.g., aseismic slip and tremor) in the end of April 2008, a normal-faulting event with $M_w=5.3$ occurred around the aseismic deformation area. Although we do not yet estimate the spatial extent of

the aseismic slip transient and its temporal behavior, the stress from the aseismic slip transient may have triggered this extensional earthquake. Similar stress interactions between aseismic slip transients and extensional earthquake activity are observed in other subduction zones. *Liu et al.* (2007) have observed a cluster of extensional earthquakes in Guerrero, Mexico during 2006 that is temporally correlated with a large aseismic deformation transient. The Guerrero observation in *Liu et al.* (2007) showed that the extensional earthquakes corresponded to the initiation of the aseismic deformation transient, indicating that the aseismic deformation transient seems to be initiated by extensional earthquakes. Thus, the underlying mechanisms of the sequential transient deformations observed in the MTJ zone and in the Guerrero region would be different. Nevertheless, we speculate that similar stress transfer processes are involved in these two sequential deformations.

11.3 Characteristically Repeating Microearthquakes

By utilizing waveforms from $\sim 5,000$ MTJ local earthquakes ($M > 2.5$ in 1992-2011), we have been identifying repeating microearthquakes in the MTJ zone (Figure 2.24), detecting numerous and distributed sites of repeating microearthquake activity along the Mendocino Fracture Zone (red circles shown in Figure 2.22a). Their recurrence intervals are about 2-3 years, which may be the result of aseismic fault slip surrounding the sequences.

11.4 Acknowledgements

This work is supported by the U.S. Geological Survey NEHRP program under grant number G11AP20168.

11.5 References

- Ide, S., Variety and spatial heterogeneity of tectonic tremor worldwide, *J. Geophys. Res.*, *117*, B03302, doi:10.1029/2011JB008840, 2012.
- Liu, Y., J.R. Rice, K.M. Larson, Seismicity variations associated with aseismic transients in Guerrero, Mexico, 1995-2006, *Earth and Planetary Science Letters*, *462*, 493-504, 2007.
- McCrorry, P.A., J.L. Blair, D.H. Oppenheimer, S. R. Walter, Depth to the Juan de Fuca slab beneath the Cascadia subduction margin: A 3-D model for sorting earthquakes, U. S. Geol. Surv. Data Series, DS-91, 2004.
- Porritt, R.W., R.M. Allen, D.C. Boyarko, M.R. Brudzinski, Investigation of Cascadia segmentation with ambient noise tomography, *Earth Planet. Sci. Lett.*, *185*, 67-76, doi:10.1016/j.epsl.2011.06.026, 2011.

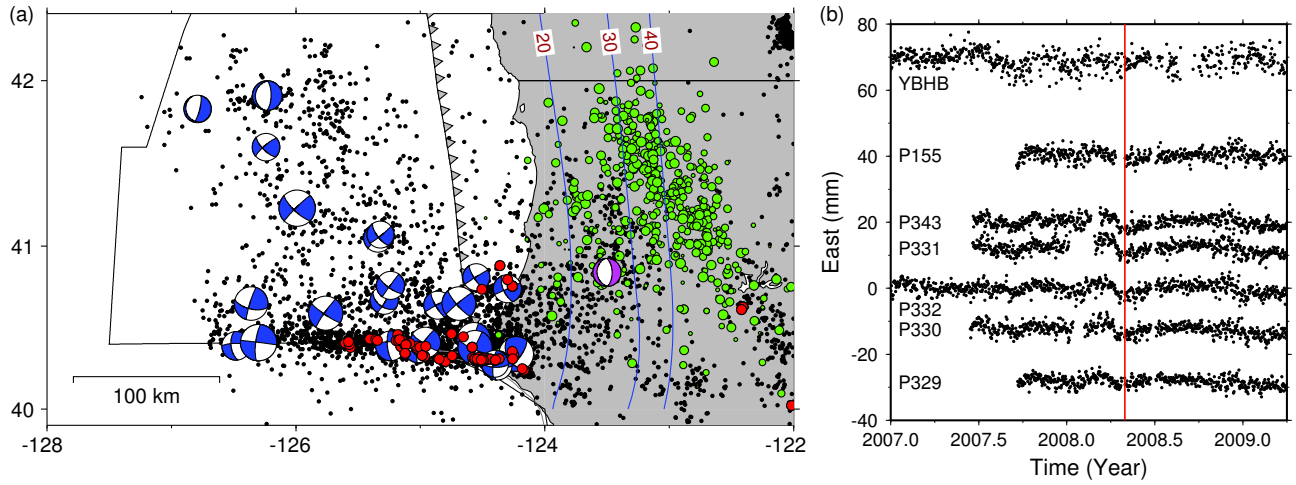


Figure 2.22: (a) Location of the MTJ earthquakes (black circles) between 1984 and present from the Northern California Earthquake Data Center (NCEDC) catalog. Green circles are identified tectonic tremors in 2008, identified from our analysis. Red circles are characteristically repeating earthquake sequences. Also shown are focal mechanisms for $M > 5$ earthquakes determined from the NCEDC moment tensor analysis. The purple one is the 2008 M_w 5.3 normal-faulting earthquake. Blue lines are the plate interface from *McCrory et al.* (2004). (b) GPS time series in the east-west component determined by the Pacific Northwest Geodetic Array (PANGA). Black positions are daily GPS station positions in mm. The red line is the occurrence of the 2008 M_w 5.3 normal-faulting earthquake.

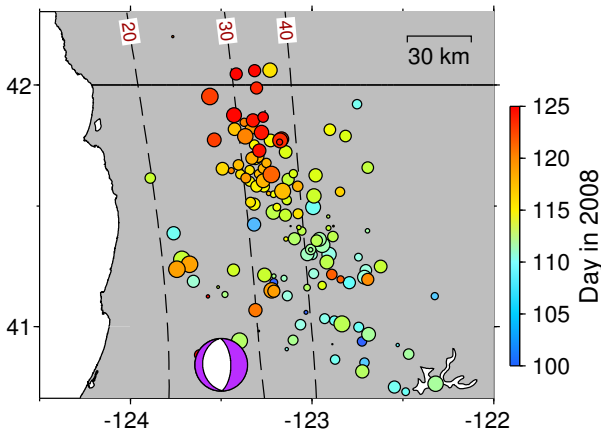


Figure 2.23: Tremor epicenters (circles color coded by time) during the transient deformation in 2008. About 150 tectonic tremors are identified. The circle sizes are inversely proportional to the uncertainty in the tremor locations. The focal mechanism shown in purple is the 2008 M_w 5.3 normal-faulting earthquake. Also shown is the plate interface geometry (contoured at 10-km intervals) from *McCrory et al.* (2004).

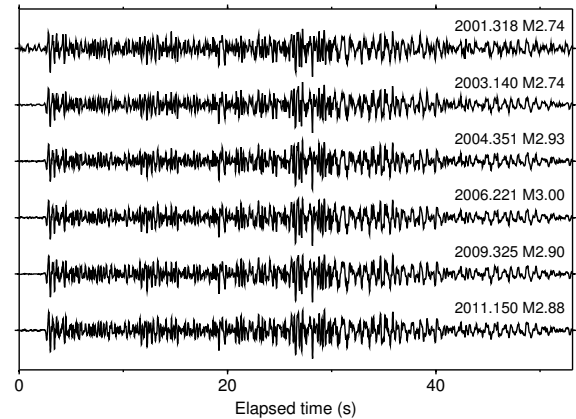


Figure 2.24: Repeating earthquake sequences identified in our analysis recorded at station WDC. The average event magnitude is around 2.8.

12 Incipient Faulting near Lake Pillsbury, CA

Amanda M. Thomas, Roland Bürgmann, Douglas S. Dreger

12.1 Anomalous Seismic Activity

In March of 2000, a swarm of earthquake activity lasting approximately six months and culminating in an M_w 4.4 earthquake occurred along the eastern edge of the Middle Mountain block (Hayes *et al.*, 2006), between the Ma'acama and Bartlett Springs faults in Northern California. The swarm began with a month-long period of intense microseismicity that preceded the shallow M_w 4.4 event which occurred on May 17, 2000. Over the course of the next three months, microseismicity at depths of 3 to 8 km propagated to the southeast and eventually a second large M_w 4.0 earthquake occurred at the southeast end of the seismic lineament. The area sustained elevated earthquake activity for the next 6 years and between 2006 and 2007 another intense swarm culminated in a M_w 4.8 earthquake. This event was similarly preceded by very energetic microseismicity.

Precise earthquake locations (Waldhauser *et al.*, 2008) from both swarms illuminate discontinuous, geometrically complex structures that roughly parallel the strike of faults within the San Andreas fault (SAF) system. In the south, a small fraction of the seismicity occurs shallowly around 2 km, however the majority of hypocenters are aftershocks of the M_w 4.0 event and cluster between 5 and 8 km depth on a plane dipping 70°NE. Continuing northwest along strike, seismicity shallows and localizes onto a near vertical structure extending from 1 to 6 km depth, near the hypocenter of the M_w 4.4. Further north, shallow, diffuse seismicity extends between the surface and 3 km depth and hypocenters are located as much as 3 km off fault. In this same area deeper events, which mostly consist of aftershocks from the M_w 4.8 event, delineate a N-S striking plane dipping 70°NE.

To further constrain the geometry and structural maturity of the lineament we compute double-couple focal mechanisms for all events with 25 or more first motion observations and full-waveform moment tensors for the three largest events (Hardebeck and Shearer, 2002; Dreger *et al.*, 2000). First motion solutions generally have large uncertainties in strike, rake, and dip, which are primarily due to gaps in the takeoff angle particularly before the installation of the Transportable Array stations prior to the 2006-7 swarm. However, the similarity of nearby first motion solutions and agreement with the independent analyses of McLaren *et al.* (2007) and Hayes *et al.* (2006) suggests that solutions may be useful in constraining lineament geometry. Figure 1 compares the moment tensor solutions for the 2000 M_w 4.4, 2000 M_w 4.0, and 2007 M_w 4.8 earthquakes, populations of fault plane so-

lutions of nearby earthquakes, and the geometry defined by the earthquake hypocenters. In the southern swarm, focal mechanism and moment tensor solutions indicate that nearly all events are right-lateral strike-slip earthquakes that occur on structures striking parallel to the Ma'acama and Bartlett Springs faults. Some of these events, particularly those associated with the M_w 4.4, occur on vertically dipping fault planes, however others, including the M_w 4.0, slip on more shallowly dipping structures that are not optimally oriented. In the northern swarm, mechanisms are highly variable and consist of predominantly right-lateral strike-slip and normal faulting events. Both the first motions and hypocenter locations indicate faulting below 2 km depth occurs along a N10°W trending plane that dips 70°E. The moment tensor solution for the M_w 4.8 has a similar strike but dips 79° which differs by 9° from the dip inferred from the hypocenters. The 90% confidence interval on the dip angle of M_w 4.8 solution spans a dip range that includes 70°, however the 80% confidence intervals do not, suggesting this event may have slipped on a plane with a different orientation than that delineated by the hypocenters. While uncertainties in the best-fit geometries were not considered we note this discrepancy because it suggests that the M_w 4.8 may have involved the fracture of intact rock.

12.2 Comparison to Incipient Faulting in the Field

Earthquake swarms are a relatively common occurrence and have been linked to aseismic slip, pore fluid migration, and volcanic activity (see Roland and McGuire, 2009 and references therein). The geometric complexity, earthquake hypocenters, and focal mechanisms of the seismic lineament suggest that it may be an incipient fault (Bawden *et al.*, 1999). Similar fault geometries have been documented extensively in field studies of the initial stages of shear zone development (Martel, 1988). Structural complexity arises for two reasons. First, faults take advantage of preexisting weaknesses, which may have developed in either an earlier tectonic event or in the same tectonic event (Crider and Peacock, 2004). These zones of weakness typically have poor connectivity and are generally neither coplanar nor optimally oriented. Second, to form a through-going fault while still exploiting these weaknesses, secondary fractures are generated in response to the stress fields surrounding en echelon cracks (Martel *et al.*, 1988; Martel, 1990; Crider and Peacock, 2004). Similarly, the seismic lineament is

structurally segmented with abrupt changes in geometry between the south and north and a general lack of any geometric definition in the shallow events in the north. The colocation of the lineament and the Bucknell Creek fault in the south and with relic dipping structures in the north suggests the lineament may be exploiting pre-existing structure as it propagates northward. Additionally, many of the normal events have strikes coincident with the \sim N-S direction of the maximum compressive stress suggesting that small-scale extensional faulting occurs between the two structures.

Focal mechanisms and deformation style also vary markedly along strike. In the south first motion mechanisms are mostly right-lateral strike-slip events that have strikes and dips consistent with the structure delineated by the seismicity. In the north, both the variety of mechanisms and the inconsistency between the geometry delineated by the seismicity and that of the moment tensor for the M_w 4.8 event argue for immature faulting. In a survey of northern California focal mechanisms, *Castillo and Ellsworth* (1993) find that right-lateral transform motion between the North American and Pacific Plates often occurs on structures dipping between 50° and 75° . They suggest these structures may have formed as reverse faults in the forearc of the Cascadia subduction zone and furthermore, due to the way in which this deformation is accommodated, will eventually evolve to a more energetically favorable, vertical strike-slip geometry common to the majority of faults within the SAF system (*Castillo and Ellsworth*, 1993). If their interpretation is correct, then the M_w 4.8 earthquake likely reflects the transition between these two styles of deformation because it occurred as a strike-slip event on a 70° dipping structure about 10 km north of the more mature southern section of the Bucknell Creek lineament. Focal mechanisms on the Bartlett Springs fault at roughly the same latitude exhibit a similar transition between deformation on dipping planes to near-vertical geometries (*Castillo and Ellsworth*, 1993). This suggests that preexisting zones of weakness localize deformation which concentrates stresses and facilitates the development of a new fault zone in a mechanically favorable orientation.

12.3 Acknowledgements

This work is funded by the Geological Society of America Student Research Grant and a National Science Foundation Graduate Research Fellowship.

12.4 References

Bawden, G. W., Michael, A. J., and Kellogg, L. H., 1999, Birth of a fault: Connecting the Kern County and Walker Pass, California, earthquakes. *Geology*, v. 27, p. 601-604.

Castillo, D. A., and Ellsworth, W. L., 1993, Seismotectonics of the San Andreas fault system between Point Arena and Cape Mendocino in northern California: Implication for the

development and evolution of a young transform. *Journal of Geophysical Research*, v. 98, p. 65436560.

Crider, J. G., and Peacock, D. C. P., 2004, Initiation of brittle faults in the upper crust: a review of field observations. *Journal of Structural Geology*, v. 26, p. 691-707, doi: 10.1016/j.jsg.2003.07.007.

Dreger, D. S., Tkali, H., and Johnston, M., 2000, Dilational Processes Accompanying Earthquakes in the Long Valley Caldera. *Science*, v. 288, p. 122-125.

Hardebeck, J.L., Shearer P.M., 2002, A New Method for Determining First-Motion Focal Mechanisms. *Bulletin of the Seismological Society of America*, v.92, p.2264-2276.

Hayes, G. P., Johnson C. B., and Furlong K. P., 2006, Evidence for melt injection in the crust of northern California?. *Earth and Planetary Science Letters*, v. 248, p. 638-649, doi: 10.1016/j.epsl.2006.05.008.

Huffman M. E., 1969, Engineering Geology of Garrett Tunnel and Potter Valley Conveyance System. *State of California Department of Water Resources*, Memorandum Report.

Kelsey, H. M., and Carver, G. A., 1988, Late Neogene and Quaternary tectonics associated with northward growth of the San Andreas transform fault, northern California. *Journal of Geophysical Research*, v. 93, p. 47974819.

Martel, S. J., Pollard, D. D., and Segall, P., 1988, Development of simple strike-slip-fault zones, Mount Abbot Quadrangle, Sierra-Nevada, California. *Geological Society of America Bulletin*, v. 100, p. 1451-1465.

Martel, S. J., 1990, Formation of compound strike-slip fault zones, Mount Abbot quadrangle, California. *Journal of Structural Geology*, v. 12, p. 869877, 879882.

McLaren, M. K., Wooddell, K. E., Page, W. D., van der Elst, N., Stanton, M. A., and Walter, S. R., 2007, The McCreary Glade Earthquake Sequence: Possible Reactivation of Ancient Structures Near Lake Pillsbury, Northern Coast Ranges, Mendocino County, California: *Eos Transactions, AGU*, v.88, no.52, Fall Meet. Suppl., Abstract S21A-0245.

Powell, R. E., and Weldon, R. J., 1992, Evolution of the San Andreas fault. *Annual Review of Earth and Planetary Sciences*, v. 20, p. 431-468, doi: 10.1146/annurev.earth.20.1.431.

Roland, E. and J. J. McGuire, 2009, Earthquake Swarms on Transform Faults, *Geophys. J. Int.* v. 178, p. 1677-1690, doi: 10.1111/j.1365-246X.2009.04214.x.

Waldhauser, F. and Schaff, D. P., 2008, Large-scale relocation of two decades of Northern California seismicity using cross-correlation and double-difference methods. *Journal of Geophysical Research*, v. 113, B08311, doi:10.1029/2007JB005479.

13 Measurements of PBO Borehole Seismometer Orientations

Taka'aki Taira, Kathleen M. Hodgkinson (UNAVCO), Otina Fox (UNAVCO), David Mencin (UNAVCO)

13.1 Introduction

Borehole observations from Plate Boundary Observatory (PBO) seismometers yield a substantially lower detection threshold for lower-amplitude earthquakes and non-volcanic tremors. The three components of PBO borehole data have the potential to improve the identification of seismic phases that will provide high-resolution spatio-temporal monitoring of these lower-amplitude tectonic events. However, the orientations of PBO borehole sensors are not yet well-documented because it is fundamentally difficult to install borehole sensors with a specified orientation, particularly in the horizontal component. A robust estimate of borehole sensor orientations is thus very important for fully utilizing borehole seismic data for investigations of earthquake source and Earth structure. We present a simple method for identifying borehole sensor orientations in the horizontal component based on a waveform cross-correlation analysis and show the result for the PBO stations deployed in Anza, California, in which a number of broadband stations are installed near the PBO borehole stations (Figure 2.25). The primary objective of this project is to provide the necessary information in the instrument responses for the PBO borehole seismic sensors, to allow a broad cross-section of the research community to make use of the PBO borehole seismic data.

13.2 PBO Borehole Data

PBO borehole data improve the detectability of lower-magnitude earthquakes (Figure 2.26). The magnitude sensitivity of the Southern California Seismic Network (SCSN) is geared toward providing completeness down to at least M 1.4 in the Anza region (Kane *et al.*, 2007). However, the low noise recordings from a dense array of PBO borehole stations in the Anza region indicate that these stations could be capable of recording events with good signal to noise down to magnitudes approaching 0 (Figure 2.26). These lower magnitude data can provide a significantly greater number of events for investigating the underlying mechanics of the faulting process.

13.3 Horizontal PBO Sensor Orientation

The cross-correlation method used is based on the principle that highly similar long-period waveforms (> 20 s) will be observed at collocated borehole and reference broadband seismic sensors. The method involves performing a grid search over all possible values of sensor azimuths for borehole data, rotating borehole data with

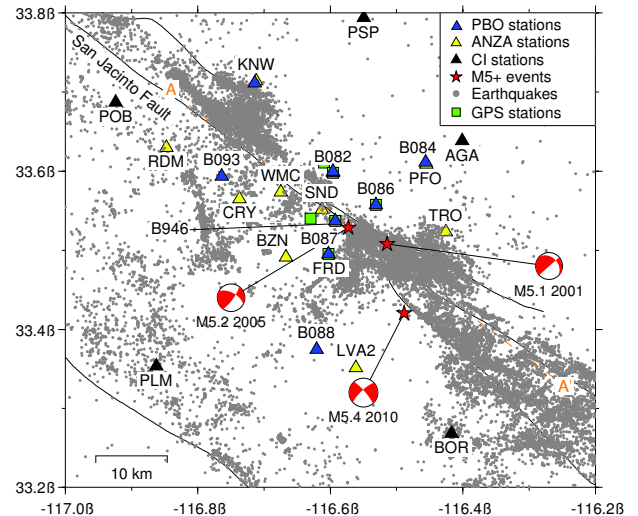


Figure 2.25: Location of the Anza earthquakes (gray circles) during 1984–2005 from *Lin et al.* (2007). Also shown are M > 5 earthquakes (red stars) from the SCSN catalog since 1985. Triangles are seismic stations. Blue triangles are the PBO borehole stations. Black and yellow ones are the USGS seismic stations and the broadband stations of the Anza Broadband Seismic Network, respectively. Also shown are the five GPS stations (green squares).

the assigned sensor azimuth into the transverse and longitudinal directions, and computing the average cross-correlation coefficient between the rotated borehole and reference broadband data for a pair of transverse and longitudinal components. The best-fitting borehole sensor azimuth is identified, in which the average cross-correlation coefficient takes its maximum (dashed red line in Figure 2.27). The 95 percent confidence interval (dashed blue lines in Figure 2.27) is estimated with a Fisher transform (*Baisch and Bokelmann*, 2001).

13.4 References

- Baisch, S., G.H.R. Bokelmann, Seismic waveform attributes before and after the Loma Prieta earthquake: Scattering change near the earthquake and temporal recovery, *J. Geophys. Res.*, 106(B8), 16,323–16,337, doi:10.1029/2001JB000151, 2001.
- Kane, D.L., D. Kilb, A.S. Berg, V.G. Martynov, Quantifying the remote triggering capabilities of large earthquakes using data from The ANZA Seismic Network Catalog (Southern California), *J. Geophys. Res.*, 112, B11302, doi:10.1029/2006JB004714, 2007.

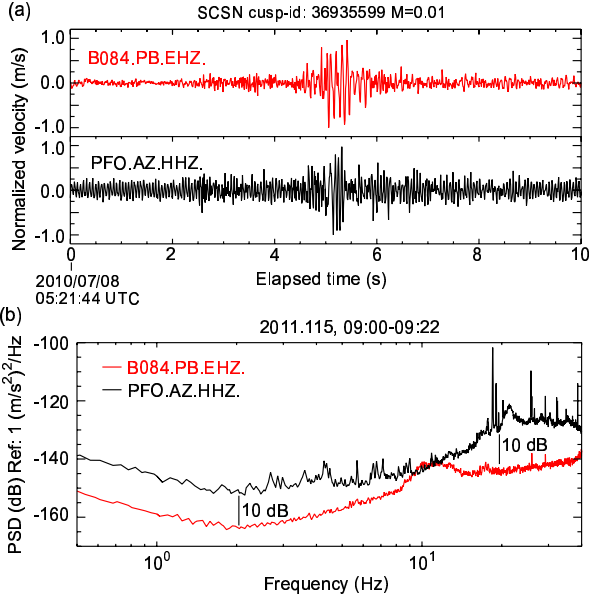


Figure 2.26: Comparison of seismic waveforms recorded at borehole and surface stations. (a) Observed seismograms recorded at the PBO borehole (red, B084) and the ANZA broadband station (black, PFO) for an M 0.01 Anza earthquake. This event is the smallest event in the 2010 M_w 5.4 Anza aftershock sequence listed in the SCSN catalog. A 1.0 Hz highpass filter was applied and the amplitudes of those two waveforms were normalized by their maximum amplitudes. Those two stations are collocated (see Figure 2.25 for the station locations). (b) Power spectral density (PSD) of background noise for the PBO borehole, B084.PB.EHZ (red) and the Anza surface, PFO.AZ.HHZ (black) stations. PSDs were calculated with a \sim 22-minute data window (131,072 data points), 2011.115, 09:00-09:22. This time period was chosen as one of the seismically quiet periods in March through May, 2011 from IRIS quality control measurement results (<http://www.iris.washington.edu/servlet/quackquery/>). This example demonstrates that the noise level of station B084 is \sim 10 dB less than that of station PFO in the frequency range of 1-40 Hz (except for the 8-12 Hz band) and indicates that borehole records allow us to identify lower-magnitude earthquakes.

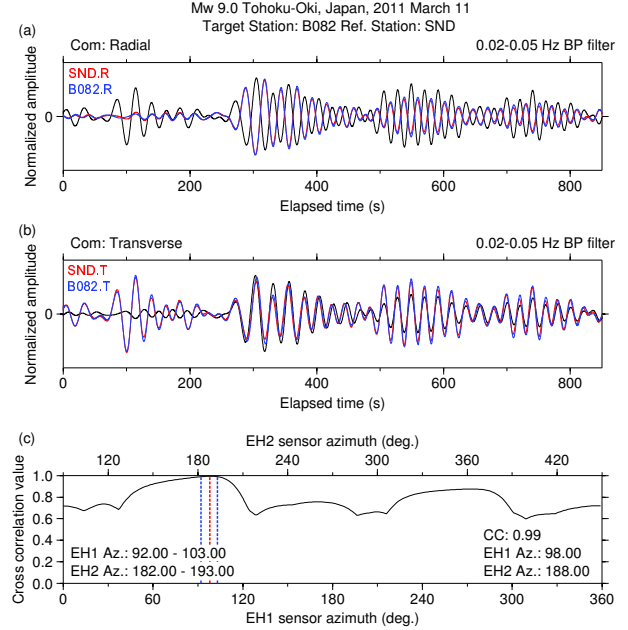


Figure 2.27: B082 sensor orientation estimate using the cross-correlation method. Observed waveforms (20-50 sec) in (a) the radial and (b) the transverse components from station SND (red) and B082 (blue) for the 2011 M_w 9.0 Tohoku-Oki Japan earthquake. Also shown are the rotated waveforms for station B082 (black) with assigned sensor azimuths EH1=0 degree and EH2=90 degrees. (c) Cross-correlation values between station SND and B082 as a function of sensor azimuth/orientation. The relative orientation of two horizontal components from station B082 is fixed to be constant (90 degrees or -90 degrees). We determine that the sensor orientations of station B082 EH1 and EH2 horizontal channels are 98 degrees and 188 degrees, respectively (dashed red line), with the cross-correlation value of 0.99. The high cross-correlation values obtained indicate that our measurement of the PBO sensor orientations is robust. The 95 percent confidence interval (dashed blue lines) for the sensor orientation estimate is 92-103 degrees for the EH1 channel (182-193 degrees for the EH2 channel).

14 Spatiotemporal Behaviors in Earthquake Multiplets at the Geysers Geothermal Field, CA

Taka'aki Taira

14.1 Introduction

The Geysers geothermal field is located in northern California and is characterized by a high rate of microseismicity. The Geysers seismicity is spatially and temporally correlated with geothermal production and injection well activity. The Geysers area is thought to be subject to a regional tectonic stress field associated with the strike-slip relative motion between the North American and Pacific plates (Oppenheimer, 1986). Many naturally occurring fractures may be stressed to near failure, and thus a small perturbation in the stress field could lead to failure (Majer and Peterson, 2007).

One of the important signatures of the Geysers microseismicity involves earthquake multiplets, or families of earthquakes with similar waveforms. Spatiotemporal variations in the state of stress or migration of geothermal fluids near the multiplet source area are reflected by changes in multiplet occurrence in time and space (Thelen et al., 2011). We identify Geysers multiplets and investigate their spatiotemporal behaviors.

14.2 Multiplet Catalog in the Geysers Geothermal Area

We construct a multiplet catalog using broadband seismic data recorded at station GDXB. This station is located near the center of the Geysers geothermal area (Figure 2.28) and has been operational since the middle of 2006. The background noise level above 1 Hz at station GDXB appears to be lowest, compared with those at other seismic stations in the Geysers area. We focus on the data from station GDXB and analyze over 65,000 Geysers local earthquakes (May 2006 through Dec. 2011) detected by the Northern California Seismic System earthquake catalog.

A 8-24 Hz bandpass filter and a 5.12-s time window from the direct P-wave are used to identify multiplets. This time window typically includes the direct S-wave arrivals. We measure cross-correlation values for 400 million seismogram pairs and use 0.95 for the waveform cross-correlation threshold for identifying multiplets (Figure 2.29). This threshold minimizes the possibility of falsely detecting two events as an earthquake multiplet. We find around 650 earthquake multiplets. The majority of them are earthquake doublets. We calculate the recurrence intervals and differences in seismic magnitudes for earthquake multiplets (Figure 2.30).

It appears the distribution of the recurrence intervals obtained has a peak at 30-50 days, although doublets

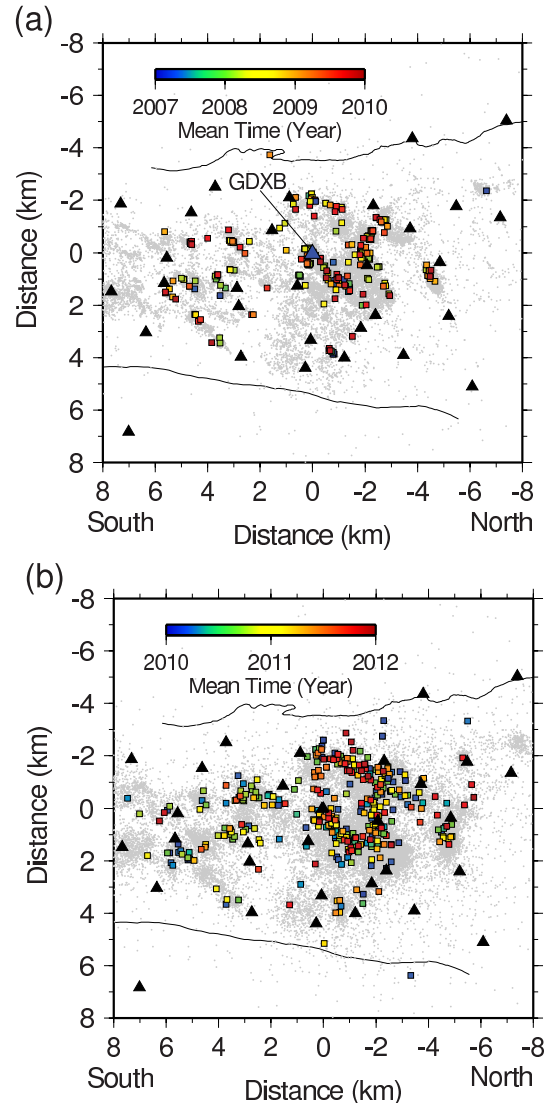


Figure 2.28: Geysers multiplets (squares) during (a) 2007-2009 and (b) 2010-2012, identified by our analysis. Triangles are seismic stations. Gray dots are the background seismicity determined by NCEDC.

or multiplets would be less likely to occur within a few minutes of each other than within a month of each other (Figure 2.30a). The magnitude difference is close to zero, indicating that the multiplet events have event sizes comparable to each other (Figure 2.30b). This result suggests that multiplets or doublets are not mainshock-aftershock sequences. The shorter recurrence interval with simi-

lar event size for Geysers multiplets is consistent with those for multiplets observed during eruptions at volcanoes (e.g., *Thelen et al.*, 2011) in which magma or geothermal fluid migration would lead to the occurrence of multiplets, rather than stress perturbations. We infer that the occurrence of Geysers multiplets is primarily governed by hydrothermal fluid migration. The catalog of Geysers multiplets appears to indicate increased multiplet activity after 2010 (Figure 2.28). In the future, we will examine spatial and temporal correlations between the multiplet seismicity and geothermal production and injection well activity.

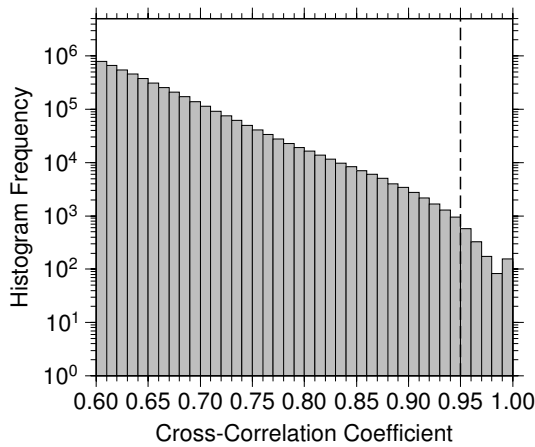


Figure 2.29: Histogram of cross-correlation values (> 0.6) for the Geysers local earthquakes analyzed.

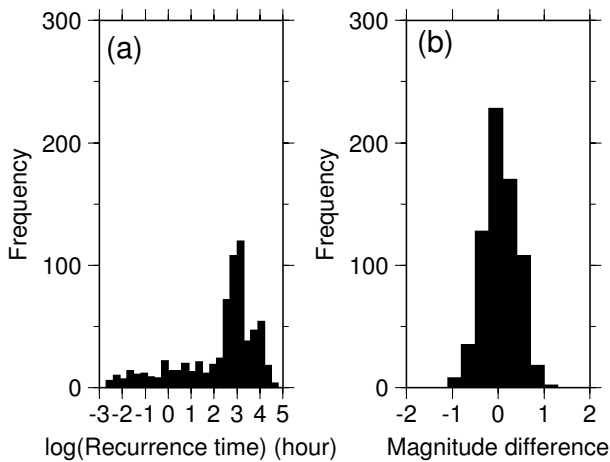


Figure 2.30: Distributions of (a) recurrence intervals and (b) magnitude differences for the Geysers multiplets

14.3 Acknowledgements

We thank F. Massin for discussion, NCEDC and LBNL for data collection and distribution. This work is supported by the National Science Foundation EAR-1053211.

14.4 References

Majer, E., J. E. Peterson, The impact of injection on seismicity at The Geysers California Geothermal Field, *International Journal of Rock Mechanics and Mining Sciences*, 44, 1079-1090, 2007.

Oppenheimer, D.H., Extensional tectonics at the Geysers geothermal area, California, *J. Geophys. Res.*, 91(B11), 11,463-11,476, doi:10.1029/JB091iB11p11463, 1986.

Thelen, W., S. Malone, M. West, Multiplets: Their behavior and utility at dacitic and andesitic volcanic centers, *J. Geophys. Res.*, 116, B08210, 16pp., DOI:10.1029/2010JB007924, 2011. .

15 A systematic analysis of seismic moment tensor for seismicity at The Geysers Geothermal Field, California

Sierra Boyd, Douglas Dreger, Peggy Hellweg, Taka'aki Taira, Jennifer Taggart, Tom Weldon, and Peter Lombard

15.1 Introduction

Forty $M > 3$ earthquakes located at The Geysers Geothermal Field were selected from the UC Berkeley Moment Tensor Catalog for in depth analysis of seismic moment tensor solutions, uncertainties, and well resolved source-type. Deviatoric and full moment tensor solutions were computed, and statistical tests were employed to assess solution stability, resolution, and significance. The general moment tensor can be decomposed in a multitude of ways, and in this study we examine the pure isotropic (explosion/implosion ISO), double-couple (DC), volume Compensated Linear Vector Dipole (CLVD) sources, as well as compound sources such as DC+CLVD, DC+ISO, and tensile-crack+DC source models. The solutions are cataloged. A single event that occurred on October 12, 1996 at the southern edge of the field was found to have a statistically significant isotropic component.

15.2 Methodology

We invert three-component, complete waveform data for deviatoric and full, six-element moment tensors using the method outlined in *Minson and Dreger, 2008*. The broadband velocity data is instrument corrected with reported pole-zero response functions, integrated to displacement and bandpass filtered with an acausal, 4-pole, Butterworth bandpass filter with a 0.02 to 0.05 Hz or 0.02 to 0.10 Hz passband. In addition to finding best fitting solutions we apply the F-test to determine the significance of models with higher degrees of freedom, Jackknife tests to assess the stability of solutions due to station configuration, bootstrap residuals to characterize random, aleatoric uncertainties in the solutions, and utilize the Network Sensitivity Solution (NSS; *Ford et al., 2010*) to map the full moment tensor solution for the complete source-type solution space as proposed by *Hudson et al., 1989*. All of these tests require significant computational effort and therefore a staged approach is taken in which if a solution is largely double-couple no additional analysis is performed. If a solution has large deviatoric non-double-couple components (e.g. CLVD), or if a full moment tensor has large non-double-couple terms, an F-test is first performed to assess significance. If that test indicates that there is a large improvement in fit with the non-double-couple terms then the additional Jackknife, bootstrap and NSS analyses are performed.

We found that depth sensitivity using data filtered between 0.02 to 0.05 Hz is fairly limited, so we therefore

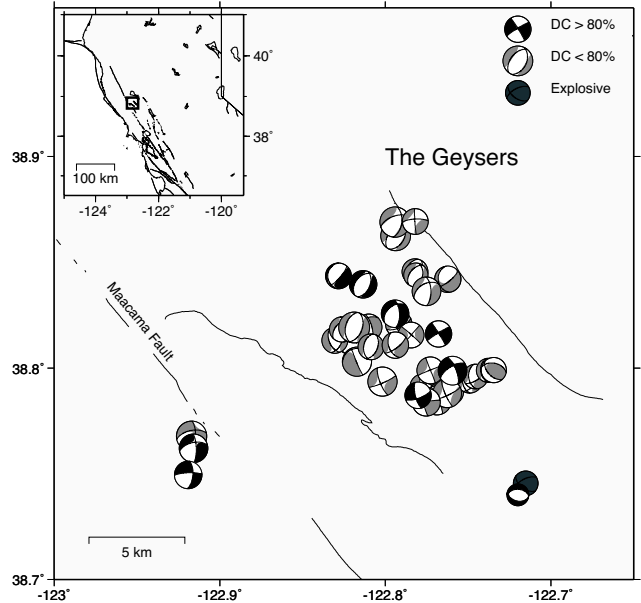


Figure 2.31: Map showing moment tensor solutions of the 40 studied events.

restrain our analysis to event depths determined from the NCSS and LBNL catalogs. In the future, with better-calibrated velocity models and/or using the local Calpine seismic data we may be able to improve on moment tensor based source depth determination. However, for now we assume that the depths reported in the catalog are well determined and focus on the recovery of the seismic moment tensor source parameters.

15.3 Results

In Figure 2.31 moment tensor solutions are shown for the studied events. The black solutions are for events that have solutions with DC components larger than 80% of the total seismic moment, whereas the gray solutions show the cases with large non-double-couple components (DC < 80%). On the whole the solutions show a trend in which the T-axis is oriented E-ESE; however, solutions vary from relatively rare strike-slip cases to more common normal faulting events, and CLVD solutions that accommodate both DC types. The CLVD solutions have a roughly horizontal, E-ESE trending major vector dipole in tension. There is one solution for an event on October 12, 1996 in the southern region of the field that has a large isotropic moment tensor solution. The DC event

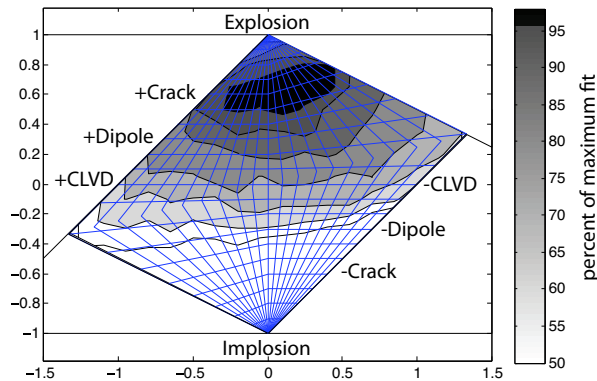


Figure 2.32: Network sensitivity solution for the October 12, 1996 event.

located nearby shows an unusual east-west striking normal solution. The deviatoric solution for the October 12, 1996 has the same orientation.

The F-test is used to compare the ratio of the goodness of fit of the full and deviatoric moment tensor solutions. Most events do not rise above a level of statistical significance of 50%; however, the October 12, 1996 event (large circle) does show a statistical significance of 99% for a solution using 10 three-component stations. The Jackknife test is performed by inverting all combinations of 9 and 8 stations from the full 10 station set. The results of the Jackknife test reveal a stable solution that is substantially non-double-couple with a large tensile isotropic component. These tests show that no single station, or particular azimuth is biasing results toward a non-double-couple solution.

The network sensitivity solution (NSS; Ford *et al.*, 2010) is a method to map maximum fit surface in a source-type representation. This method searches in a brute force manner an order of 10 million uniformly distributed moment tensor solutions. This technique was developed to examine the uniqueness and possible trade-offs in solutions due to sparse network configurations and to changes in available station coverage. Here it can be used in a comparative sense to illustrate differences and overlap of solutions using different data sets. For the October 12, 1996 event we show the maximum fit surface considering 20 million uniformly distributed moment tensors, shown in Figure 2.32. The darker gray fields are showing 90, 95, 98% of the best fit solution. The double-couples and deviatoric solutions fit at best only 80% of the best fit solution.

15.4 Conclusions

We investigate source models for stability and significance of forty events at The Geysers Geothermal Field. Of these events 9 are found to be dominantly double-

couple, 30 are found to deviate significantly from a double-couple solution, and 1 is found to have a statistically significant isotropic component. We use the NSS to determine confidence regions of possible source types of events at The Geysers Geothermal Field. The results of the NSS for the October 12, 1996 event shown in Figure 2 suggest a solution that is a combination of double-couple and volumetric expansion. Our previous results identified the full moment tensor solution as having a statistically significant volumetric component based on the F-test.

15.5 Acknowledgements

This work was supported by the Assistant Secretary for Energy Efficiency and Renewable Energy, Office of Geothermal Technologies, of the U. S. Department of Energy under Contract No. DE-EE0002756.

15.6 References

- Ford, S.R., W.R. Walter and D.S. Dreger, Event discrimination using regional moment tensors with teleseismic-P constraints, *Bull. Seism. Soc. Am.*, 108, 883-884, 2012.
- Ford, S.R., D.S. Dreger, and W.R. Walter, Network sensitivity solutions for regional moment tensor inversions, *Bull. Seism. Soc. Am.*, 100, 1962-1970, 2010.
- Hudson, J.A., R.G. Pearce, and R.M. Rogers, Source type plot for inversion of the moment tensor, *J. Geophys. Res.*, 9(B1), 765-774, 1989.
- Minson, S. and D. Dreger, Stable inversion for complete moment tensors, *Geophys. Journ. Int.*, 174, 585-592, 2008.

16 Joint Inversion of Seismic and Geodetic Data for the Source of the 4th March 2010 M_w 6.3 Jia-Shian, SW Taiwan, Earthquake

Mong-Han Huang, Douglas Dreger, Roland Bürgmann, and Seung-Hoon Yoo

16.1 Introduction

The March 2010 Jia-Shian (M_w 6.3) earthquake occurred in southwestern Taiwan and caused moderate damage (Figure 2.33a). No surface rupture was observed, reflecting a deep source that is relatively rare in west Taiwan. We develop finite-source models using a combination of seismic waveform data (strong motion and broadband stations), GPS, and InSAR to understand the rupture process and slip distribution of this event. The main shock is mainly a reverse event with a small left-lateral component. The rupture's centroid source depth is 19 km based on a series of moment tensor solution tests with improved 1D Greens functions. The primary slip asperity of the preferred model is about 20 km in diameter and ranges in depth from 22 to 13 km. The peak slip is 42.51 cm, and the total scalar seismic moment is 3.25×10^{18} N m. Both the main shock and aftershocks are located at the transition zone where the depth of the regional basal decollement deepens from central to south Taiwan. In addition, the P and T axes of this event are rotated about 40 degrees counterclockwise from the direction of the current plate collision. Hence, the deviation of the compressional stress exhibited by this event may be a regional perturbation of a pre-existing geologic structure.

16.2 Inversion and Result

We use a linear least squares inversion code based on *Kaverina et al.* (2002), in which the finite source is discretized with a finite distribution of point sources in both space and time. A damped, linear least squares inversion with a positivity constraint (allowing only for thrust dip-slip component) is used to determine the distribution of slip in space and time. A single time window is used with a fixed dislocation rise time (0.5 s) propagating away from the source with constant rupture velocity (4.2 km/s). Spatial smoothing with linear equations minimizing differences in slip between subfaults is applied to stabilize the seismic and geodetic inversion. Different weighting and smoothing parameters are applied to the simultaneous inversion using the method proposed by *Kaverina et al.* (2002). The Green's functions for southern Taiwan are taken from *Chi and Dreger* (2004). For the geodetic inversion, the geodetic Greens functions are computed by assuming the same layered elastic structure as for the seismic inversion. A 50×50 km NW dipping fault geometry with 625 subfaults was considered for the inversions. The coseismic slip distribution is estimated

both from the inversion of each data set separately and jointly.

Seven strong motion and three broadband seismic stations are used for the seismic inversion, and 108 GPS stations and 3 ALOS PALSAR interferograms are used for the geodetic inversion. The joint inversion shows coseismic slip covering a 15×20 km area northwest of the hypocenter (Figure 2.33c) with an average slip of 15 cm and a peak slip of 42.5 cm.

16.3 Discussion and Conclusion

The orientation of the P and T axes of the main shock and aftershocks is different from the direction of the current plate collision (Figure 2.33d,e). However, the crustal scale (0-30 km) strain rate based on the SW Taiwan regional seismicity and focal mechanism inversions (*Mouthereau et al.*, 2009) shows ENE-WSW compression near the Jia-Shian epicenter. This ENE-WSW compression has the same orientations as the P axes of the main shock and most of the aftershocks, which agree with the ambient strain distribution at the source depth. To conclude, the Jia-Shian event occurred along the boundary between the Western Foothills and the Central Range. The current surface strain rate is not consistent with the stress orientations in the upper crust of the Jia-Shian event. Combining all of the observations suggests that this event may be due to the reactivation of a pre-existing geological structure that is not necessarily participating in the current plate collision. Details of the kinematics or the geometry of the structure will be needed to confirm this.

16.4 Acknowledgements

We thank the Institute of Earth Science, Academia Sinica, Taiwan for providing seismic and geodetic data. We thank H.-H. Huang of National Taiwan University for providing the aftershock catalog.

16.5 References

- Kaverina, A., Dreger, D., and Price, E., The combined inversion of seismic and geodetic data for the source process of the 16 October 1999 M_w 7.1 Hector Mine, California earthquake, *Bull. Seismol. Soc. Am.*, 92, 1266-1280, 2002.
- Mouthereau, F., C., Fillon, and K.-F. Ma, Distribution of strain rates in the Taiwan orogenic wedge, *Earth Planet. Sci. Lett.*, 284, 361-385, 2009.
- Saikia, C. K., Modified frequency-wave-number algorithm for regional seismograms using Filons quadrature-modeling of L(g) waves in eastern North America, *Geophys. J. Int.*, 118, 142-158, 1994.

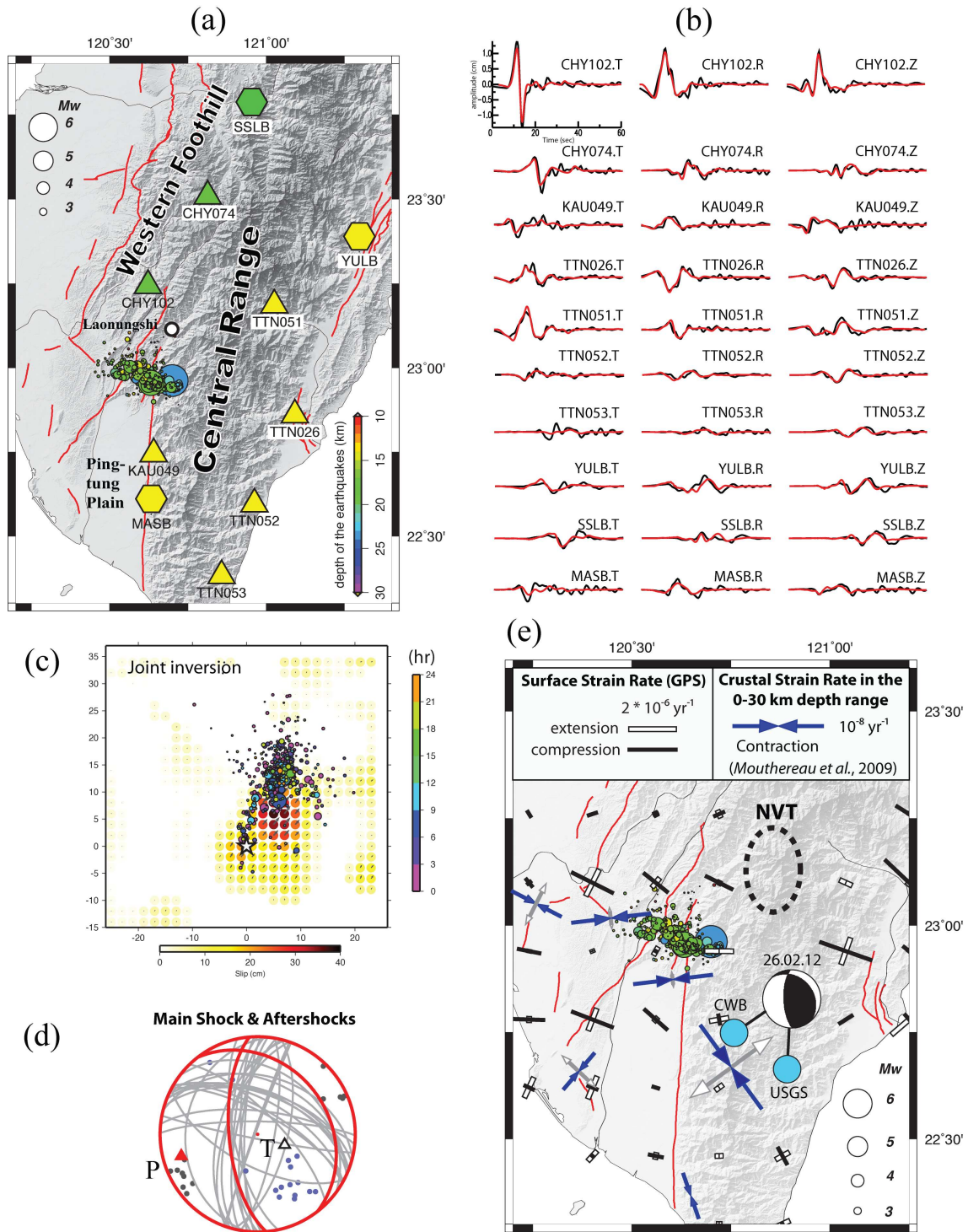


Figure 2.33: (a) Selected strong motion stations (triangles) and broadband stations (hexagons). The green and yellow stations belong to the west and east Taiwan velocity models, respectively. The Jia-Shian main shock and aftershocks are color coded by depth. (b) The comparison of synthetic (red) and seismic data (black) from the joint inversion. (c) Joint inversion result (variance reduction of seismic data: 74.8%; GPS: 64.9%; InSAR: 77.0%). Black arrows represent the slip direction and amplitude for each subfault. The colored circles are aftershocks since the main shock in hours. (d) P and T axes of the main shock (red and white triangles) and aftershocks (grey and dark blue circles). (e) The surface strain rate (black and white bars) and crustal scale (0-30 km) strain rate (dark blue arrows). The beach ball diagram shows the most recent earthquake in this region with a focal mechanism similar to the Jia-Shian event, which may imply an extension of this structure to the southeast. NVT indicates the region of triggered non-volcanic tremors in the Central Range.

17 Deciphering the Mystery of the Great Indian Ocean Earthquakes

Kelly Wiseman and Roland Bürgmann

17.1 Introduction

On April 11, 2012, there were two magnitude 8+ earthquakes off the west coast of northern Sumatra, Indonesia. The first was a magnitude 8.6 and the second was a magnitude 8.2, two hours later. Both of these earthquakes were a result of strike-slip faulting within the oceanic lithosphere of the broadly distributed India-Australia plate boundary zone. Unlike the nearby 2004 magnitude 9.2 Sumatra megathrust earthquake that produced a disastrous tsunami, these earthquakes involved mostly horizontal motion and initiated more than 380 km from the Sumatra mainland, thereby limiting the shaking and tsunami damage. Although these earthquakes quickly faded from the news once the tsunami warnings were canceled, the magnitude 8.6 mainshock is incredibly significant as it holds the distinction of being both the largest instrumentally recorded strike-slip earthquake and the largest earthquake within the interior of a tectonic plate. Early geophysical studies have revealed another noteworthy aspect of these events, that the mainshock involved sequential ruptures of multiple fault planes oriented nearly perpendicular to each other. Here we discuss the unusual geological conditions within the Indian Ocean basin that allow for such a large, complex intraplate earthquake and relate the timing of these events to the 2004 megathrust earthquake.

17.2 Relation to the 2004 Sumatra-Andaman earthquake

The 2004 Sumatra megathrust earthquake fundamentally changed the stress state in the surrounding lithosphere and seismicity rates have been enhanced throughout Southeast Asia in the years following the great earthquake. The yellow and blue beach balls in Figure 2.34b,c (www.globalcmt.org) depict the focal mechanisms for all of the strike-slip earthquakes in the incoming Indian and Australian plates, west of the Sunda trench, during the years between the 2004 and 2012 earthquakes. The mechanisms are very similar to the focal mechanisms for the two April, 2012 earthquakes (shown in red), and are consistent with either left-lateral strike-slip motion on the N-S oriented fractures, or right-lateral motion on E-W oriented planes.

The 2012 mainshock initiated at 20 km depth and the aftershock pattern (gray dots in Figure 2.34a, USGS NEIC catalog), along with preliminary back-projection rupture propagation models (Meng *et al.*, 2012), suggests complex rupture on multiple fault planes. It appears that the mainshock started with bilateral shear away from the

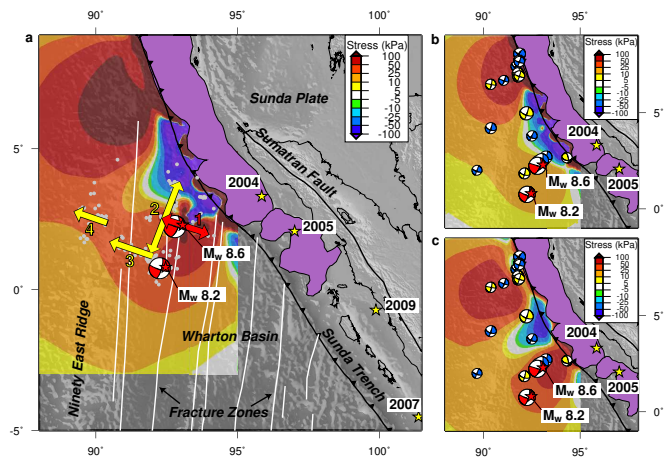


Figure 2.34: Recent stress changes in the Indian Ocean. (a) Total stresses induced by the 2004 and 2005 megathrust earthquakes (purple regions) plus the 2012 foreshock resolved at the hypocentral depth of the magnitude 8.6 earthquake into the orientation of the initial E-W fault plane. The red-and-white beach balls depict the focal mechanisms for the two 2012 magnitude 8+ earthquakes. The epicenters for the first 12 days of the 2012 aftershock sequence are marked with gray dots (USGS NEIC catalog). The fault planes are based on Meng *et al.* (2012) and the fracture zones are from Singh *et al.* (2011). (b) Coseismic stresses induced by the 2004 and 2005 earthquakes. The yellow focal mechanisms highlight the strike-slip earthquakes during the first two months following the 2004 earthquake and the blue focal mechanisms depict earthquakes after the first two months and before the 2012 mainshock. (c) Postseismic stresses induced by the 2004 and 2005 earthquakes.

hypocenter on an E-W oriented plane (red fault segment in Figure 2.34a) and then bilaterally ruptured a N-S oriented plane to the west of the hypocenter (yellow segment labeled 2). It ended with slip on two additional E-W oriented segments to the south, near the eventual magnitude 8.2 aftershock (yellow segments labeled 3 and 4) (Delescluse *et al.*, 2007). The 2012 mainshock was able to grow to such a large magnitude because it was able to continue rupturing beyond the initial E-W fault plane, on multiple nearby faults in the weak, heavily fractured northern Wharton Basin. This complex rupture scenario is similar to the second largest Wharton Basin earthquake, a magnitude 7.9 earthquake in June 2000, that started as left-lateral strike-slip motion on a

N-S plane and ended as oblique motion on an E-W plane (Abercrombie *et al.*, 2003). Half of the focal mechanisms for the 2012 aftershocks show oblique motion, indicating that the magnitude 8.6 earthquake may have included an oblique sub-event as well.

We have calculated the stresses induced by the 2004 (Chlieh *et al.*, 2007) and 2005 (Konca *et al.*, 2007) megathrust earthquakes at the hypocenter of the magnitude 8.6 earthquake in order to determine if the 2012 earthquakes were triggered events. We modeled the static, coseismic stress perturbations from the two nearby megathrust ruptures and the time-dependent perturbations resulting from postseismic relaxation of the upper mantle following the megathrust events. The 2004 earthquake contributed most of the stress changes at the 2012 hypocenter and further to the north spanning the zone of enhanced strike-slip activity. The rate of strike-slip activity in the northern Wharton Basin increased greatly in the initial months following the 2004 earthquake (yellow beach balls in Figure 2.34b,c), and continued at a lower level up until the 2012 earthquakes. The combined coseismic stress perturbation from the 2004 and 2005 earthquakes was ~ 18 kPa at the hypocenter (Figure 2.34b), with similar values when resolving stress on either the E-W or N-S fault plane orientation. The additional stress perturbations from postseismic deformation can explain the continued strike-slip activity during the years following the 2004 earthquake (blue beach balls in Figure 2.34b,c). By April 2012, the postseismic stress perturbation from the megathrust earthquakes was ~ 4 times larger than the induced coseismic stresses at the 2012 hypocenter, highlighting the importance of postseismic deformation for triggering earthquakes away from the coseismic rupture plane. (Figure 2.34c). A magnitude 7.2 foreshock, ~ 25 km NE of the mainshock in January 2012, involved right-lateral slip on an E-W oriented fault and added a final push before the April events.

17.3 Discussion

The high strain-rates within the Wharton Basin enable strike-slip earthquakes over a wide portion of the plate interior, and the stresses imparted to the oceanic lithosphere by the 2004 earthquake induced a spike in these strike-slip earthquakes. This behavior is particular to the Equatorial region of the Indian Ocean basin, as we did not see triggered strike-slip earthquakes in the Pacific plate following the 2011 Tohoku earthquake. The 2012 magnitude 8+ events were the latest in this collection of post-2004 strike-slip earthquakes and the additional stress imparted to the lithosphere from the postseismic deformation can explain the time delay between the 2004 and 2012 earthquakes. The 2012 mainshock was so large because it was able to rupture multiple weak spots within the oceanic lithosphere, including four separate fault planes. The annual moment rate for

the entire Wharton Basin, that actively deforms down to 20°S , is $\sim 3.5 \times 10^{19}$ Nm/yr (Delescluse and Chamot-Rooke, 2007), and these two magnitude 8+ strike-slip earthquakes released ~ 270 years of accumulated seismic moment. The northern portion of Wharton Basin is the highest straining region in the diffuse India-Australia boundary zone, accommodating roughly 1 cm/yr of N-S left-lateral shear (Delescluse and Chamot-Rooke, 2007), so this region should have shorter earthquake repeat times, on the order of 500-1000 years, than the rest of the region. Over the past millennia, the megathrust earthquake periodicity for the southern end of the 2004 rupture has been roughly 400-600 years (Meltzner *et al.*, 2010), therefore these great oceanic strike-slip earthquakes may coincide with the great Sunda megathrust earthquakes every 1-2 cycles. Although these 2012 earthquakes did not cause much damage or casualties, they highlight the risk that very large earthquakes can occur within the interior of a plate, and that unexpected events can be triggered well after great megathrust earthquakes.

17.4 Acknowledgments

This work is supported by the National Science Foundation grant EAR 0738299.

17.5 References

- Abercrombie *et al.*, The June 2000 M_w 7.9 earthquakes south of Sumatra: Deformation in the India-Australia Plate, *J. Geophys. Res.*, 108, B1,2018, 2003.
- Chlieh *et al.*, Coseismic slip and afterslip of the great M_w 9.15 Sumatra-Andaman earthquake of 2004, *Bull. Seismol. Soc. Am.*, 97, S152-S173, 2007.
- Delescluse and Chamot-Rooke, Instantaneous deformation and kinematics of the India-Australia Plate, *Geophys. J. Int.*, 168, 818-842, 2007.
- Konca *et al.*, Rupture kinematics of the 2005 M_w 8.6 Nias-Simeulue earthquake from the joint inversion of seismic and geodetic data, *Bull. Seismol. Soc. Am.*, 97, S307-S322, 2007.
- Meng *et al.*, Back-projection results 4/11/2012 (M_w 8.6), offshore Sumatra, Indonesia, http://tectonics.caltech.edu/slip-history/2012_Sumatra/back_projection, 2012.
- Meltzner *et al.*, Coral evidence for earthquake recurrence and an A.D. 1390-1455 cluster at the south end of the 2004 Aceh-Andaman rupture, *J. Geophys. Res.*, 115, B10402, 2010.
- Singh *et al.*, Extremely thin crust in the Indian Ocean possibly resulting from Plume-Ridge Interaction, *Geophys. J. Int.*, 184, 29-42, 2011.

18 Source Spectral Variation and Yield Estimation Derived from High Frequency P and S Coda

Seung-Hoon Yoo, Kevin Mayeda, and Douglas Dreger

18.1 Introduction

Identifying Underground Nuclear Explosions (UNEs) and discriminating them from natural earthquakes is a critical issue for the verification of the Comprehensive nuclear-Test-Ban Treaty (CTBT). The earthquake source is described as a shear dislocation on a fault plane, which generates both P- and S-wave at the source. On the other hand, the nuclear explosion source is described as an isotropic volumetric expansion, which theoretically generates only P-waves without S-waves. However, significant S-wave generation is commonly observed from explosion sources and the mechanism remains controversial. A number of explanations (e.g., phase interaction and conversion at the free-surface or any other near source boundary, Rg generation by a compensated linear vector dipole source (CLVD), scattering due to topography, spallation, rock damage, etc) were proposed but a unifying model does not present. To enhance the identification and discrimination capability of explosions, a more comprehensive understanding of explosion sources including primary and secondary process are essential.

We analyze seismic coda waves from the near-source explosions to better understand the generation and properties of the scattered P and S wavefields. The well-instrumented experiments provide us with excellent data from which to document the characteristic spectral shape (e.g., tamped single-fired with variety explosives, ripple-fired), relative partitioning between P and S-waves.

18.2 Data and Method

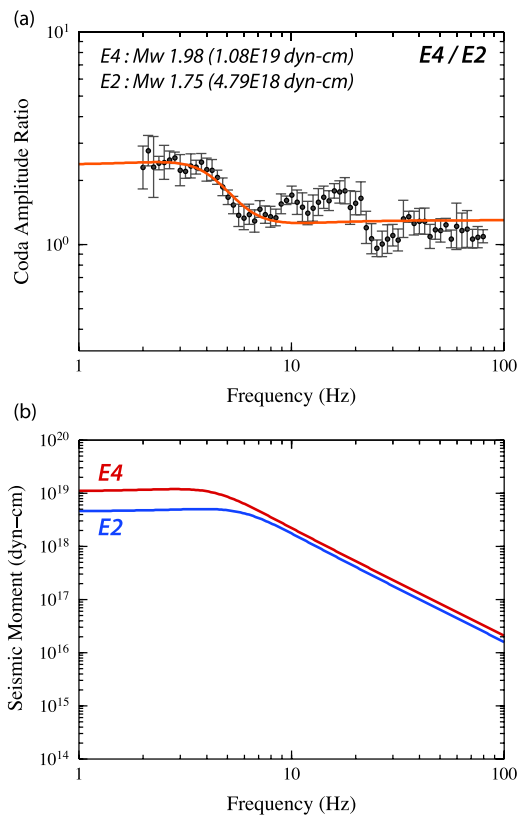
We report on two near-source explosion data sets. In the first case, we examine tamped single-fired explosions, which are conducted in Barre granite during the 2008 New England Damage Experiment (NEDE) (*Leidig et al., 2009*). The experiment included the detonation of five small (135 to 270 lbs) chemical explosions in relatively unfractured, homogeneous Barre granite in Vermont. To examine a hypothesis that different damage would lead to possible variations in S-wave generation, the explosions (black powder, ANFO, Composition B) were designed with variable velocities of detonations (VOD) ranging from 0.5 to 8 km/sec. In the second case, we analyze five explosions (a delay-fired production blast and four single-fired shots) using ANFO explosive at a Massachusetts quarry. For the production shot, the total explosives used was 20,377 lbs with the typical delay between the holes in each row being 16 msec and the delays between rows being 106 msec. The four single-fired shots were detonated with different amount of explosive ranging from 132 to 788 lbs.

The five shots in each experiment are closely located within several tens of meters. We assume that all shots in each experiment share common path effects and apply the coda ratio method (*Mayeda et al., 2007*). We measure coda amplitudes for 3-components and narrow frequency bands (1/2 octave bandwidth with 1/8 octave overlapping) with central frequencies ranging between 2 to 80 Hz (NEDE) and 42 Hz (a Massachusetts quarry experiment). We form the average spectral ratios ratio between the high and low yield explosions over stations and components. A total of 19 short-period stations (2.8-30 km) were averaged for NEDE and 7 broadband stations (1.3-4.5 km) and 10 short-period stations (0.5-5.3 km) were averaged for a Massachusetts quarry experiment (Figure 2.35A). Then, we perform a grid-search using the MM71 explosion source model (*Mueller and Murphy, 1971*) to get the theoretical source spectra. We also perform time-domain full moment tensor inversion for selected high yield explosions (Figure 2.35B). Independent seismic moment estimates are needed to convert the dimensionless coda amplitudes to an absolute physical unit. This is also very important to get a stable estimate of source spectrum by constraining the long period coda ratio in the source model search. Using the derived theoretical source spectra and independent seismic moment, we calibrate all measured coda amplitudes to source spectra for the other explosions (Figure 2.35C).

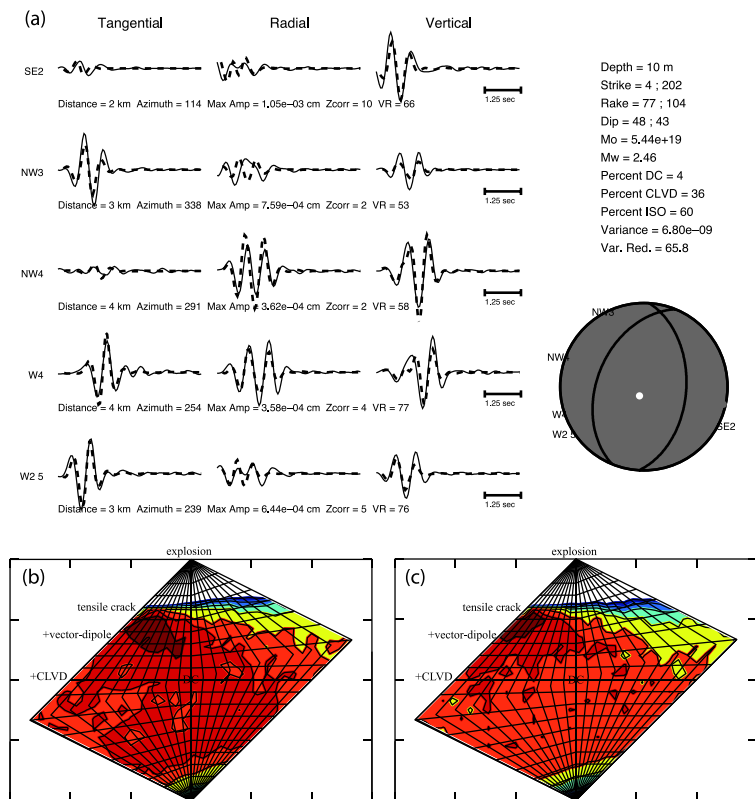
18.3 Preliminary Results

From NEDE source spectra, we found the source spectrum for the black powder shot (slow burning explosive) falls off rapidly at high frequency compared to the source spectra of ANFO and Composition B. However, the black powder shot produced spectral amplitudes comparable to that of the ANFO shot below 5 Hz. Composition B (fast burning explosive) explosions effectively radiate more high frequency energy, however it is deficient in low frequency S-wave energy. The Composition B shot produced significantly smaller spectral amplitudes than the black powder shot below 5 Hz. We also found that there is a factor of ~ 2 difference in seismic moment for similar yield shots between the NEDE and a Massachusetts quarry data due to the venting effect. In the source spectrum of the ripple-fired shot, we clearly see the modulation peaks at theoretical modulation frequencies based on the delay times.

A. Coda Spectral Ratio



B. Full Moment Tensor Analysis



C. Coda-derived Source Spectra

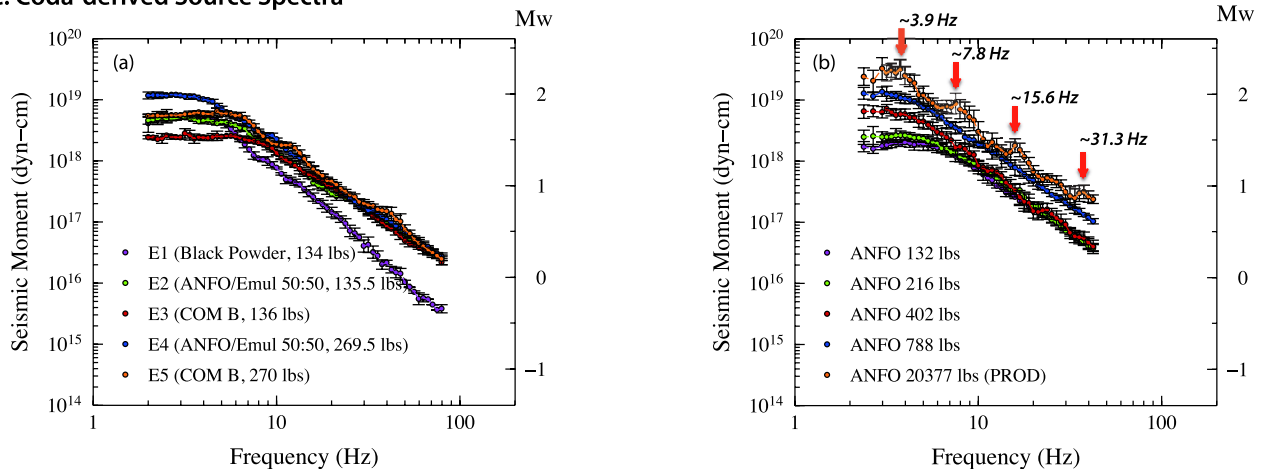


Figure 2.35: A: Averaged coda spectral ratio between the E4 and E2 shots in NEDE experiment (a) and the corresponding theoretical source spectra (b). B: Full moment tensor inversion result (a) and network sensitivity analysis using 3 stations (b) and 5 stations (c) for the production shot in a Massachusetts quarry experiment. C: Coda-derived source spectra for the NEDE shots (a) and a Massachusetts quarry shots (b).

18.4 Acknowledgements

This work was supported by Weston Geophysical Corp.

18.5 References

Leidig, M., R. Martin, P. Boyd, J. Bonner, and A. Stroujkova, Quantification of rock damage from small explosions and its effect on shear-wave generation: phase I homogenous crystalline rock, in *Proceedings of the 2009 Monitoring Research Review: Ground-Based Nuclear Explosion Monitoring Technologies*, 1, 492-501, 2009.

Mayeda, K., L. Malagnini, and W.R. Walter, A new spectral ratio method using narrow band coda envelopes: Evidence for non-self-similarity in the Hector Mine sequence, *Geophys. Res. Lett.*, 34, L11303, doi:10.1029/2007/GL030041, 2007.

Mueller, C.S., and J.R. Murphy, Seismic characteristics of underground nuclear detonations, Part I: seismic spectrum scaling, *Bull. Seism. Soc. Am.*, 61, 1675-1692, 1971.

19 Regional Moment Tensor Inversion for Shallow Sources: the Effects of Free-Surface Vanishing Traction

Andrea Chiang and Douglas S. Dreger

19.1 Introduction

For the nuclear explosion source-type identification problem the uncertainty in a solution is as important as the best fitting parameters (*Ford et al.*, 2009), and there are concerns about bias that can be introduced through velocity structure and corresponding Green’s functions, as well as due to the shallow depth of burial. A potential issue for shallow seismic sources that are effectively at the free-surface between the ground and air is that the vanishing traction at the free-surface can cause the associated vertical dip-slip (DS) Green’s functions to have vanishing amplitudes (*Julian et al.*, 1998), which in turn results in the indeterminacy of the M_{xz} and M_{yz} components of the moment tensor and bias in the moment tensor solution. The effects of the free-surface on the stability of the moment tensor method become important as we continue to investigate and improve the capabilities of regional full moment tensor inversion for source-type identification and discrimination. It is important to understand the effects for discriminating shallow explosive sources in nuclear monitoring, but free-surface effects could also be important in natural systems that have shallow seismicity such as volcanoes and geothermal systems.

19.2 Methods

In this study, we generated a suite of velocity models by introducing a shallow velocity gradient to the 1D reference model (*Song et al.*, 1996). This is accomplished by splitting the top 2.5-km thick layer in the reference model into two separate layers. We systematically adjusted the thickness and velocity of the two new layers (Figure 2.36a), but constrained the variations of the two parameters by maintaining the same vertical travel time as the reference model. The purpose of the study was to generate different but comparable velocity models.

For each 1D model, we generated Green’s functions at regional distances (100 to 400 km) with source depths ranging from 0.2 to 3.5 km. Using the same set of Green’s functions, we generated two types of synthetic data with different source mechanisms: a pure explosion case and a composite case (double-couple and explosion) with an F-factor of 1 (*Burger et al.*, 1986). Random Gaussian white noise of 20% was added to the synthetic data. Then we used a 10 to 50 seconds causal bandpass butterworth filter to filter the synthetic data and the Green’s functions. We implemented a semi-ideal four-station coverage for the inversion, consisting of source-to-receiver distances

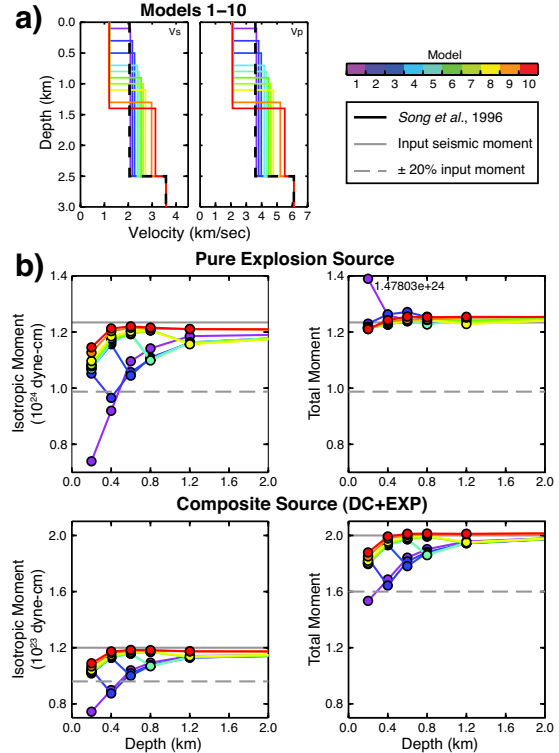


Figure 2.36: (a) Velocity models 1 to 10 of the 59 models tested. (b) Isotropic and total scalar seismic moments for pure explosion and composite source (double-couple and explosion) mechanisms. Results are based on Green’s functions computed using the velocity models in part (a).

distributed at increasing 100 km increments from 100 to 400 km, and in semi-regular azimuths. The linear inversion problem yields six independent components of M_{ij} .

19.3 Velocity Model Dependence

Of the 59 velocity models tested, those with a shallow velocity gradient in the upper 1.5 km have little to no bias in their isotropic and total moment estimates, and all estimates fall within the 20% noise level for both the explosion source and the composite source. Similarly, moment estimates from models with a shallow velocity gradient in the upper 1.5 to 2.0 km are within 20% of the input values at depths greater than 0.4 km. Although the total moment estimates for the composite case exhibit greater deviations from the true input value at source

depths shallower than 0.4 km, the bias in the isotropic moment is less significant (Figure 2.36b).

In most cases the full moment tensor inversion successfully recovers the correct mechanism for both the pure explosion case and the composite case over the targeted depth range (< 1 km) for nuclear explosions (Figure 2.37). Free-surface vanishing traction has little effect on recovering the correct mechanism for models with a shallow velocity gradient. The inversion can still recover the correct mechanism for models without a strong shallow velocity gradient at depths greater than 0.5 km; the bias in source mechanism is significant only at depths shallower than 0.4 km.

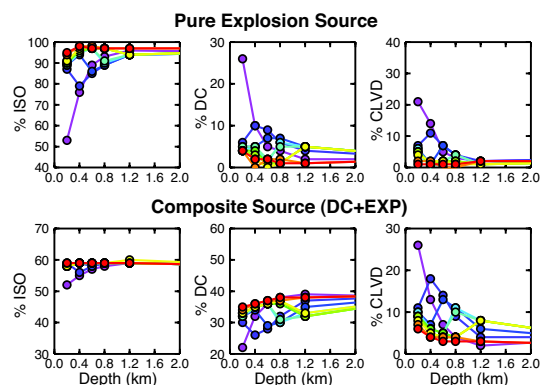


Figure 2.37: Full moment tensor solutions including shear (DC), compensated linear vector dipole (CLVD), and net volume change (ISO), for the different models tested in Figure 2.36a.

19.4 Frequency Dependence

The Littleton quarry blast is an excellent dataset in terms of understanding the effects of free-surface vanishing traction with real data. These chemical explosions are approximately 10 m in depth and are recorded at up to several km distances. Therefore the data represents a rather severe source-station geometry in terms of vanishing traction issues. It is possible to obtain a robust full moment tensor solution that is composed dominantly of an isotropic or explosive component; however the data provide the opportunity to evaluate capabilities of moment tensor inversion as a function of frequency.

Using five broadband stations at distances between 1.3 and 4.4 km from the production shot, we inverted for the best-fit moment tensor solutions and computed the Network Sensitivity Solutions (NSS) for different passbands. Indeed as we move towards longer periods, the moment tensor solution degrades and we obtain the incorrect source mechanism. Although the effects of free-surface vanishing traction may contribute to the degradation of the moment tensor solution as we go towards

longer periods, our preliminary analysis suggests noise in the data and possibly station geometry have a more significant effect on the method’s capabilities in seismic source analysis. A more thorough analysis is needed to assess the different factors that contribute to the errors in the inversion.

19.5 Discussions

Synthetic testing indicates that the DS Green’s functions associated with the M_{xz} and M_{yz} components are affected by the vanishing traction at the free-surface in the period range we are interested, between 10 and 50 seconds period. The amplitudes of the Green’s functions decrease systematically, but the waveforms look similar over the targeted depth range for nuclear explosions with little phase distortion. Our preliminary results show the degree in which free-surface vanishing traction affects the moment tensor solution depends strongly on the velocity model. Velocity models with a shallow velocity gradient show little to no bias in the isotropic and total scalar seismic moment, for both pure explosion source and composite source mechanisms. Similarly, we can retrieve the correct mechanism for these models using the full moment tensor inversion. One possible explanation is that models with a shallow velocity gradient have more complicated waveforms, and thus provide more constraint on the moment tensor inversion. Theoretically, as we go towards longer periods, the effects of vanishing traction would be more severe as the wavelength increases. Initial analysis of the Littleton dataset suggests errors due to noise may be more significant than the effects of vanishing traction. Further analysis is needed to separate out the different sources of error.

19.6 Acknowledgements

We acknowledge funding from the Air Force Research Laboratory, contract FA9453-10-C-0263 that is supporting this research.

19.7 References

- Burger, R.W., T. Lay, T.C. Wallace, and L.J. Burdick, Evidence of tectonic release in long-period S waves from underground nuclear explosions at the Novaya Zemlya test sites, *Bull. Seismol. Soc. Amer.*, *76*, 733-755, 1986.
- Ford, S.R., D.S. Dreger, and W.R. Walter, Identifying isotropic events using a regional moment tensor inversion, *J. Geophys. Res.*, *14*, B01306, 2009. doi:10.1029/2008jb005743.
- Ford, S.R., D.S. Dreger, and W.R. Walter, Network Sensitivity Solutions for Regional Moment-Tensor Inversions, *Bull. Seismol. Soc. Amer.*, *100*, 1962-1970, 2010.
- Julian, B.R., A.D. Miller, and G.R. Foulger, Non-double-couple earthquakes 1. Theory, *Rev. Geophys.*, *36*, 525-549, 1998. doi:10.1029/98rg00716.
- Song, X.J., D.V. Helmberger, and L. Zhao, Broad-Band Modelling of Regional Seismograms: the Basin and Range Crustal Structure, *Geophys. J. Int.*, *125*, 15-29, 1996. doi:10.1111/j.1365-246X.1996.tb06531.

20 ShakeAlert: A Unified EEW System for California

Margaret Hellweg, Richard Allen, Maren Böse (Caltech), Holly Brown, Georgia Cua (ETH), Egill Hauksson (Caltech), Thomas Heaton (Caltech), Margaret Hellweg, Ivan Henson, Serdar Kuyuk, Doug Neuhauser

20.1 Introduction

Earthquake Early Warning (EEW) is a method of rapidly identifying an earthquake in progress and transmitting alerts to nearby population centers before damaging ground shaking arrives. The first few seconds of the initial P-wave arrivals at one or more stations are used to detect the event, and predict magnitude and peak shaking. Detections from several stations are combined to locate the event. A warning of imminent shaking can be used to activate automatic safety measures, such as slowing trains, isolating sensitive equipment, or opening elevator doors. Warnings can also be sent directly to the public via cell phone, computer, television, or radio.

With support from the United States Geological Survey (USGS), the California Integrated Seismic Network (CISN) hosted a three-year proof of concept project for EEW algorithms in 2006-2009. Following that successful project, the Berkeley Seismological Laboratory (BSL) together with its CISN EEW partners, the California Institute of Technology (Caltech), and the Swiss Institute of Technology Zürich (ETH), is collaborating on an integrated, end-to-end demonstration system for real-time EEW in California. The new system, called CISN ShakeAlert, is capable of continuous long-term operation and rapidly provides alerts to test users in the state.

20.2 Project Status

The ShakeAlert system combines the best aspects of the three methods from the proof-of-concept project. Caltech's OnSite algorithm uses P-wave data from the single station nearest the epicenter to provide extremely rapid estimates of likely ground shaking. The BSL's ElarmS algorithm and ETH's Virtual Seismologist algorithm use data from several stations around an event epicenter to produce a slightly slower but more reliable estimate of magnitude and location. Combining these methods produces an algorithm which has the speed of a single-station method but is then promptly confirmed and adjusted by additional station data to form a more accurate description of the event. When an identified event exceeds a defined combination of magnitude, ground shaking intensity and statistical likelihood, information is broadcast to system users. Currently, during the development phase, only project participants receive event information. In January 2012, test users outside the seismological community began to receive alert information. The recipients include the state's emergency operations center at the California Emergency Management

Agency (CalEMA). A schematic diagram of the end-to-end system is shown in Figure 2.38.

20.3 ElarmS Developments

During the past year, we have worked extensively to improve UC Berkeley's contribution to the system, ElarmS and the Decision Module (see Section 21). We implemented updated and streamlined waveform processing software. As a result, data are now available several seconds earlier than before, especially data from Q330 data loggers. This new waveform processing system is now on our operational computers, improving robustness and reliability. In addition, we have released and are operating a revised version of the ElarmS code, ElarmS-2. During the proof of concept phase, the code detecting earthquakes and preparing alerts was simply the original research software. During the current project, we have rewritten and modernized the ElarmS software. The new version has been the operational version since March 2012, and is producing and publishing alerts for the entire state. Elarms-1 only published alerts for the greater San Francisco Bay Area. Results from Elarms-2 are shown in the map of Figure 2.39. We have also been working hard to exclude false alerts from distant earthquakes.

20.4 Perspectives

July 2012 marks the end of the current USGS-funded project. We look forward to continuing to maintain, operate and improve the demonstration EEW system with continued support from the USGS, with particular emphasis on the interaction with EEW users. During the past year, we received support from the Moore Foundation, together with Caltech and the University of Washington, to begin development of a West Coast Earthquake Early Warning system. Important tasks for this project include the development of tools to quickly evaluate large and great earthquakes using GPS measurements and finite fault analysis. We envision including these new tools in our current operational system.

20.5 Acknowledgements

This project is supported at UC Berkeley by USGS Cooperative Agreement G09AC00259, at Caltech by Agreement G09AC00258, at USC/CEC by Agreement G09AC00255 and at ETH Zürich by Agreement G09AC00256. Funding from the Moore Foundation is under project number GALA 3024.

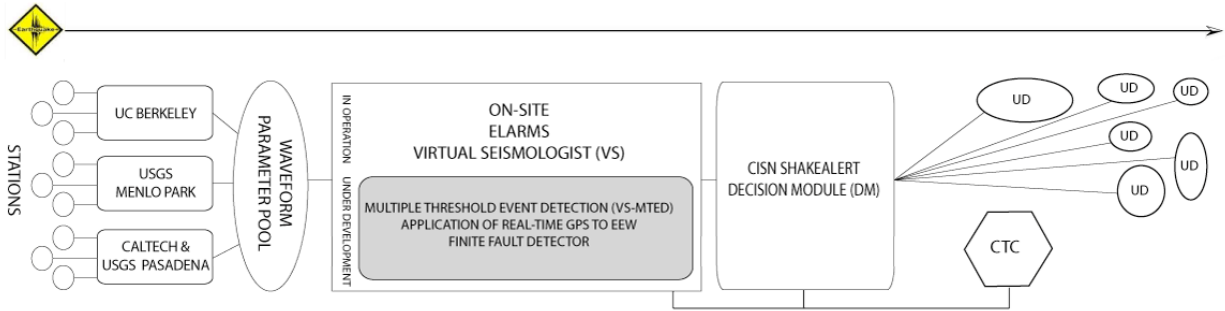


Figure 2.38: Components of the ShakeAlert EEW System. From left to right, the elements of the system are waveform processing, event detection, decision module (DM), CISN ShakeAlert user displays (UD), and the CISN testing center (CTC) software. *Waveform Processing:* Each data center processes telemetered digital waveform data collected from seismic stations throughout California. Critical waveform parameters are calculated from this data, then dumped into a statewide parameter pool. *Event Detection:* From the parameters, CISN’s EEW algorithms rapidly detect and characterize an event within seconds of its initiation. Several EEW detection algorithms run in parallel to provide the Decision Module with the best available source parameters. *Decision Module:* The DM combines earthquake information from each algorithm and delivers a “ShakeAlert” xml message about an earthquake in progress to subscribed users. *CISN ShakeAlert User Displays:* The ShakeAlert UD receives xml messages from the DM and displays their content in a simple and easily understandable way. *CISN Testing Center Software:* The CTC Software provides automated and interactive performance evaluations of ShakeAlert forecasts.

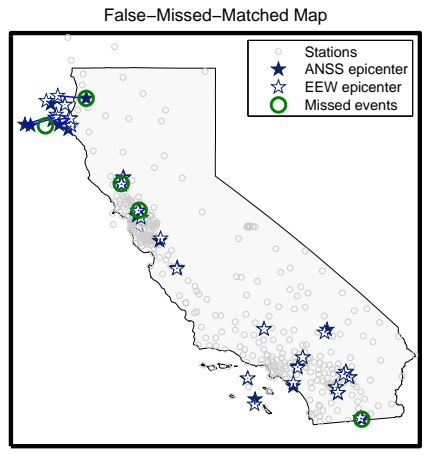


Figure 2.39: Map of California showing earthquakes from 6 Dec 2011 - 11 Jun 2012 with $M > 3.4$ for which ElarmS-2 produced alerts. Solid stars - ANSS epicenter; hollow stars - ElarmS-2 epicenter; circles - missed events. There were no false events (ElarmS-2 alerts when no earthquake was reported by CISN network operators) during this interval. At the edges of the network where station coverage is poor, like Cape Mendocino in Northern California, ElarmS-2 may mislocate events, but in most cases it still detects and reports them.

21 ElarmS Earthquake Early Warning

H. Serdar Kuyuk, Holly Brown, Richard Allen, Douglas Neuhauser, Ivan Henson and Margaret Hellweg

21.1 Introduction

ElarmS is a network-based earthquake early warning (EEW) algorithm developed at UC Berkeley for rapid earthquake detection, location and hazard assessment. ElarmS operates as part of the greater ShakeAlert EEW system, an ongoing project by the California Integrated Seismic Network (CISN). ShakeAlert combines three different EEW algorithms, one of which is ElarmS, into a unified system for providing warnings for events throughout the state. Output from the three algorithms is integrated by the ShakeAlert DecisionModule into a single alert messaging system. In this past year, the alert messages generated are being sent to external test users from several public and private, industry and governmental groups.

ElarmS consists of two primary modules: (1) a waveform processing algorithm, which runs in parallel at UC Berkeley, Caltech, and USGS Menlo Park to continuously filter real time seismic data, and (2) a single state-wide event detection algorithm which operates at UC Berkeley. The event detection module analyzes the incoming data from the three waveform processing streams and identifies earthquakes in progress.

21.2 Current Progress

From March 2011 to April 2012 ElarmS was sending event messages to ShakeAlert DecisionModule for events in the San Francisco Bay Area and Central Coast. In 2010 and 2011, we developed second generation ElarmS waveform processing and event detection algorithms, based in C++ for speed and adaptability. New more flexible communication software connects the remote waveform processing modules to the event detector. The new event detection module (E2) utilizes the established location and magnitude relations, but has an updated method of associating triggers together to form events. With the new updates E2 has been processing statewide real-time data since April 2012. Its new capabilities include: a) a split event check to prevent dual event alerts for a single event; b) linear teleseismic filtering to reduce teleseismic phase triggers; c) use of 1-second data package from BK network to increase speed; d) replay capability for past earthquake events; e) improved magnitude determination for southern California; f) improved location estimation; g) specific algorithms for offshore events; h) dynamic integration of station data from throughout California.

We are continuously inspecting and assessing system performance on a weekly basis. The assessment software

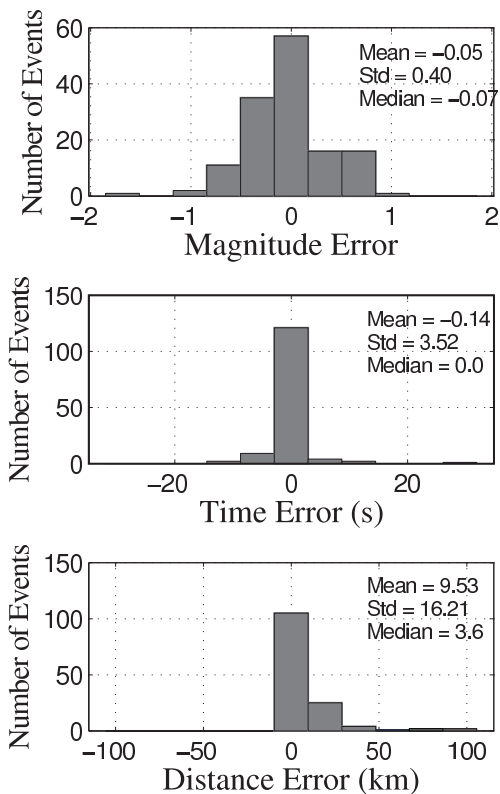


Figure 2.40: Performance of E2 for events $M > 2.5$ for about 4 months. Standard deviation of the magnitude, and origin time error are 0.4, 3.52 respectively. The median epicenter location error is 3.6 km.

automatically evaluates station latencies, promptness of alerts, accuracy of magnitude, location, and ground-shaking estimates, and number of successful event detections, false alarms, and missed events. This information is evaluated and E2 is being optimized based on performance.

In offline tests of performance using the latest version (Ev2.2) applied to the data from a period of ~ 4 months (December 6, 2011 to April 20, 2012) we find that E2 detected 164 events of magnitude 2.5 or greater in California and sent 4 false alerts, of which 3 are due to a single teleseismic event. In this period 22 events are declared with magnitude greater than 3.5 with 2 false and only one missed earthquake. For the greater Bay Area, 11 events were detected with magnitude greater than 3.5 with no false and no missed events. Figure 2.40 shows the performance of E2 for events $M > 2.5$ for the same period.

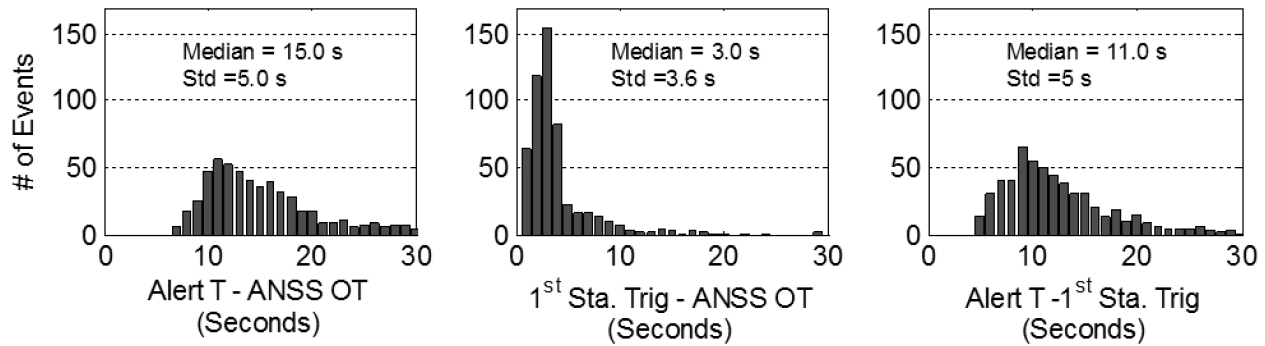


Figure 2.41: On average E2 declares events 15 seconds after origin time with a 5 second standard deviation. The initial P-waves take an average of 3 seconds to reach the first station, and the communications, processing and algorithms require an average of 11 seconds to declare an earthquake.

On average, E2 declared events 15 seconds after the origin time with a 5 second standard deviation. Initial P-waves take an average of 3 seconds to reach the first station, meaning that the communications, processing and algorithms require an average of 11 seconds to declare an earthquake (Figure 2.41).

21.3 Future Perspective

a) Investigation of GPS: in 2011 we also began investigating the use of GPS for earthquake early warning, focusing on the M_w 7.2 El Mayor-Cucapah earthquake, which had both real-time GPS and seismic data available. We developed a simple algorithm to extract the permanent displacement at GPS sites starting one oscillation after triggering on the dynamic long period signal. The estimate is continually improved with time. These permanent displacements can then be inverted for source characteristics given an approximate estimate of the fault plane. Initial results suggest that GPS would provide a valuable contribution to EEW. The new approach provides an independent estimate of magnitude, which is particularly important for the largest events. This approach is now being improved upon and applied to the M_w 9.0 2011 Tohoku-oki earthquake (see 22 in this volume).

b) Artificial Neural Network based pattern recognition of false events: in 2012 we began testing an Artificial Neural Network (ANN) filter at the end of ElarmS offline processing stream as a final "quakefilter" to catch false alerts before they are released to users. The ANN reads input data (an earthquake alert message) and the desired output (true or false) for a large dataset of sample events, and optimizes a mapping function between inputs and outputs. That function can then be utilized on future events to filter out alerts with a high probability of being false.

When ElarmS requires four stations to confirm an event -which is the case for the current online system-

the ANN could not improve on the current ElarmS results which has a 4% false alert rate. When ElarmS is reconfigured (offline) to send alert messages with only two or three stations the number of false alerts increases significantly. However, application of the ANN halves the false alert rate, from 15% to 8%.

One possible approach is therefore to allow ElarmS to detect events with just 2 or 3 triggers, apply the ANN filter to reduce false alerts, and then release the event alerts indicating the higher probability of a false alert. Once an event has four stations reporting, ElarmS would bypass the ANN completely and revert to the current standard alert criteria, thus avoiding any risk of the ANN mistakenly filtering out a real earthquake unlike the events it has seen to date, e.g. a very large earthquake. However, the ANN presents the option of sending faster, lower-certainty alerts, which would then be confirmed or improved seconds later when four stations have triggered. As always, users could choose whether to receive the earlier, lower certainty alerts or not.

21.4 Acknowledgements

This project is funded by USGS/NEHRP award G09AC00259 and by the Gordon and Betty Moore Foundation.

21.5 References

- Brown, H., R.M. Allen, M. Hellweg, O. Khainovski, D. Neuhauser, and A. Souf, Development of the ElarmS methodology for earthquake early warning: Realtime application in California and offline testing in Japan, *Soil Dynamics and Earthquake Engineering.*, 31, 188-200, 2011.
- Allen, R.M., Seconds before the big one, *Scientific American*, 2011.
- Allen, R.M. and A. Ziv. Application of real-time GPS to earthquake early warning, *Geophys. Res. Lett.*, 38, 2011.

22 Earthquake Early Warning with GPS Data

Simona Colombelli (University of Naples) and Richard Allen

22.1 Introduction

The combined use of seismic and geodetic observations is now a common practice for finite-fault modeling and seismic source parametrization. With the advent of high-rate 1Hz GPS stations the seismological community has recently begun looking at GPS data as a valid complement to the seismic-based methodologies for Earthquake Early Warning (EEW).

In the standard approaches to early warning, the initial portion of the P-wave signal is used to rapidly characterize the earthquake magnitude and to predict the expected ground shaking at a target site, before the arrival of the most damaging waves. Whether the final magnitude of an earthquake can be predicted while the rupture process is underway, still represents a controversial issue; the point is that the limitations of the standard approaches when applied to giant earthquakes have become evident after the experience of the M_w 9.0, 2011 Tohoku-Oki earthquake.

Here we explore the application of GPS data to EEW and investigate whether they can be used to provide reliable and independent magnitude estimations. The large size and the complex rupture process, together with the huge number of high-quality GPS records available, make the 2011 Tohoku-Oki earthquake a unique and ideal case-study for our purposes.

22.2 Seismic vs. GPS data

Because EEW systems are essentially applied to moderate-to-strong earthquakes, large, dynamic, accelerometric sensors are generally used for real-time seismic applications. These instruments are able to record unsaturated signals without risk of clipping at the arrival of the strongest shaking. Accelerometer waveforms are usually integrated twice to obtain displacement time-series and a high-pass causal Butterworth filter is finally applied to remove the artificial effects and long-period drifts introduced by the double integration operation (Boore, 2002). The application of the high-pass filter, while removing the artificial distortions, reduces the low-frequency content of the recorded waveforms, resulting in the complete loss of the low-frequency energy radiated by the source and of the static displacement component. The effect of such a filtering is even more relevant for very large earthquakes, whose corner frequency is expected to be lower or comparable with the cut-off filtering frequency (typically 0.075 Hz). Since GPS stations are able to register directly the ground displacement without any risk of saturating and any need of compli-

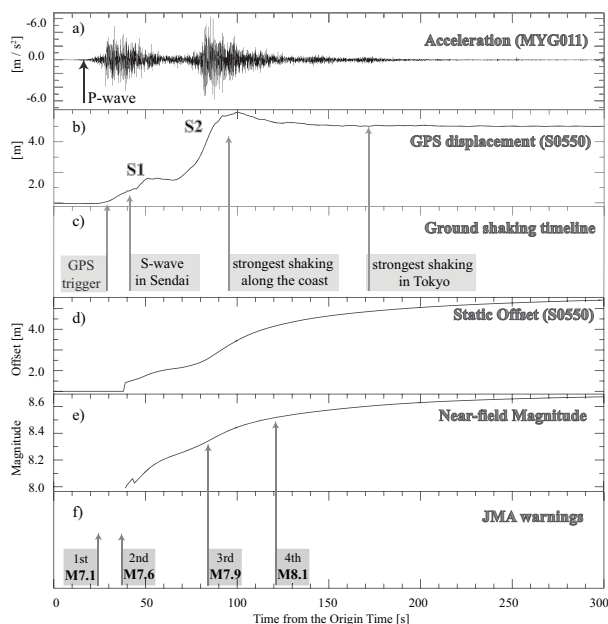


Figure 2.42: a) acceleration waveform at the closest seismic station (MYG011); b) displacement waveform at the closest GPS station (S0550), co-located with MYG011 station; c) timeline showing when the GPS information is available with respect to the time at which the strongest shaking occurs in the Sendai and Tokyo regions; d) output of the algorithm for the static offset extraction at the S0550 station; e) magnitude estimation from the closest GPS station with the point source and the near-field condition approximations; f) timeline of the JMA warnings and magnitude updates.

ated artificial corrections, geodetic displacement time-series represent the complementary contribution to the high-frequency information provided by seismic data.

Figure 2.42 shows a comparison between the acceleration (a) and the GPS displacement (b) waveforms of the Tohoku-Oki earthquake, recorded at two co-located stations (MYG011 from the K-Net network and S0550 from the GEONET network, respectively). Both records show evidence of two main phases (denoted as S1 and S2 in the figure) that correspond to two distinctive, time delayed episodes of slip release during the rupture process (Lee *et al.*, 2011). The GPS displacement starts to be evident later than the P-wave arrival on the seismic record and approximately at the same time of the S-wave arrival and the period of strong shaking. As it can be inferred from the timeline of Figure 2.42c, the P-wave onset at the

closest seismic station (MYG011) occurs approximately 15 seconds after the Origin Time (O.T.), while the first GPS information is available around 40 seconds after the O.T. The maximum amplitude on the GPS record for both phases is almost coherent in time with the arrival of the strongest shaking (on the acceleration waveform) at the same place. However, this does not prevent the use of these data and the issuance of a warning with the expected ground shaking at more distant sites. For example, in the Tokyo region the maximum shaking occurs about 170 seconds after the O.T., well after the GPS displacement has reached its maximum value at the closest station.

22.3 Real-Time offset extraction

We analyzed the co-seismic ground deformations produced by the 2011 Tohoku-Oki earthquake collected by the Japanese GPS Earth Observation Network (GEONET) (*Sagiya, 2004*). In order to extract the permanent displacement, we used the algorithm developed by *Allen and Ziv (2011)*. The algorithm looks for a trigger along the records and declares the first-arrival onset when a pre-determined condition on the short-term vs. long-term average is satisfied (*Allen, 1978*). Starting from the trigger time, a running average is then computed along the waveforms and is delivered as a real-time estimation of the static offset. As an example, Figure 2.42d shows the permanent displacement extracted from the S0550 station.

The running average computation is expected to remove the dynamic component of the signal, which would affect the estimation of the static offset. However, to prevent the possible inclusion of a dynamic oscillation, the algorithm starts to deliver the running average after two trigger-amplitude crossings or 10 seconds after the trigger time, whichever comes first.

22.4 Rapid magnitude estimation

The static displacement resulting from the algorithm is then used to obtain a fast estimation of the earthquake magnitude. A quick and preliminary estimation of the earthquake size can be obtained by adopting the theoretical scaling relationship between the earthquake magnitude and the near-field static offset. In case of a very small fault (i.e., a point source) and at short distances from the source (i.e., in the near-field condition), the primary component of the static displacement u can be written as:

$$u \propto \frac{1}{4\pi\mu R^2} M_0(t)$$

where μ is the rigidity modulus of the medium, R the hypocentral distance and $M_0(t)$ the seismic moment. We applied the previous formula to the static offset of the closest station. The result is plotted in Figure 2.42e and

shows that the magnitude is fairly well reproduced, despite the approximations and the limited conditions of the formula. This is especially true when our result is compared with the output of the JMA warning system (Figure 2.42f), whose magnitude estimations were largely underestimated for the entire duration of the event. However, a weak systematic underestimation of the final magnitude value (with respect to the official value, $M_w = 9.0$) is evident from the plot. We infer that this underestimation is essentially due to the point source approximation, whose effect may become significant whereas the extended dimension of the fault cannot be neglected.

An approach that may be more robust is inversion for the static slip on the fault plane, which allows consideration of the contributions from the entire fault plane and may provide a better estimation of the earthquake magnitude. We are currently working on the implementation of a real-time static slip inversion scheme using a constant-slip, rectangular source embedded in a homogeneous half-space (*Okada, 1985*). Our goal is to develop an efficient methodology for both the rapid determination of the event size and for the near real-time estimation of the rupture area. This would allow for a correct evaluation of the expected ground shaking at the target sites, that represents, without doubt, the most important aspect of the practical implementation of an early warning system and the most relevant information to be provided to the non-expert, end-user audience.

22.5 Acknowledgements

This work was supported by the University of Naples Federico II and a grant from the Moore Foundation.

22.6 References

- Allen, R.V. Automatic earthquake recognition and timing from single traces, *Bull. Seism. Soc. Am.*, 68, 5, 1521-1532, 1978.
- Allen, R.M. and A. Ziv. Application of real-time GPS to earthquake early warning, *Geophys. Res. Lett.*, 38, 2011.
- Boore, D.M. Comments on Baseline Correction of Digital Strong-Motion Data: Examples from the 1999 Hector Mine, California, Earthquake, *Bull. Seism. Soc. Am.*, 92, 4, 1543-1560, 2002.
- Lee, S.-J., B.-S. Huang, M. Ando, H.-C. Chiu, and J.-H. Wang. Evidence of large scale repeating slip during the 2011 Tohoku-Oki earthquake, *Geophys. Res. Lett.*, 38, 2011.
- Okada, Y. Surface deformation due to shear and tensile faults in a half-space, *Bull. Seism. Soc. Am.*, 75, 4, 1135-1154, 1985.
- Sagiya, T. A decade of GEONET: 19942003 The continuous GPS observation in Japan and its impact on earthquake studies, *Earth Planets Space*, 56, xxixxi, 2004.

23 GPS Rapid Response to Moderate Earthquakes: A Case Study of the Alum Rock Earthquake

Ingrid A. Johanson

23.1 Introduction

The 2007 M5.5 Alum Rock earthquake is used to investigate the possible performance of real-time GPS stations in the San Francisco Bay Area. The Alum Rock earthquake was a moderate earthquake on the Calaveras fault, near several GPS stations with 1 sample per second (sps) data available. Murray-Moraleda and Simpson (2009) found nearby stations to have several mm of coseismic displacement from daily processed results, and found some to have measurable postseismic displacements (see first figure at right). The Alum Rock earthquake is used in these tests because it is the largest earthquake in the SF Bay Area since 1 Hz GPS data has been widely collected. However, it represents the smaller end of earthquakes that are likely to have detectable offsets using epoch-by-epoch processing. These tests therefore show the capabilities of high-rate GPS for a challengingly small event.

23.2 Real-time vs. Rapid Post-processing

While real-time processing of GPS data is capable of providing measurements of displacement within seconds of its occurrence, post-processing provides results with lower noise levels, leading to better precision. The differences will be especially important for a moderate earthquake with offsets of less than ~ 1 cm. GPS may not be critical in earthquake early warning for a moderate event, but it can still provide information that will be useful for rapid response. In frames A1, B1, and C1 of Figure 2.43, 1 sps GPS observations were processed with TrackRT in rewind mode (developed by Tom Herring at MIT) and with IGS Ultra-rapid orbit files. In general the processing provided clean results with a high percentage of resolved integer ambiguities and over a six-hour period the 4 stations had a RMS of 000.

These can be compared with frames A2, B2, and C2, which show post-processing using Track and Ultra-Rapid orbits with data from 2 hours before the event origin time and up to just 1 minute after. These results have considerably less long period noise and in the cases of A2 and B2 clearly show an offset that was not visually apparent in the real-time results. Processing of data up to 10 minutes after the earthquake origin is shown in frames A3, B3, and C3, and does not show major differences with processing up to just a minute after. Nor does processing of the entire day of data (not shown). This indicates that rapid post-processing can produce time series

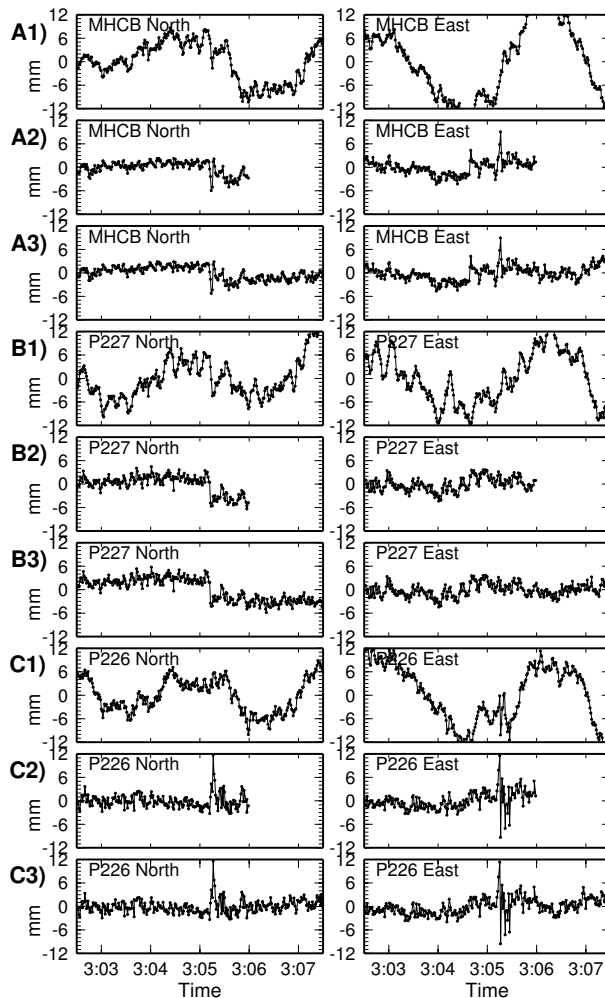


Figure 2.43: Time series of East and North motions for A) MHCB, B) P227 and C) P226. Frames numbered with 1) are from TrackRT rewind, 2) are post-processed with Track with up to 1 minute of post-earthquake data, 3) have 10 minutes of post-earthquake data. Note that the plots are in GPS time, such that the earthquake origin time would plot as 3:05:09.

that are just as precise as those covering a longer time span and considerably less noisy than real-time. With post-processing after only one minute, results could be available within 2-3 minutes for use in fault plane determination and finite fault models and could easily be repeated at various intervals for earthquakes with longer shaking.

23.3 Offset determination

The second comparison is between two methods to measure the size of an offset at the time of the earthquake. In this section, only post-processed results were used. The time of the offset was treated as a known and evaluation windows of 10, 30 and 45 seconds were tested. In all cases the before-event timespan was equal to the after-event timespan.

The median method defines the pre- and post-earthquake positions as the median positions during the evaluation windows. It has the advantage of being relatively insensitive to the large excursions in position that can happen during shaking. However, it has the disadvantage that it will continue to evolve with time. That is, it will include the effects of long wavelength noise or rapid postseismic motions. This method performed best with the smallest evaluation window tested (10s) and produced offsets that matched the size of the offsets from daily observations to a reasonable degree (Figure 2.44B).

The line-fitting method fits lines to the displacements before and after the offset time, within the evaluation windows. Unlike in the median method, the pre- and post- positions are extrapolated to the offset time and it is determined from their difference. This mitigates the effect of long-wavelength drift, but leads to large fluctuations in calculated offset in the first 10-15 seconds. This method tends to overestimate the offsets when the 10s window is used and even with the 30s window (shown in Figure 2.44A), the sizes of the offsets are as much as twice that of the results from daily solutions. However this method provided good azimuth estimates and a very good fit to station MHCB.

23.4 Conclusions

For rapid response applications during a moderate earthquake, there is still useful information to be gained by using rapid post-processing. The post-processed results will provide less noisy displacements and more accurate offset estimates. Post-processing can occur 1 minute after an event (or even sooner) and provide results in 2-3 minutes. To determine the offsets, either the median or the line-fitting methods will provide reasonable results. The line fitting method provides better azimuths in this case study, which would be important for fault plane determination. However the overshoot in size could lead to overestimates of the amount of slip in an inversion.

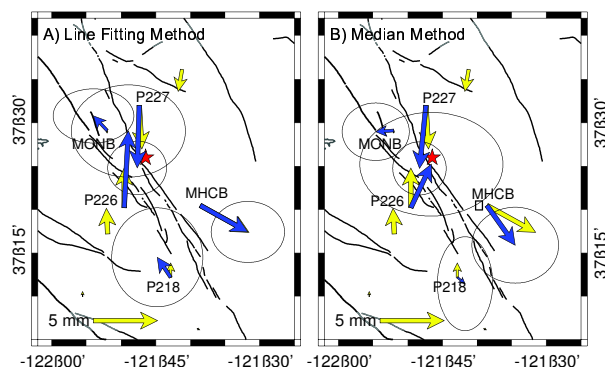


Figure 2.44: Velocity fields showing offsets determined from A) the line-fitting method and B) the median method (blue vectors). In both cases, these are from post-processing using up to 1 minute of post-earthquake data. The rapid results are compared to coseismic offsets determined by Murray-Moraleda and Simpson (2009) from post-processed daily GPS solutions (yellow vectors). The Alum Rock epicenter is shown by the red star.

23.5 References

Murray-Moraleda, J. R., and R. W. Simpson, Geodetically Inferred Coseismic and Postseismic Slip due to the M 5.4 31 October 2007 Alum Rock Earthquake. *Bull. Seismol. Soc. Am.*, 99(5), 2784-2800, 2009.

24 Using Smartphones to Detect Earthquakes

Qingkai Kong, Richard Allen, Stephen Thompson, Jonathan D. Bray, Ana Luz Acevedo-Cabrera

24.1 Introduction

We are exploring the use of accelerometers in smartphones to record earthquakes. We have developed an application for Android phones based on previous work with iPhones to record the acceleration in real time. These records can be saved on the local phone or transmitted back to a server in real time. A series of shake table tests were conducted (and more tests will be conducted soon) to evaluate the performance of the accelerometers in these smartphones by comparing them with high quality accelerometers. We also recorded different human activities using these smartphones. Different features were extracted from the recordings and were used to distinguish earthquakes from daily activities. We implemented a classifier algorithm based on an artificial neural network, which shows a 99.7% successful rate for distinguishing earthquakes from certain typical human activities

24.2 Data Sources

Two kinds of smartphones have been used in this research: iPhone and Android phones. The applications on these phones are iShake and droidShake. Data was collected mainly in three ways: (1) Continuous recording of different human activities, e.g. walking, running, sitting, taking the bus, etc. (2) Trigger-based data from various users sent to a server. This method requires that the phone stay steady for certain amount of time. Then, if the acceleration exceeds the pre-determined threshold, it triggers the algorithm to send data before and after the trigger to the server. (3) Data recorded during the shake table tests with earthquake input signals. These three types of data were used to distinguish earthquake signals from non-earthquake signals.

24.3 Detection Method and Classifier

A high pass filter was first applied to the data in real time to eliminate the baseline offset. Then the filtered data was divided into segments using a series of sliding windows. From each of the sliding windows, three parameters were extracted to characterize different types of signals, including maximum number of zero crossings from the three components, peak acceleration, and the ratio of peak velocity over peak acceleration from the vector sum of the three components. These three parameters were then used as input to train the neural network to distinguish earthquakes from non-earthquake signals.

A 10-fold cross validation method was used to determine the optimal size of the time window and the num-

Table 2.1: Confusion Matrix

		Target Class		%
		Non-EQ	EQ	
Predict Class	Non-EQ	584	3	99.5%
	EQ	1	582	99.8%
%		99.8%	99.5%	99.7%

ber of neurons in the neural network. Based on the cross validation results, a 150 sample length of time window was found to be optimum, and one hidden layer with 19 neurons was used to configure the neural network.

24.4 Results

The output of the neural network is “earthquake” or “non-earthquake.” The results are shown in the confusion matrix in Table 2.1. The overall success rate is 99.7%. Figure 2.45 shows the peak acceleration and maximum number of zero crossings for different activities and earthquake signals. It is obvious that these two parameters alone could distinguish most of the earthquakes from other human activities. The test of the neural network is shown in Figure 2.46

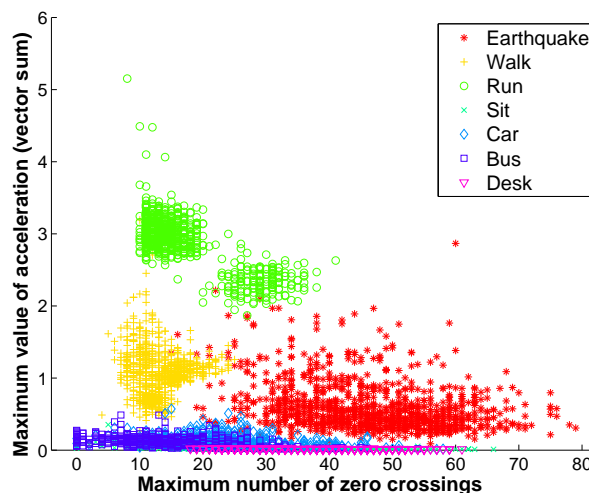


Figure 2.45: Maximum value of acceleration vs maximum number of zero crossings

24.5 Conclusion and Future Work

This initial study shows the potential of using smartphones to detect earthquakes. By using multiple phones in the future, we can achieve higher accuracy. A network

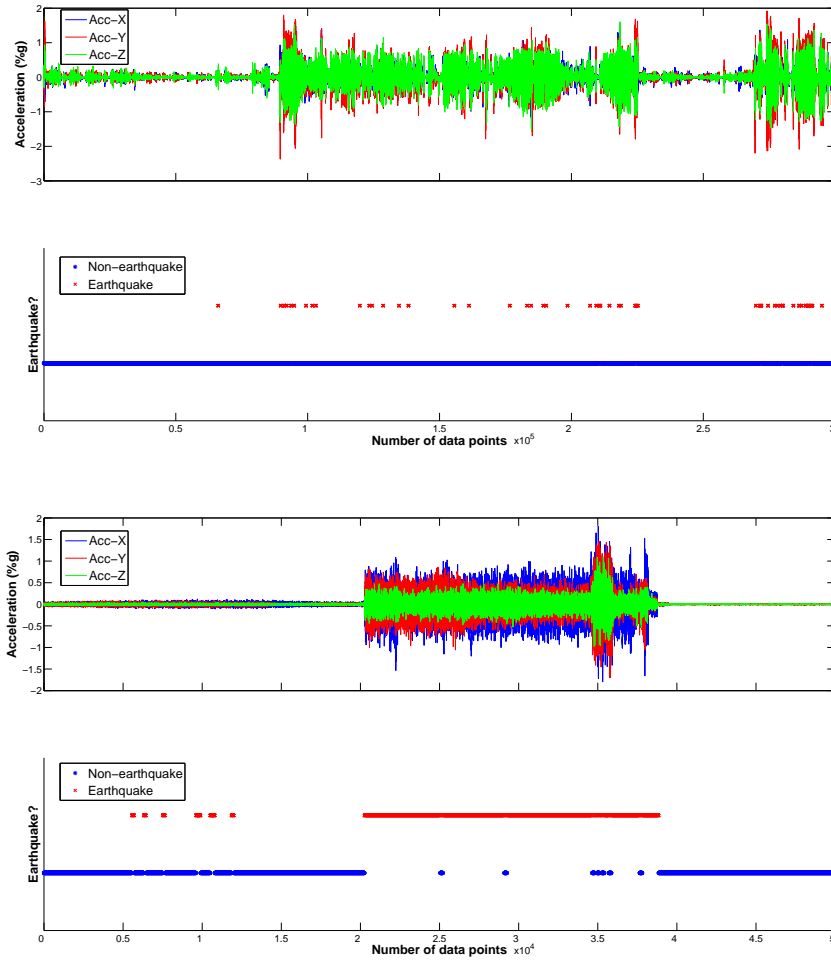


Figure 2.46: Algorithm Test: Figures show the detection of non-earthquakes and earthquakes using the artificial neural network model developed. The upper two panels show the waveform and the detector output for an accelerogram recorded for different random activities. This random record consisted of various activities within about two hours, including walking, running, jumping, riding in a vehicle, and so on. In 97% of cases, the windows were classified correctly as non-earthquake signals. The lower two panels show the detection using data recorded by the phone when it was placed on a shake table. Once the shake table starts to move, the algorithm correctly classifies most of the movement as an earthquake.

consisting of these smartphones may work as a supplemental network to the current traditional network for scientific research and real-time applications.

24.6 Acknowledgements

The shake table tests for the iPhones were arranged and conducted by Jonathan Bray, Alex Bayen, Shideh Dashti, and Jack Reilly. This project is funded by Deutsche Telekom and CITRIS. Markus Neubrand, Angela Nicoara, Louis Schreier and Arno Puder from Deutsche Telekom provided the Android phones and the droidShake application.

24.7 References

- Bao, L. and Intille, S. S., Activity recognition from user-annotated acceleration data, In *Proc. of the 2nd Int. Conf. on Pervasive Computing*, 1-17, 2004.
- Dashti, S., Reilly, J., Bray, J.D., Bayen, A., Glaser, S. and Mari, E., iShake: Using Personal Devices to Deliver Rapid Semi-Qualitative Earthquake Shaking Information, *GeoEngineering Report, Depart. of Civil and Environ. Engineering, Univ. of California, Berkeley*, 2011.
- M. Fahriddin, M. G. Song, J. Y. Kim, and S. Y. Na, Human Activity Recognition Using New Multi-Sensor Module in Mobile Environment, 2011.

25 Probing the Deep Rheology of Tibet: Constraints from 2008 M_w 7.9 Wenchuan, China Earthquake

Mong-Han Huang and Roland Bürgmann

25.1 Introduction

The time-dependent surface deformation after a large earthquake reflects the response to the redistribution of stresses induced by the earthquake and can be used to probe the viscous strength of the lithosphere. However, processes such as aseismic afterslip and aftershock-related deformation can also contribute to the postseismic deformation. The 2008 M_w 7.9 Wenchuan earthquake occurred on the eastern flank of the Tibetan Plateau and its postseismic deformation gives us an opportunity to examine the long lasting question of whether the growth of the Tibetan Plateau is by brittle crustal thickening or by lower crustal flow. We use finite element modeling of viscoelastic relaxation with lateral heterogeneity applied for the calculation of the 1.5 year postseismic displacement. A layered dislocation model is also tested for contributions of afterslip on the down-dip extension of the rupture or a shallow detachment. In the SW Longmenshan, the lower crustal flow model can explain the near- to far-field deformation in space and time. In the NE Longmenshan, the lower crustal flow alone cannot produce the localized deformation observed there. As a result, the postseismic displacement of the Wenchuan earthquake is dominated by the relaxation from the lower crust, but locally contributed to by the afterslip on the shallow part.

25.2 Method and Data

We use both an analytical solution (Pollitz, 1992) and finite element modeling software *ABAQUSTM* to calculate the postseismic deformation due to viscoelastic relaxation. The Wenchuan earthquake fault geometry is based on Shen *et al.*, 2009, based on geodetic inversion of coseismic deformation. Our simplified fault geometry is composed of five segments with different slip rates, extends to a depth of 20 km, and runs along the 285 km Longmenshan fault zone (Figure 2.47c). Thirty-six cGPS stations are deployed on both sides of the Longmenshan fault zone and obtain about 1.5 years of postseismic displacement observations (Figure 2.47c,d). Twenty two ENVISAT interferograms are generated using the software ROI PAC 3.0, and the 90 m SRTM DEM is used to correct the phase due to the topography. The InSAR time series obtained from the 22 interferograms reveals the postseismic displacement from June 2008 to December 2009.

25.3 Results

The InSAR time series shows 7-9 cm postseismic displacement in line of sight in the near-field 1.5 years after the Wenchuan main shock, and drops to 3-6 cm in the region 50 km away from the surface rupture (Figure 2.47b). In addition, surface creep is observed in the NE Longmenshan, which implies that shallow afterslips occurred in the NE region. All cGPS time series data show transient displacements in the horizontal and vertical components. The 1.5 year observations show southeastward displacement in the SW and northeastward displacement in the NE Longmenshan. Significant postseismic uplift in the SW Longmenshan is observed from the GPS measurements (Figure 2.47c) as well as the InSAR time series (Figure 2.47b).

The results of the numerical modeling show that an inferred 35 km thick lower crustal flow with viscosity of 2×10^{18} Ps s under eastern Tibet can explain both spatial and temporal patterns of the postseismic displacement. On the other hand, the best fitting afterslip model requires more than 50 cm of slip below 40 km depth, which might be below the brittle-ductile transition zone and is unlikely to produce such a high dislocation in a short time scale. Besides, there is no significant correlation between the repeating microearthquakes (data by Li *et al.*, 2011) after the main shock and the afterslip model. Consequently, in the SW Longmenshan, the lower crustal flow model can explain the near- to far-field postdeformation in space and time. However, the afterslip on the shallow part of the fault plane appears to contribute to the deformation along this strike-slip dominated portion of the rupture.

25.4 Acknowledgements

We thank Prof. Z.-K. Shen of Beijing for providing the GPS time series. M.-H. Huang thanks Prof. Andy Freed for instruction on *ABAQUSTM*. This work is supported by NSF grant (EAR 0738298).

25.5 References

- Li, L., Q. Chen, F. Niu, and J. Su, Deep slip rates along the Longmen Shan fault zone estimated from repeating microearthquakes. *J. Geophys. Res.*, 116, B09310, doi:10.1029/2011JB008406, 2011.
- Pollitz, F., Postseismic relaxation theory on a spherical earth. *Bull. Seism. Soc. Am.*, 82, 1, 422-453, 1992.
- Shen, Z.K., J. Sun, P. Zhang, Y. Wan, M. Wang, R. Bürgmann, Y. Zeng, W. Gan, H. Hiao, and Q. Wang, Slip maxima at fault junctions and rupturing of barriers during the 2008 Wenchuan earthquake, *Nat. Geosci.*, 2, 718-724, doi:10.1038/NNGEO636, 2009.

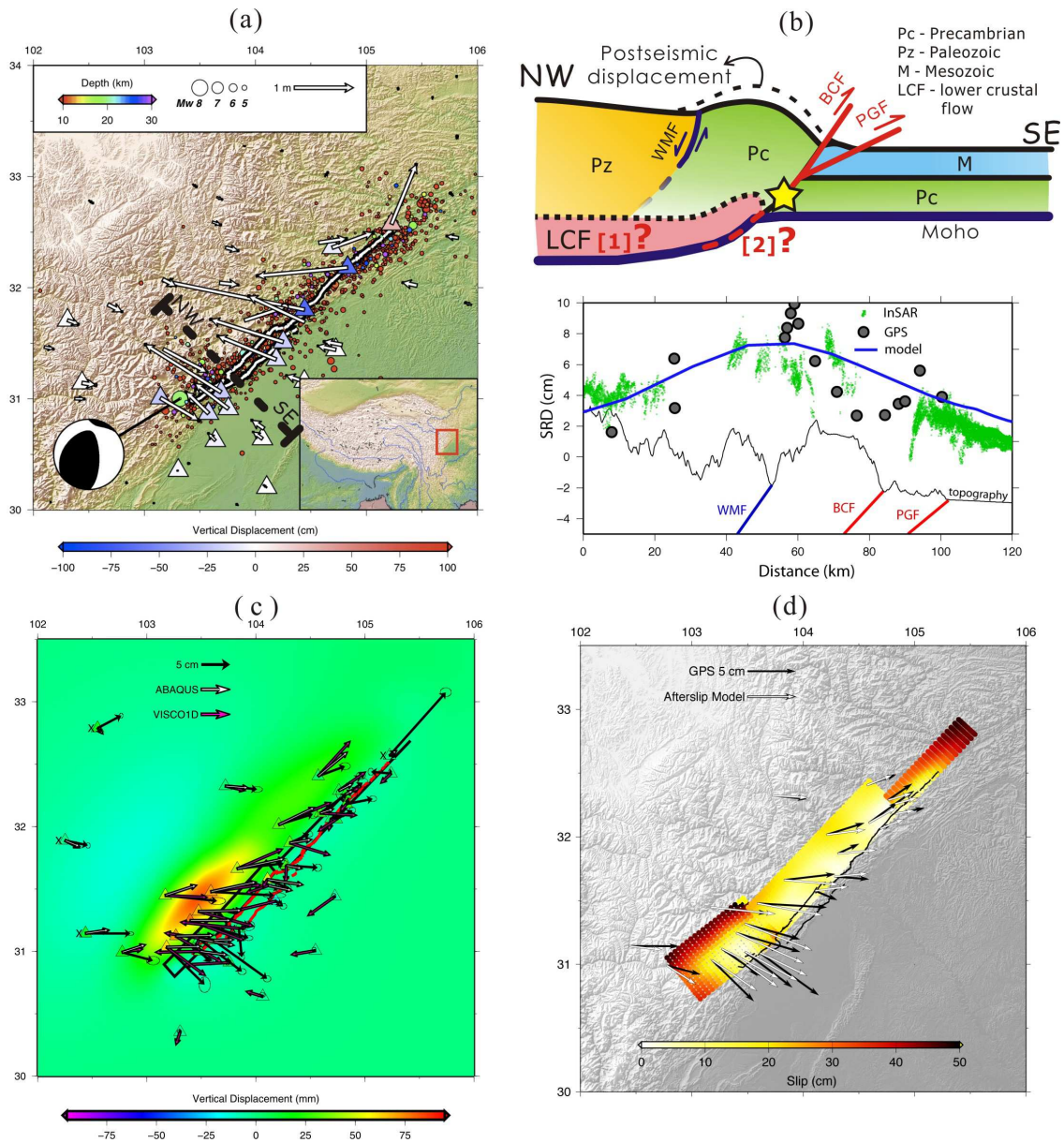


Figure 2.47: (a) The Wenchuan coseismic displacement. The white arrows are the GPS recorded coseismic displacement, and the colors in the triangles are the vertical displacement. The beach ball diagram shows the focal mechanism of the main shock, and the circles are the aftershocks color coded with depth. The white lines outline the coseismic surface rupture. The inset indicates the study area location at the edge of the Tibet Plateau. (b) Possible mechanism of Wenchuan postseismic deformation: [1] Relaxation of the lower viscous crust (pink region). [2] Afterslip in the down-dip extension of the earthquake fault. Lower figure shows the NW-SE profile of south Longmenshan (Figure 2.47a) with 1.5 years postseismic displacement observed by InSAR (green) and GPS (grey). The dark blue line is the forward model assuming viscoelastic relaxation from the lower crustal flow. (c) The predicted 1.5 years postseismic displacement. The black arrows are the GPS horizontal measurements, and the white and purple arrows are the *ABAQUS*TM and *VISCO1D* models, respectively. The background color is the *ABAQUS*TM predicted vertical displacement. (d) The afterslip model. The yellow to red circles are the fault geometry with down-dip extension to 60 km, color coded by afterslip. Note much larger slip located below 40 km that is probably below the brittle-ductile transition zone.

26 Global Waveform Tomography with the Spectral Element Method: A Second-Generation Upper-Mantle Model

Scott French, Vedran Lekic, and Barbara Romanowicz

26.1 Introduction

The SEMum model of Lekic and Romanowicz (2011) (SEMum v.1) was the first global V_S model obtained using spectral-element forward modeling (SEM: *Komatitsch and Vilotte, 1998*), and exhibits impressive amplitudes of heterogeneity in the upper 200km of the mantle compared to previous global models. Among other measures to make SEM-based modeling tractable, SEMum v.1 was developed using an homogenized crustal model of uniform 60km thickness (*Capdeville and Marigo, 2007*). While this choice is justifiable in the continents, it can potentially frustrate interpretation of shallow upper-mantle structure in the oceans. Here, we present an update to SEMum (SEMum v.2: *French et al., 2011*), which was obtained using an homogenized crust with more realistic laterally-varying thickness.

26.2 Methodology

Our approach to data processing and inversion largely mirrors that of Lekic and Romanowicz (2011). We employ a dataset identical to that of SEMum v.1, consisting of long-period ($60 \leq T \leq 400$ s) three-component waveforms of 203 well-distributed global earthquakes ($6.0 \leq M_w \leq 6.9$), as well as global group-velocity dispersion maps at $25 \leq T \leq 150$ s (*Ritzwoller, pers. comm.*). Dispersion at $T \leq 60$ s constrains our crustal model (Section 26.2), while, for consistency, the full period range is included in our mantle inversion.

Waveform inversion follows a hybrid approach, in which we forward model the global wavefield “exactly” using the SEM, while sensitivity kernels are calculated approximately using non-linear asymptotic coupling theory (NACT: *Li and Romanowicz, 1995*). The hybrid scheme represents a ≥ 3 x reduction in computation relative to a fully-numerical approach (*Tarantola, 1984*), and, together with the homogenized crustal model and mode-coupled SEM implementation (cSEM: *Capdeville et al., 2003*), renders SEM-based inversion tractable.

Crustal structure

Since cSEM uses modes to model wave propagation in the core, SEM time stability is instead dictated by crustal structure. This condition may be relaxed by *homogenizing* the crust (*Capdeville and Marigo, 2007*), wherein thin discontinuous layers are replaced with a single, smooth anisotropic layer valid at long periods (*Backus, 1964*). Unlike SEMum v.1, we now adopt a *variable* homoge-

nized crustal-thickness: similar to Crust2.0 Moho depth (*Bassin et al., 2000*), but spatially filtered and limited to the interval between 30 and 60km. Given this prescribed geometry, we seek radially-anisotropic structure that fits the group-velocity dispersion data ($T \leq 60$ s). Despite a 30km minimum thickness, the homogenized crust allows for ~ 4 x SEM time-step prolongation relative to Crust2.0.

In NACT, we adopt a crustal-correction scheme similar the modified linear corrections (MLCs) of Lekic *et al.* (2010), with the exception that we do not limit ourselves to a small set of “regionalized” crustal models: we obtain continuously-parameterized corrections, that directly reflect lateral variation in the crustal layer. Further, we developed an efficient scheme for calculation of NACT sensitivity kernels that honor lateral variation in Moho topography, thereby simplifying the parameterization of, and inversion for, mantle structure. A detailed discussion of these approaches appears in French *et al.* (in prep).

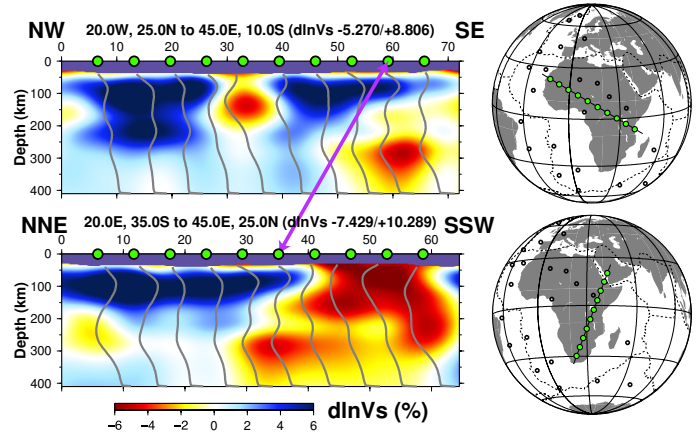


Figure 2.48: SEMum v.2 V_S structure beneath Africa; gray profiles sample 1D V_S , paths cross where indicated.

26.3 Results and Future Work

SEMum v.2 results from two iterative updates to v.1, wherein waveform fits (Table 2.2) consistently improve. Like v.1, v.2 exhibits strong heterogeneity: $>15\%$ peak-to-peak in close juxtaposition. For example, Figure 2.48 (lower panel) highlights the fast Kalahari and Tanzanian cratons, as well as very strong, bifurcated slow anomalies underlying the East African Rift through Afar, consistent with melt source-signature variation along the EAR (*Rogers et al., 2000*). Further, v.2 shows impressive low-velocity anomalies beneath numerous hotspots. Figure

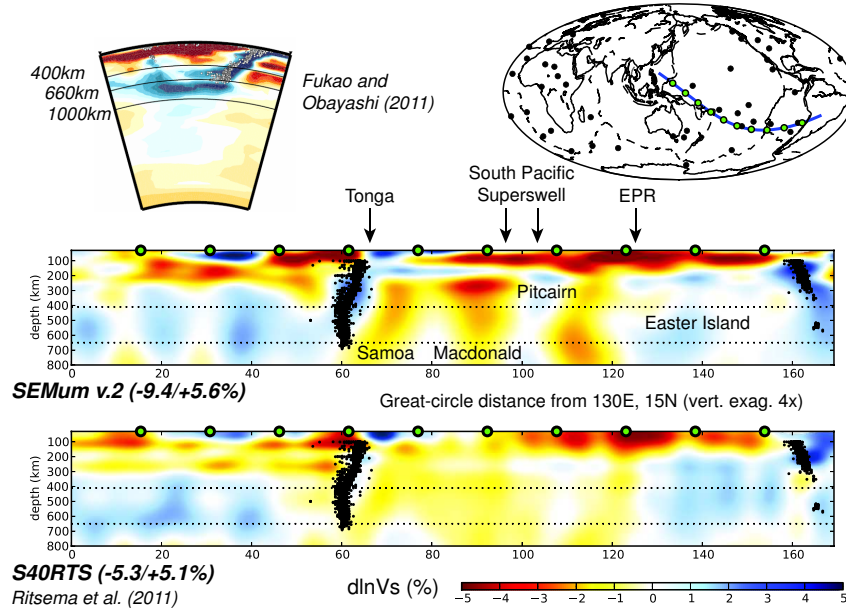


Figure 2.49: SEMum v.2 and S40RTS V_S structure beneath the South Pacific; deep seismicity highlights subducted slabs.

2.49 compares v.2 structure through the South Pacific with that of S40RTS (Ritsema *et al.*, 2011), highlighting strong columnar slow features beneath the Pacific superswell. Compare the prominent fast signatures of subducted slabs (South America, Tonga), and the similar pattern of slab stagnation west of Tonga, to that seen in the body-wave study of Fukao and Obayashi (2011, *pers. comm.*).

We are now preparing a manuscript for publication discussing SEMum v.2 methods and model structure, while also planning the next phase of our inversion: global adjoint tomography with SEMum v.2 as a starting model.

	L	T	Z
fundamental	66.0 [62.1]	75.4 [59.1]	67.6 [63.7]
overtone	80.2 [67.2]	70.9 [62.9]	78.1 [69.7]
mixed	73.3 [67.2]	81.6 [68.3]	75.7 [70.1]

Table 2.2: Waveform variance reduction (%) for SEMum v.2 and [v.1], by component and data type.

26.4 Acknowledgements

This work was supported by the NSF (NSF-EAR 0738284). SWF acknowledges support from the NSF Graduate Research Fellowship program. SEM calculations were performed on DOE NERSC resources.

26.5 References

Backus, G., Long-wave elastic anisotropy produced by horizontal layering, *J. Geophys. Res.*, 67, 4427-4440, 1962.

Bassin, C.G.L. & G. Masters, The current limits of resolution for surface wave tomography in North America, *EOS, Trans. Am. Geophys. Un.*, 81, 2000.

Capdeville, Y. & Marigo, J., Second order homogenization of the elastic wave equation for non-periodic layered media, *Geophys. J. Int.*, 170(2), 823-838, 2007.

Capdeville, Y., E. Chaljub, J.P. Vilotte, & J.P. Montagner, Coupling the spectral element method with a modal solution for elastic wave propagation in global earth models, *Geophys. J. Int.*, 152, 34-67, 2003.

French, S.W., V. Lekic, & B. Romanowicz, Toward global waveform tomography with the SEM: Improving upper-mantle images, Abstract S13C-02 presented at 2011 Fall Meeting, AGU, San Francisco, Calif., 5-9 Dec., 2011.

Komatitsch, D. and J.P. Vilotte, The spectral element method: an efficient tool to simulate the seismic response of 2D and 3D geological structures, *Bull. Seism. Soc. Am.*, 88(2), 368-392, 1998.

Lekic, V. & B. Romanowicz, Inferring upper-mantle structure by full waveform tomography with the spectral element method, *Geophys. J. Int.*, 185(2), 799-831, 2011.

Lekic, V., M. Panning, & B. Romanowicz, A simple method for improving crustal corrections in waveform tomography, *Geophys. J. Int.*, 182(1), 265-278, 2010.

Li, X.D. & B. Romanowicz, Comparison of global waveform inversions with and without considering cross-branch modal coupling, *Geophys. J. Int.*, 121, 695-709, 1995.

Tarantola, A., Inversion of seismic reflection data in the acoustic approximation, *Geophysics*, 49(8), 1259-1266, 1984.

Ritsema, J., A. Deuss, H.J. van Heijst, & J.H. Woodhouse, S40RTS, *Geophys. J. Int.*, 184, 1223-1236, 2011.

Rogers, N., R. Macdonald, J.G. Fitton, R. George, M. Smith, & B. Barreiro, Two mantle plumes beneath the East African rift system, *Earth Planet. Sci. Lett.*, 176, 387-400, 2000.

27 The DNA12 Seismic Velocity Model

Robert Porritt, Richard Allen, and Fred Pollitz

27.1 Introduction

The DNA velocity models have been following the rolling USArray from west to east. The initial model, DNA07 (Xue and Allen, 2010), used data from the earliest USArray deployment, the BDSN, and other regional networks. Obrebski *et. al.*, (2010) continue further east for DNA09, in which the interaction of the Yellowstone Plume and Juan de Fuca plate has a prominent role in the model. DNA10 updates the body wave dataset and develops the use of a joint inversion technique which uses Rayleigh wave phase velocities to constrain the upper lithosphere where teleseismic body waves rapidly lose resolving power (Obrebski *et al.*, 2011). In this research update we discuss the most recent generation of the DNA models, DNA12, in which we extend the dataset further east and include ambient seismic noise to resolve structure within the crust.

27.2 Method

The inclusion of surface wave data in the inversion provides constraints on the lithosphere allowing interpretation of structure from the surface through the mantle transition zone. However, the S-wave body-wave data is typically measured on the tangential component as it is a cleaner signal than the radial component. Nonetheless, in the presence of large anisotropic signals, there is a chance of mixing vertical and horizontal polarizations. To overcome this problem, we implement a rotation into the P-SV-SH coordinate frame with the predicted incidence angle (Bostock *et. al.*, 2001) and measure the arrival times on the three independent components.

The SV body wave delay times are jointly inverted with Rayleigh wave phase velocities. The phase velocities are generated by two independent methods. Teleseismic phase velocities are computed by Fred Pollitz using a non-plane wave method (Pollitz and Snoke, 2010). The phase velocities are updated from the dataset used in Obrebski *et. al.*, (2011) by using new USArray stations. Additionally, we employ ambient seismic noise to recover relatively short period phase velocities (Benson, *et. al.*, 2007). In this case, we update the dataset used in Porritt *et. al.*, (2011) to cover the continuous United States. The two surface wave models are joined by averaging with a period specific weighting parameter. This parameter allows for more weight to be given to the ambient noise at shorter periods where the ocean microseism produces strong ambient noise signal and more weight is given to the teleseismic phase velocities at longer periods where the signal is generally stable, but ambient noise has only

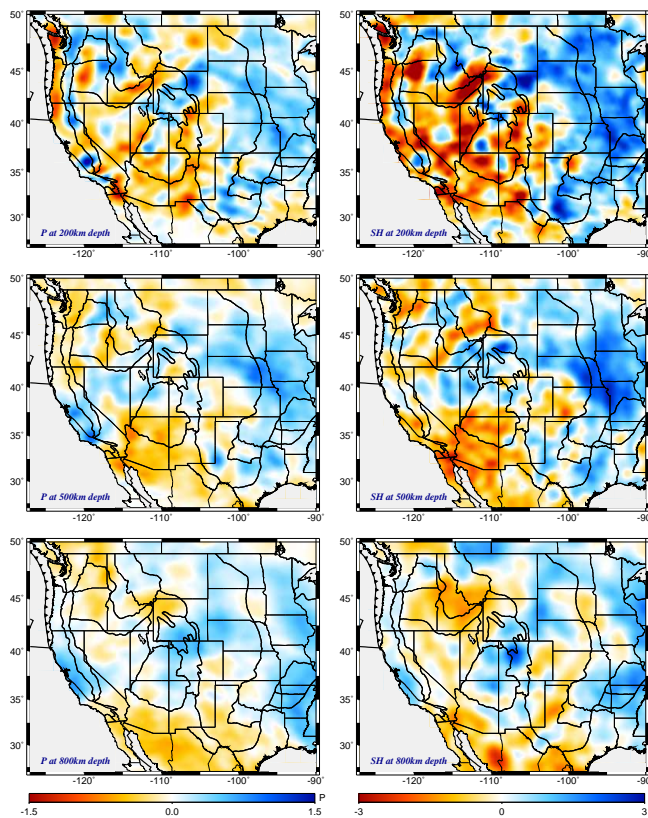


Figure 2.50: (left) Views of DNA12-P at various depths. (right) Corresponding views of DNA12-SH.

a weak signal.

27.3 Results

We focus this discussion on the Ancestral Rocky Mountains (ARM) region where there has been little resolution in previous versions of the DNA models. The ARM is a NW-SE trending series of uplifts and basins which formed in the mid-continent around 300Ma. Soreghan *et al.*, (2012) use potential field and active source seismic data to discuss the uplift and subsidence during the Mississippian through the Permian. They model the observed uplift as a NW-SE trending Cambrian rift system (the Southern Oklahoma Alucogen - SOA) being inverted due to crustal heterogeneity and a far-field horizontal stress field causing non-linear buckling. This horizontal stress field is attributed to the Ouachita-Marathon front which runs through southern Texas and was created by the collision of Africa with North America in the formation of Pangea (Kluth, 1986). Other authors (Algeo, 1992) have

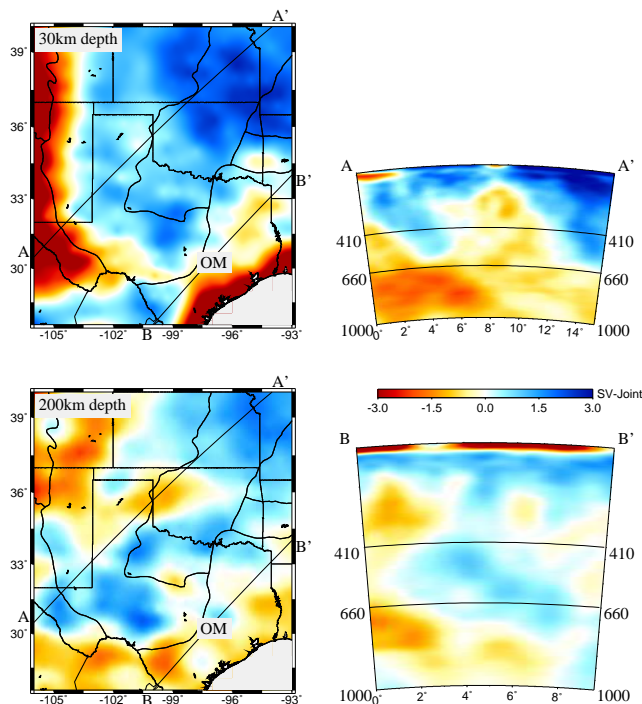


Figure 2.51: Views of the DNA12 model focused on the ARM. Maps at 30km and 200km depth are shown on the left with cross-section locations, physiographic boundaries, and state lines overlain. The Marathon-Ouachita Front (OM) is in southeast Texas near section B-B'.

suggested southward dipping subduction or wrenching of the Laurentia craton as the source of horizontal stress.

In Figure 2.51 we illustrate the velocity structure in the ARM region. The first feature we notice is the Ouachita-Marathon front in the 30km depth slice. The front is seen as a region of velocity contrasts where the generally high velocity cratonic lithosphere to the NW meets the area where the Pangean breakup occurred. In the asthenosphere, a high velocity body is imaged SW of the main uplifts dipping roughly to the NE and striking NW-SE. This high velocity body is distinct from the North American craton and the deeper Farallon slab system. One possible explanation is an independent subduction system which collided from the SW. Dating of igneous rocks in the ARM shows primarily Cambrian ages (Hogan and Gilbert, 1997) meaning any subduction in the region must have occurred 200 million years before the ARM uplift. Therefore we cannot conclude that subduction was the main force of ARM uplift, but a relic slab in the lithosphere could provide a buttress during the Pangean-forming orogeny, further forcing the stress into the SOA and resulting in the observed buckling.

27.4 Acknowledgements

We first thank UCB undergraduate Jenny Taing for picking a large portion of the teleseismic body wave data. Next, we thank Fred Pollitz for use of his surface wave phase velocities. Further, we wish to acknowledge the IRIS DMC webservices team who developed the Fetch-BulkData script we used for the data collection and the new collaborative earth model view. Additionally, we thank Earthscope and the Array Network Facility for the high quality data available through USArray. Finally, we thank NSF-EAR for funding this research as well as a UC Berkeley lab grant.

27.5 References

- Algeo, T.J., Continental-scale wrenching of south-western Laurussia during the Ouachita-Marathon orogeny and tectonic escape of the Llano block, *West Texas Geological Society Guidebook*, v. 9292, p. 115131, 1992.
- Bensen, G.D., M.H. Ritzwoller, M.P. Barmin, A.L. Levshin, F. Lin, M.P. Moschetti, N.M. Shapiro, and Y. Yang, Processing seismic ambient noise data to obtain reliable broadband surface wave dispersion measurements, *Geophys. J. Int.*, 169, 1239-1260, doi: 10.1111/j.1365-246X.2007.03374.x, 2007.
- Bostock, M. G., Rondenay, S., Schragge, D.S., Multiparameter two-dimensional version of scattered teleseismic body waves, 1. Theory for oblique incidence: *J. Geophys. Res.*, 106, 30,771-30,782, 2001.
- Hogan, J.P., and Gilbert, M.C., Intrusive style of A-type sheet granites in a rift environment: The Southern Oklahoma aulacogen, in Ojakangas, R.W., et al., eds., Middle Proterozoic to Cambrian rifting, central North America, *Geological Society of America Special Paper 312*, p. 299311, doi: 10.1130/0-8137-2312-4.299, 1997.
- Kluth, C.F., Plate tectonics of the Ancestral Rocky Mountains, in Peterson, J.A., ed., Paleotectonics and sedimentation in the Rocky Mountain region, United States, *American Association of Petroleum Geologists Memoir 41*, p. 353369, 1986.
- Obrebski, M., Allen, R.M., Xue, M., Hung S.H., Slab-plume interaction beneath the Pacific Northwest, *Geophys. Res. Lett.* 37, L14305, doi:10.1029/2010GL043489, 2010.
- Obrebski, M., Allen, R.M., Pollitz, F.F., Hung, S.H., Lithosphere-asthenosphere interaction beneath the western United States from the joint inversion of body-wave traveltimes and surface-wave phase velocities, *Geophys. J. Int.* 185, 1003-1021, doi:10.1111/j.1365-246X.2011.04990.x, 2011.
- Pollitz, F.F. and Snoke, J.A., Rayleigh-wave phase-velocity maps and three-dimensional shear-velocity structure of the western US from local non-plane surface-wave tomography, *Geophys. J. Int.*, 180, 1153-1169, 2010.
- Porritt, R.W., Allen, R.M., Boyarko, D.C., Brudzinski, M.R., Investigation of Cascadia Segmentation with Ambient Noise Tomography, *Earth Planet. Sci. Lett.* 185, 67-76, doi:10.1016/j.epsl.2011.06.026, 2011
- Soreghan, G.S., Keller, G.R., Gilbert, M.C., Chase, C.G., Sweet, D.E., Load-induced subsidence of the Ancestral Rocky Mountains recorded by preservation of Permian landscapes, *Geosphere*, 10.1130/GES00681.1, 2012
- Xue, M. and R.M. Allen, Mantle Structure Beneath the Western US and its Implications for Convection Processes, *J. Geophys. Res.*, 115, B07303, doi:10.1029/2008JB006079, 2010

28 Trust but Verify: a spot check for the new stratified model of upper mantle anisotropy beneath North America

Huaiyu Yuan and Vadim Levin (Rutgers University)

28.1 Research Summary

A newly developed 3D model of radially and azimuthally isotropic shear wave velocity beneath the North American continent (Yuan *et al.*, 2011; referred to as YR11 hereafter) resolves a long-standing argument regarding the provenance of seismic anisotropy (e.g. Silver, 1996; Vinnik *et al.*, 1984) with directional dependency of wave speed placed into both the lithosphere and the asthenosphere. As YR11 shows, the anisotropy domain of the North American continent is strongly stratified; large amplitude anisotropy domains are observed in both lithosphere and asthenosphere, suggesting that contributions to the core-refracted shear wave SKS splitting come from both lithosphere and asthenosphere.

Due to the continent-wide coverage, the new model has lateral resolution on the scale of 500 km and is expected to average, and thus possibly misrepresent, the structure in regions with abrupt lateral changes in properties. One such region is the New England Appalachians, where rifting and paleo-ocean closure have significantly reworked the passive continent margin (e.g., Thomas, 2006). The local tomography studies suggest a thin lithosphere (~ 100 km) in the region (e.g., Li *et al.*, 2003). This view is also supported by the P and S receiver function (RF) studies (e.g., Abt *et al.*, 2010).

On the other hand, azimuthal anisotropy in this region in YR11 shows in general a two-layered upper mantle (Fig. 2.52): a thick upper layer (>150 km; with peak around 80 km) with the anisotropy direction at high angle to the plate motion (APM; Gripp and Gordon, 2002); and a deeper layer (>200 km) whose anisotropy direction appears APM parallel (Fig. 1). This two-layered fast axis direction pattern is consistent with one of the earliest cases for stratified anisotropy built on data from this part of North America (Levin *et al.*, 1999), however the lithosphere thickness inferred from the abrupt depth dependent anisotropy is thicker than other studies.

We conduct two-layer single station shear wave splitting modeling at station HRV, and anisotropy P-receiver function analysis at the stations. Compared to the long period surface waveform modeling, these techniques have complementary sensitivity to the upper mantle anisotropy structure, therefore can provide high-quality constraints on the vertical and lateral variation in attributes of anisotropy. We compare (and contrast) these constraints with structure predicted for this location by the YR11 model. Our goals are both to test the new model in one place, and to develop a strategy for such testing.

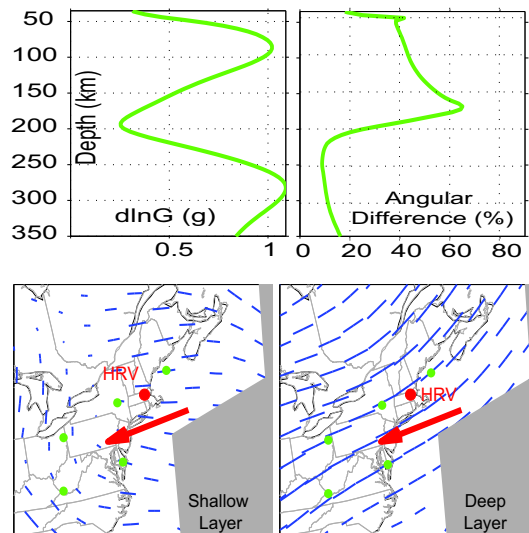


Figure 2.52: 1D azimuthal anisotropy strength (top left) and anisotropy angular difference with respect to the APM, averaged from model nodes (green dots) in the maps below, which shows the two-layer equivalent apparent fast axis directions (blue sticks) predicted from YR11 model: lithosphere, lower left; and asthenosphere, lower right. Red arrow shows the APM.

28.2 Results and Conclusions

We find ample evidence for sharp gradients in anisotropy within the upper mantle beneath northeastern North America. The depths where these gradients occur are consistent with the region of abrupt vertical change in anisotropic parameters of the new 3D model. Orientations of the symmetry axes suggested by polarity changes in receiver functions (Fig. 2.53) also agree with the model. Individual measurements of splitting in SKS phase from HRV vary with backazimuth, forming a characteristic $\pi/2$ pattern (Fig. 2.54) that is well represented by two layers of anisotropy. This result confirms Levin *et al.* (1999) results with vastly larger amount of data. We find it very gratifying that parameters of anisotropy within the layers generally agree with both the new model and the old study. Orientations of fast anisotropic axis at ~ 100 km depth suggested by the two methods are in good agreement as well: 100SE from SKS (Fig. 2.55) and 110-130 from RFs (Fig. 2.53).

We can thus infer that the fabric below ~ 100 km is indeed aligned with plate motion, and that the transition from this fabric to another is abrupt. This transition may indicate a shallow LAB in the region, as evidenced by the negative velocity gradient following the orogenic trends

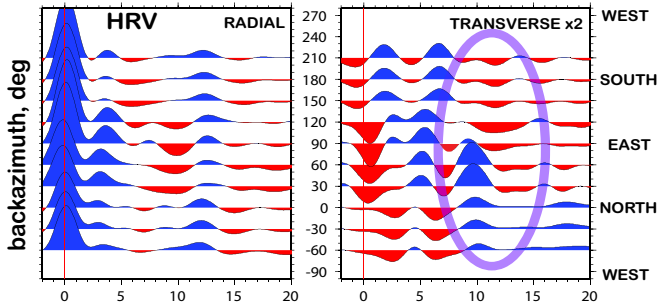


Figure 2.53: Receiver function azimuthal stacks at station HRV. Left radial component; right transverse component. Note change of polarity occurs around 10 sec (circled).

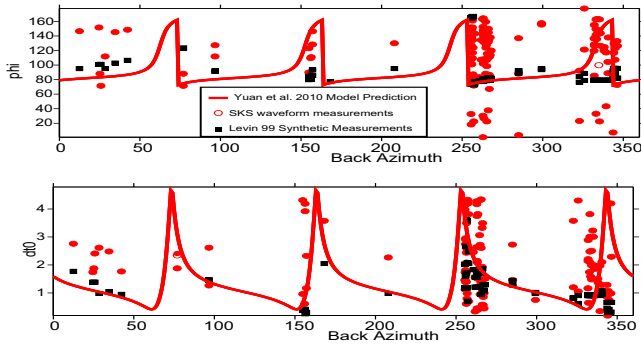


Figure 2.54: Model prediction (red curves, YR11) and data measurements for individual events, plotted against event back-azimuth. Measurements from *Levin et al.* (1999) model synthetic waveforms are plotted for comparison.

and the hotspot track shown in the updated shear-wave model of YR11 (Fig. 2.56).

28.3 Acknowledgements

We thank the IRIS DMC for providing the waveforms.

28.4 References

- Abt, D., Fischer, K., French, S., Ford, H., Yuan, H. & Romanowicz, B. North American lithospheric discontinuity structure imaged by Ps and Sp receiver functions, *J. Geophys. Res.*, 115, B09301, 2010.
- Gripp, A. & Gordon, R. Young tracks of hotspots and current plate velocities, *Geophys. J. Int.*, 150, 321-361, 2002.
- Levin, V., Henza, A., Park, J. & Rodgers, A. Texture of mantle lithosphere along the Dead Sea Rift: recently imposed or inherited?, *Phys. Earth Planet. Int.*, 247, 157-170, 2006.
- Li, A., Forsyth, D. & Fischer, K. Shear velocity structure and azimuthal anisotropy beneath eastern North America from Rayleigh wave inversion, *J. Geophys. Res.*, 108, 24 PP, 2003.
- Silver, P. Seismic anisotropy beneath the continents; probing the depths of geology, *Annu. Rev. Earth Planet. Sci.*, 24, 385-432, 1996.
- Thomas, W. Tectonic inheritance at a continental margin, *GSA Today*, 16, doi: 10.1130/1052-5173, 2006.
- Vinnik, L., Kosarev, G. & Makeyeva, L. Anisotropy of the lithosphere according to the observations of SKS and SKKS waves, *Dokl. Akad. Nauk SSSR*, 278, 1335, 1984.

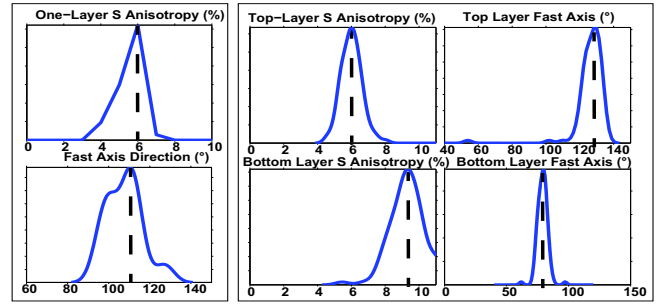


Figure 2.55: SKS 1-layer (left) and two-layer (right) modeling results. Plotted are probability density function of apparent fast axis (top) and slitting time (bottom) for each layer.

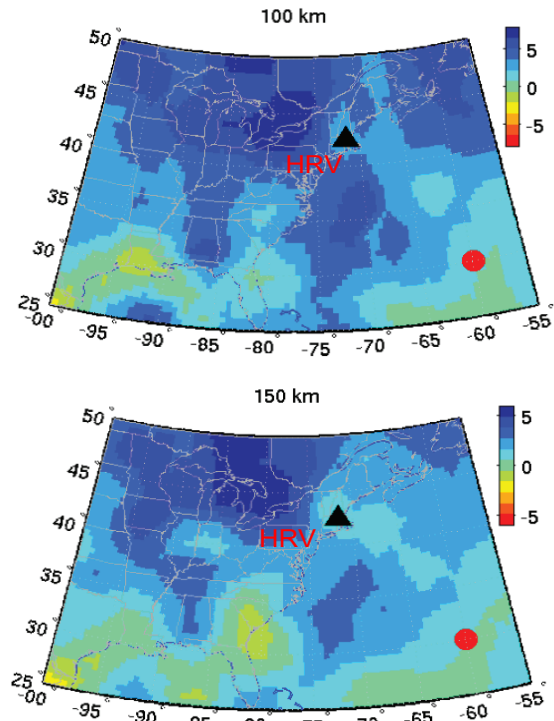


Figure 2.56: Model update of YR11, using ~200 local events and TA stations up to Oct. 2011. Note thinning of the lithosphere occurs near HRV. Red dot is Bermuda hotspot location.

Yuan, H., Romanowicz, B., Fischer, K. & Abt, D. 3-D shear wave radially and azimuthally anisotropic velocity model of the North American upper mantle, *Geophys. J. Int.*, 184, 1237-1260, 2011.

Yuan, H., Dueker, K. & Schutt, D. Testing five of the simplest upper mantle anisotropic velocity parameterizations using teleseismic S and SKS data from the Billings, Montana PASSCAL array., *J. Geophys. Res.*, 113, B03304, 03320 PP., 2008.

29 3-D Seismic Velocity Structure of the Hawaii Hotspot from Joint Inversion of Body Wave and Surface Wave Data

Cheng Cheng, Richard M Allen, Rob W Porritt

29.1 Introduction:

The Hawaii hotspot and the associated chain of islands have been long regarded as the case example of a deep-rooted mantle plume. However the efforts to detect a thermal plume seismically have been inconclusive. While the tomography model of *Wolfe et al.* (2009, 2011) suggests a lower mantle plume southeast of Hawaii, *Cao et al.* (2011) use scattering off the underside of the 660 km discontinuity to argue that the source of the hotspot is a broad region to the southwest. They image a broad down-warping of the 660 discontinuity that they interpret as being due to a hot region of the uppermost lower-mantle approximately 2000km wide. They suggest that the Hawaii volcanism is fed by small-scale convection in the upper mantle around the periphery of this broad lower-mantle feature.

Previous body wave tomography models may not be able to resolve between a continuous plume-like structure and separate anomalies at different depths resulting from small-scale mantle convection. In this study we combine the complementary sensitivities of body and surface-waves in order to improve resolution of mantle structure beneath Hawaii. The main limitation of body-wave tomography alone is the lack of resolution at shallow lithospheric depth where ray paths do not cross each other. By adding surface-wave constraints to the inversion as well, the resolution of the crustal and upper mantle structure is improved.

29.2 Data Processing:

We used data from the deployment of temporary broadband ocean-bottom seismometers (OBSs) of the Hawaiian Plume-Lithosphere Undersea Melt Experiment (PLUME), which was designed to determine mantle seismic velocity structure beneath the Hawaiian hotspot.

In a first step we oriented the PLUME OBS horizontal components using teleseismic P-wave particle motions. Generally we obtained stable and reliable orientations over a range of earthquake back-azimuths. Due to the high noise of the OBS data in some frequency bands we began by filtering in the period band of 0.04-1Hz. We measured ~ 1100 P-wave relative arrival times on the vertical component and ~ 750 S-wave relative arrival times (include direct S and SKS phases) on the SV component using multi-channel cross correlation. We use a total of ~ 70 events which are distributed in as wide a range of back azimuth directions as possible. We also use surface wave constraints and apply the two-plane wave tomog-

raphy method to invert for the phase velocity structure. This tomography method, which also considers the finite frequency effects, inverts the phase data and amplitude information simultaneously for the phase velocity at each point across the region in addition to incoming wavefield parameters. We use surface waves from 71 events with magnitude greater than 5.8 to generate phase velocity maps from 25 sec to 100 sec. These maps clearly show the low velocities beneath the islands surrounded by relatively high phase velocity.

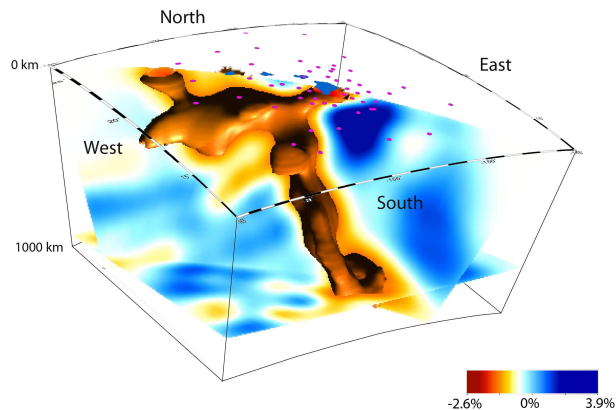


Figure 2.57: 3D view of our preliminary S-velocity model for the mantle beneath Hawaii. The location of the islands (blue) and the PLUME array (pink) are shown on the surface of the model volume.

29.3 Preliminary Results and Implications:

Figure 2.57 shows the S-velocity model derived from the body wave data. This shows the 3-D structure beneath the PLUME array to a depth of 1000km and reveals a several-hundred-kilometer-wide region of low velocities beneath Hawaii that dips to the southeast. The low velocities continue downward through the mantle transition zone and extend into the uppermost lower-mantle (although the resolution of lower mantle structure from this data set is limited). The independent P-wave images are generally consistent with S-wave structure. These images are consistent with the interpretation that the Hawaiian hotspot is the result of an upwelling high-temperature plume from the lower mantle. The broader upper-mantle low-velocity region immediately beneath the Hawaiian Is-

lands likely reflects the horizontal spreading of the plume material beneath the lithosphere.

We also obtain a preliminary result from the joint body-wave and surface-wave inversion (Figure 2.58). The same shallow low velocity zone is imaged along the island chain and the deeper part is identical to the body-wave inversion image. The low velocity to the southwest of the island is also clear to a depth of 600km as mentioned above. If the observation here is true, it will provide a hot environment for the 660km discontinuity to the west of the Hawaii and may give a new perspective to the plume origin debate.

29.4 References

Cao, Q. et al., Seismic Imaging of Transition Zone Discontinuities Suggests Hot Mantle West of Hawaii, *Science*, 332, 1068, 2011.

Obrebski, M., Allen, R. M., Xue, M., Hung, S-H., Slab-plume interaction beneath the Pacific Northwest, *Geophys. Res. Letters*, 37, 114305, 2010.

L. Cserepes, D. A. Yuen, On the possibility of a second kind of mantle plume. *Earth Planet. Sci. Lett.* 183, 61, 2000.

C. J. Wolfe et al., Mantle shear-wave velocity structure beneath the Hawaiian hot spot. *Science* 326, 1388, 2009.

C. J. Wolfe et al., Mantle P-wave velocity structure beneath the Hawaiian hotspot. *Earth Planet. Sci. Lett.* 303, 267, 2011.

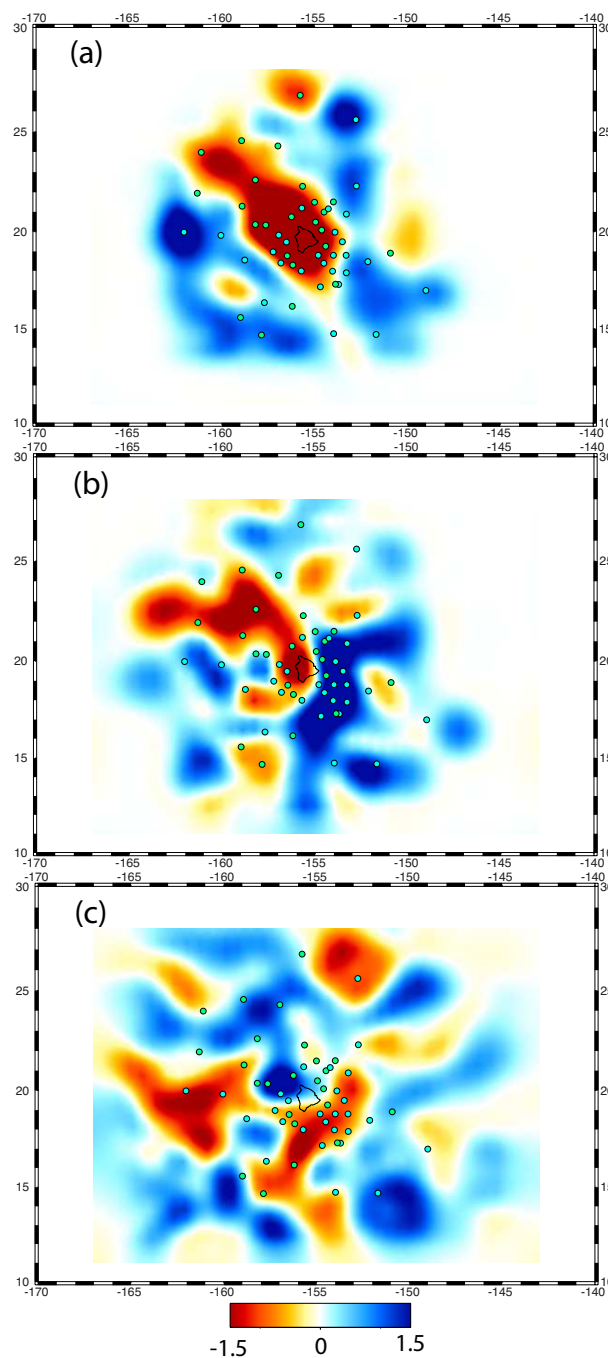


Figure 2.58: SV-velocity perturbation map around Hawaii at different depths using joint body- and surface-wave tomography. (a) 100 km (b) 300 km (c) 600 km depth

30 Azimuthal anisotropy in the Pacific upper mantle

Huaiyu Yuan and Barbara Romanowicz

30.1 Anisotropic Layering in North America

We recently developed a new three dimensional radially and azimuthally anisotropic model of the upper mantle in north America, using a combination of long-period 3-component surface and overtone waveforms, and SKS splitting measurements (*Yuan and Romanowicz, 2010*). We showed that: 1. azimuthal anisotropy is a powerful tool to detect layering in the upper mantle, revealing two domains in the cratonic lithosphere, separated by a sharp laterally varying boundary in the depth range 100-150 km, which seems to coincide with the mid-lithospheric boundary (MLD) found in receiver function studies; 2. contrary to receiver functions, azimuthal anisotropy also detects the lithosphere-asthenosphere boundary (LAB) as manifested by a change in the fast axis direction, which becomes quasi-parallel to the absolute plate motion below ~ 250 km depth; and 3. a zone of stronger azimuthal anisotropy is found below the LAB both in the western US (peaking at depths of 100-150km) and in the craton (peaking at a depth of about 300 km).

30.2 Going to the global inversion

Here we show preliminary attempts at expanding our approach to the global scale with the goal, in particular, of determining whether our results can be generalized to other continents and oceans. We started with our most recent global upper mantle radially anisotropic shear velocity model, determined using the Spectral Element Method (*French et al.*, in prep) and augmenting the corresponding global dataset of initially 200 events and 10,000 long period waveforms, in order to ensure optimal azimuthal coverage of the globe. Depth parameterization is chosen so as to resolve the kind of layering seen in north America. Our preliminary results, which do not yet incorporate SKS splitting measurements (see discussion below), look promising as they confirm the layering found in North America, using a different, global dataset and starting model (Fig. 2.59).

30.3 Robust SKS measurements

In *Romanowicz and Yuan (2012)*, we show that back-azimuthally averaged splitting does not depend on the order of layers in the model and is correctly predicted by the formalism of *Montagner et al. (2000)*, which forms the basis of our joint inversion of surface waveforms and SKS splitting data. Robust station average measurements is contingent upon a wide back-azimuthal coverage of the

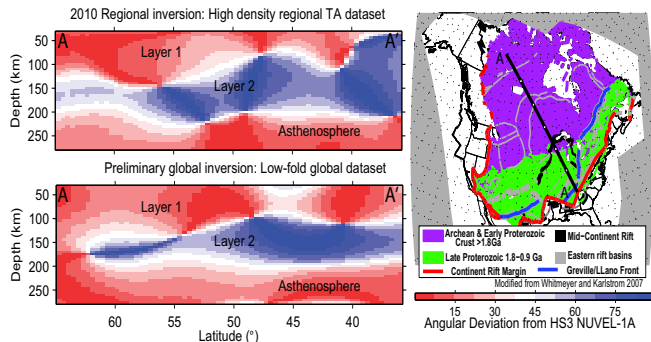


Figure 2.59: Two layered lithosphere in the North American craton shown by both the regional (top) and global (bottom) inversions. Color coded are anisotropy direction differences with respect to the HS3 NUVEL-1A absolute plate motion (APM; *Gripp and Gordon, 2002*). A promising three-layer anisotropy domain is observed, confirming the layering found in North America.

SKS events. A systematic evaluation of the global SKS datasets to obtain robust station averaged measurements is currently being performed, which is essential in recovering the deep azimuthal anisotropy at deep depth (*Yuan and Romanowicz, 2010*).

We therefore focus only the upper most mantle (< 250 km) of the Pacific region, where earthquakes from the Pacific ring of fire have given the region an optimal azimuthal coverage. The available SKS measurements are sparse in the region (e.g., *Becker et al., 2012*), which as we showed in our previous study in North America are needed in continents where the lithosphere is thick (~ 200 - 250 km). For the Pacific region, however, the oceanic lithosphere is relatively thin (e.g., *Rychert and Shearer, 2011; Schmerr, 2012*), thus the natural depth resolution of the surface waveforms allows us to look into both the lithosphere and asthenosphere and their interactions.

30.4 Pacific Layering

Anisotropy stratification of the Pacific upper mantle was reported in early azimuthal anisotropy studies (e.g., *Montagner, 2002; Smith et al., 2004; Maggi et al., 2006*). Our initial results (Fig. 2.60) show at shallow depths (70-100km) a domain of anisotropy with a general northward fast axis direction beneath the old (e.g. west of Hawaii > 80 Ma, *Muller et al. 2008*) portion of the plate. The direction is consistent with the paleo-pacific plate motion (e.g., *Muller et al., 2008*). Within this shallow domain an east-west direction, which seems to follow the fracture zones (e.g., *Smith et al., 2004*), is observed where the

plate is young.

Below 150 km depth, there is a deeper anisotropy domain whose fast axis direction is in good agreement with the current Pacific plate motion direction (HS3-NUVEL 1A; *Gripp and Gordon, 2002*). This deep anisotropy domain seems stronger in amplitude, and spatially correlates with the low velocity channel in the asthenosphere (e.g. *Montagner 2002*). Perturbations to the anisotropy domain are observed near the Hawaii hotspot and the Pacific/Eurasia subduction region.

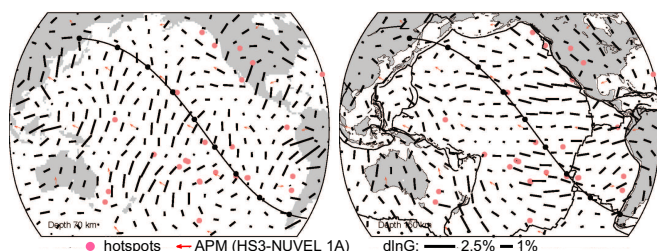


Figure 2.60: Two anisotropic domains in the Pacific Ocean. Azimuthal anisotropy direction and strength (shown as the black sticks) at 70- (left) and 150-km (right), respectively. The APM in HS3-NUVEL 1A model is illustrated in small red arrows. Ridges and hotspots are indicated.

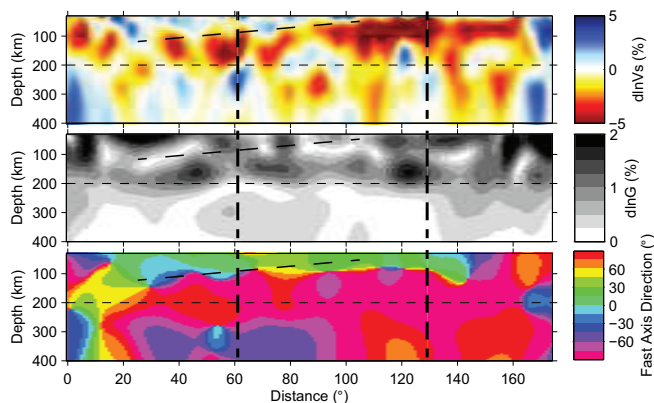


Figure 2.61: Depth cross-sections of isotropic Vs (top), azimuthal anisotropy strength G (middle) and fast axis directions (bottom). The location of the cross-section is shown in (Fig. 2.60). Black broken line indicates the bottom of the oceanic lithosphere inferred from Vs and G. Vertical dashed lines show the location of the Hawaii hotspot and the East Pacific Rise. The APM directions are in general NWW (light purple) in the Pacific.

The Vs depth cross-section from our group’s most recent global model (~300-km horizontal resolution; *French et al. in prep.*) shows age-progressive thickening of the high velocities away from the ridge (Fig. 2.61). Remarkably the boundary of the two anisotropy domains, corresponding to those discussed in (Fig. 2.60), also follows the age progressive pattern at similar depths. Clearly the paleo- or current APM parallel direction is

associated with each domain, respectively, a strong indication that the past and present time plate motions have been preserved in the upper mantle.

30.5 Summary

We expand our regional azimuthal anisotropy inversion to the global scale. With the current low data-fold waveforms, we are able to re-produce the layered lithospheric anisotropy pattern found in our previous studies. While robust SKS data are yet to be incorporated to address deep anisotropy in the cratonic upper mantle worldwide, promising results indicate that that the Pacific ocean upper mantle is also anisotropically layered, with depth dependent domains that record past and current plate motions.

30.6 Acknowledgements

This work was supported by NSF/EarthScope program grants EAR-0643060 and EAR-0738284.

30.7 References

Becker, T.W., Lebedev, S. and Long, M.D., 2012. On the relationship between azimuthal anisotropy from shear wave splitting and surface wave tomography, *J. Geophys. Res.*, 117, B01306.

Gripp, A.E. and Gordon, R.G., 2002. Young tracks of hotspots and current plate velocities, *Geophys. J. Int.*, 150, 321-361.

Lekic, V. and Romanowicz, B., 2011. Inferring upper-mantle structure by full waveform tomography with the spectral element method, *Geophys. J. Int.*, 185, 799-831.

Maggi, A., Debayle, E., Priestley, K. and Barruol, G., 2006. Azimuthal anisotropy of the Pacific region, *Earth Planet. Sci. Lett.*, 250, 53-71.

Montagner, J.-P., Griot-Pommerer, D.-A. and Lave, J., 2000. How to relate body wave and surface wave anisotropy?, *J. Geophys. Res.*, 105, 19,015-019,027.

Montagner, J.P., 2002. Upper mantle low anisotropy channels below the Pacific Plate, *Earth Planet. Sci. Lett.*, 202, 263-274.

Muller, R.D., Sdrolias, M., Gaina, C. and Roest, W.R., 2008. Age, spreading rates, and spreading asymmetry of the world’s ocean crust, *Geochem. Geophys. Geosyst.*, 9, Q04006.

Romanowicz, B. and Yuan, H., 2012. On the interpretation of SKS splitting measurements in the presence of several layers of anisotropy, *Geophys. J. Int.*, 188, 1129-1140.

Rychert, C.A. and Shearer, P.M., 2011. Imaging the lithosphere-asthenosphere boundary beneath the Pacific using SS waveform modeling, *J. Geophys. Res.*, 116, B07307.

Schmerr, N., 2012. The Gutenberg Discontinuity: Melt at the Lithosphere-Asthenosphere Boundary, *Science*, 335, 1480-1483.

Smith, D.B., Ritzwoller, M.H. and Shapiro, N.M., 2004. Stratification of anisotropy in the Pacific upper mantle, *J. Geophys. Res.*, 109, B11309.

Yuan, H. and Romanowicz, B., 2010. Lithospheric layering in the North American craton, *Nature*, 466, 1063-1068.

31 Anisotropic Upper Mantle Shear-wave Structure of East Asia from Waveform Inversion

Jiajun Chong, Huaiyu Yuan, Scott French, Barbara Romanowicz, and Sidao Ni (KLDG)

31.1 Introduction

East Asia is a region that is seismically active and is surrounded by active tectonic belts, such as the Himalaya collision zone, western Pacific subduction zones and the Tianshan-Baikal tectonic belt. Seismic anisotropic tomography can shed light on the complex crust and upper mantle dynamics of this region, which is the subject of much debate. In this study, we applied time domain full waveform tomography to image the 3D isotropic and anisotropic upper mantle shear velocity structure of East Asia. We present preliminary modeling results of the first iteration and discuss their tectonic implications.

31.2 Data and Inversion

Three component waveforms of teleseismic and far regional events ($15^\circ \leq \Delta \leq 165^\circ$) with magnitude ranges from M_w 6.0 to M_w 7.0 and source duration time less than 10 sec are collected from 133 permanent and 563 temporary broadband seismic stations in East Asia. Wave-packets of both fundamental and overtone modes, filtered between 60 and 400 sec, are picked automatically according to the similarity between data and synthetic waveforms, and later checked manually to get high quality data. Wavepackets corresponding to event-station paths that sample the region considered are weighted according to path redundancy and signal to noise ratio. These waveforms (1467 events) together with the dataset used for the global tomography (*Lekic and Romanowicz, 2011*) provide us with good density and azimuthal coverage in the target region.

The model is laterally parameterized with spherical splines and vertically in terms of cubic splines. We correct waveforms for the effects of 3D structure outside of the region with a starting global anisotropic upper mantle shear velocity model based on waveform inversion using the Spectral Element Method (*Lekic and Romanowicz, 2011*), updated for more realistic crustal thickness (*French et al., 2011*). We also invert for the 3D structure of the target region using normal mode non-linear asymptotic coupling theory (*NACT, Li and Romanowicz, 1995*).

31.3 Preliminary Result

After one iteration, the isotropic (V_s) and radial anisotropic ($\xi = (V_{sh}/V_{sv})^2$) model in the target region is updated to a spherical spline level of 6 and 5, equivalent to a spherical harmonic of about degree 92 and 46 for V_s and ξ , respectively. The following 2D maps

show the perturbations of V_s (Figure 2.62) with respect to the new 1D average model of the target region and the radial anisotropic structure (Figure 2.63) at a depth of 150 km. The map view of V_s perturbation with respect to the 1D regional mean velocity model shows dominant fast (west) and slow (east) velocity domains separated by Altai-Qilian orogenic belts. The anisotropic structure generally agrees well with the tectonics in target region.

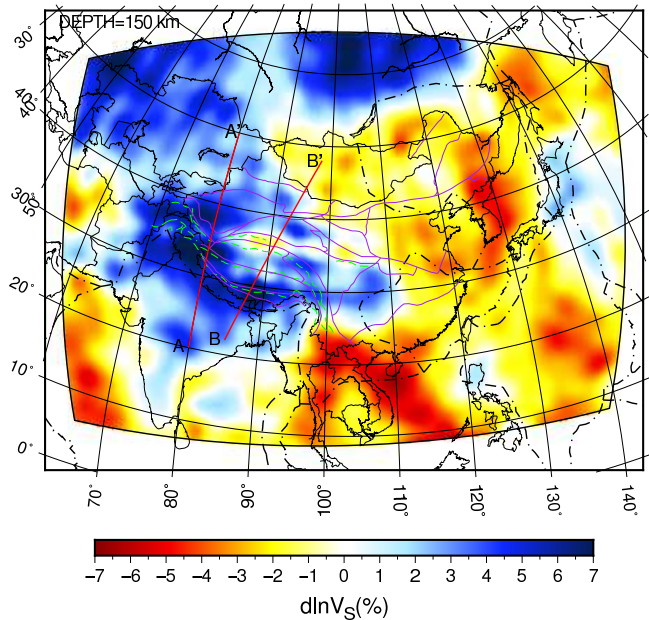


Figure 2.62: Map view of V_s perturbation at a depth of 150 km. It shows dominant fast (west) and slow (east) velocity domains separated by Altai/Qilian orogenic belts. Red lines are the location of depth cross-sections in Figure 2.64 and Figure 2.65. Purple lines are the boundaries of major tectonic blocks, and black dashed lines mark the plate boundaries.

Depth cross-sections in the Tibet region, as shown in Figure 2.64 and Figure 2.65, indicate that the Indian plate may have subducted northward beneath Tibet with different dipping angles and north reach in the western (Figure 2.64) and eastern part (Figure 2.65) of Tibet. A high velocity anomaly has been found beneath east Tibet which may be the subducted Asian lithosphere. We also found that strong low velocity structure extends down to 100+ km in the central and north regions of Tibet, which also has been found in early studies (*Brandon and Romanowicz, 1986, Bourjot and Romanowicz, 1992*).

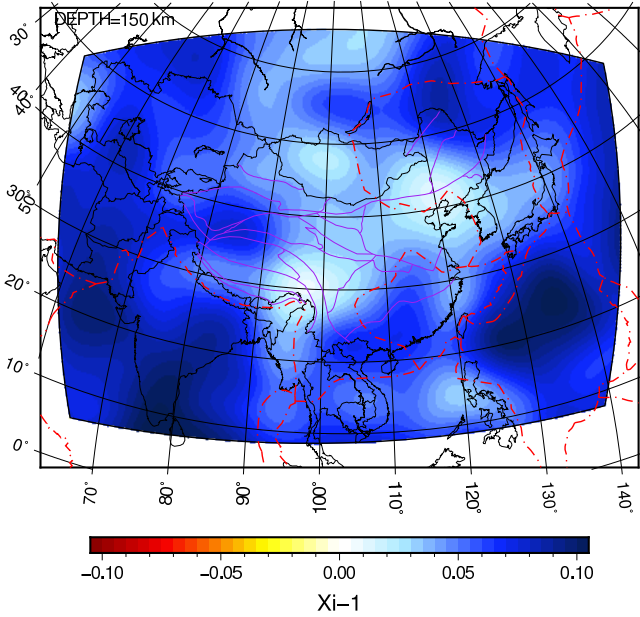


Figure 2.63: Map view of anisotropic structure ($\xi - 1$) at a depth of 150 km.

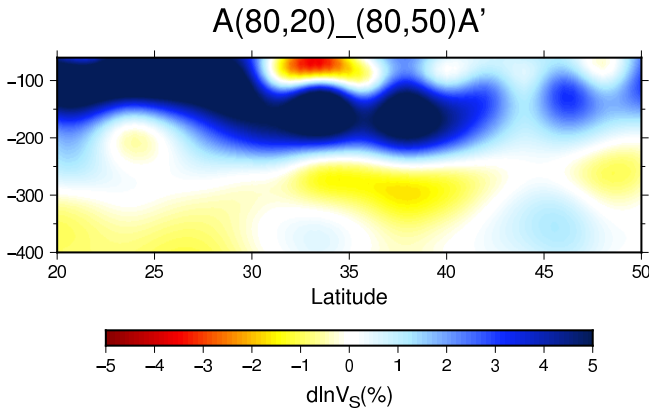


Figure 2.64: Depth cross-section along AA' in Figure 2.62, shows that the Indian plate has reached the south boundary of the Tarim Block around 35° north with a relatively large dipping angle.

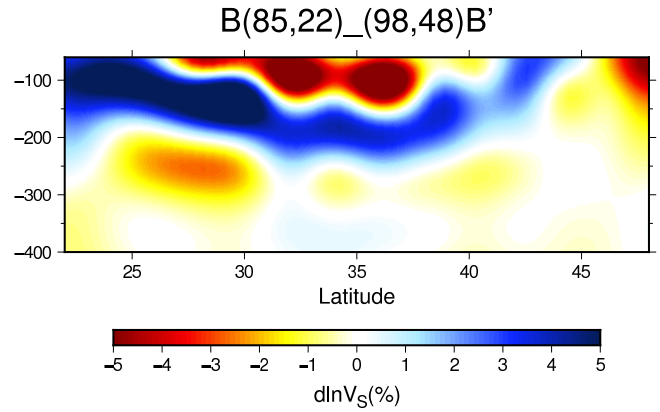


Figure 2.65: Depth cross-section along BB' in Figure 2.62, shows that the Indian plate may have reached the Bangong-Nujiang suture around 32° north. The Asian lithosphere may also have subducted southward beneath Tibet.

31.4 Conclusions

We present a preliminary anisotropic upper mantle model of East Asia based on time domain waveform inversion. Our model shows some features that agree well with tectonics in the target region and some structures that haven't been imaged before. We plan to do more iterations to improve the waveform fit and resolution. We will also combine waveform inversion with SKS splitting data to invert for azimuthal anisotropy, as in *Yuan and Romanowicz, (2010)* for North America.

31.5 Acknowledgements

This work was supported by NSF grant EAR 0738284.

31.6 References

- V. Lekic, and B. Romanowicz, Inferring upper mantle structure by full waveform tomography with the Spectral Element Method, *Geophys. J. Int.*, 2011.
- X.D. Li, and B. Romanowicz, Comparison of global waveform inversions with and without considering cross-branch modal coupling, *Geophys. J. Int.*, 1995.
- Brandon and Romanowicz, A "NO-LID" zone in the central Chang-Tang platform of Tibet: evidence from pure path phase velocity measurements of long period Rayleigh waves, *JGR.*, 1986
- Bourjot and Romanowicz, Crust and upper mantle tomography in Tibet using surface waves, *GRL.*, 1992
- H. Yuan and B. Romanowicz, Lithospheric layering in the North American craton, *Nature*, 2010

32 An Exceptionally Large ULVZ at the Base of the Mantle near Hawaii

Sanne Cottaar and Barbara Romanowicz

32.1 Introduction

The lowermost lower mantle, also called the D", is a thermo-chemical boundary layer, presenting many intriguing observations. Global shear velocity tomography of shear velocities show strong degrees 2 and 3, dominated by two large low shear velocity provinces (LLSVP); one under Africa and one under the Pacific. Local studies on smaller scales show the occurrence of thin (tens of kilometers), intermittent ultra-low velocity zones (ULVZ). In this study we forward model the location, geometry and velocity reduction of one such ULVZ beneath the central Pacific on the basis of striking waveform complexities in shear (diffracted) phases.

32.2 Data and observations

The striking complexities appear in North American seismic data from events in the New Ireland Region, Papua-New Guinea. In particular, we model a 2010 event that has significant energy towards North America and good coverage thanks to the USArray Transportable Array. A nearby event in 2003 has less dense coverage (*To et al.*, 2011), but offers extended coverage from the Nars-Baja array to the south. The main observation is the occurrence of a postcursor in the period band 10-30 seconds. The postcursor is delayed by more than 30 seconds compared to the main phase with a move-out as a function of azimuth up to 50 seconds. Beamforming analysis on these delayed phases shows they are originating in a localized area in the lowermost lower mantle.

Additional azimuthal coverage comes from S/ScS phases from Fiji events to stations in Alaska. The observed delayed ScS phases (~15 seconds) help further constrain the uncertainty in location.

32.3 Forward modeling results

Synthetic data are forward modeled using a sandwiched version of CSEM (Coupled Spectral Element Method, *Capdeville et al.*, 2003). This method is computationally effective by only solving for the full 3D model, in the lowermost part of the mantle and coupling to a normal mode solution for a 1D model in the rest of the Earth.

Based on the beamforming and ray-theoretical analysis of the travel time results, we consider a simplified cylindrical shape for the ULVZ (see Figure 2.66). Our final model has a width of ~900 km and a height of ~20 km, thus having a large width:height aspect ratio. The velocity reduction is ~20% and the cylinder is centered

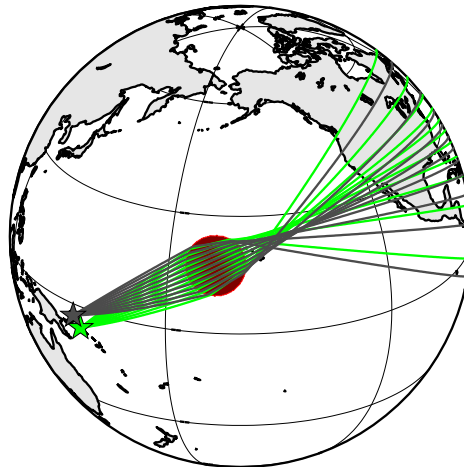


Figure 2.66: Ray-theoretical interpretation of the lens-like behavior of the ULVZ creating the postcursors. The 2010 event is shown in dark gray and the 2003 event in light gray. The dark circle indicates the location of the base of the final model.

roughly 11 degrees to the southwest of Hawaii. Figure 2.67 shows synthetic traces with and without a ULVZ alongside observations of the 2010 event. The different parameters have different uncertainties and trade-offs.

Height: The height of the ULVZ is fairly well constrained by the frequency dependence of the observations. Only periods below 30 seconds appear sensitive to this structure, while no postcursors are seen at longer periods. Similar frequency dependence can be seen in synthetics for models with heights between 15 and 25 km.

Width and velocity reduction: Clearly there is a trade-off in the size and the strength of the velocity reduction. However, when the ULVZ is too localized, the postcursors become smaller in amplitude. At the other end, when the ULVZ is large and weak, the move-out of the postcursor changes. Taking into account these constraints, error margins still remain on the order of 100 km in width and several percent in velocity reduction.

Location: Core-diffracted phases have a path-integrated sensitivity similar to that of surface waves. This creates an anisotropic uncertainty in location when modeling one event. Orthogonal to the direction of propagation, the location is well-constrained (as the postcursor move-out with azimuths would shift when shifting

the model). Along path the uncertainty in location is large. Combining the events for the New Ireland Region with the complexities seen in traces from a Fiji event towards Alaska further constrained the location to be SW of Hawaii. Uncertainties in latitude and longitude are on the order of several degrees.

32.4 Discussion

This data set has allowed us to map the full, though simplified, geometry of a ULVZ. The modeled ULVZ is much wider than ULVZs previously were thought to be (on the order of > 100 km). The location of this ULVZ is close to the northern boundary of the Pacific LLSVP. ULVZs have been modeled as chemically-distinct ridge-like features that are swept up at the LLSVP boundaries (McNamara *et al.*, 2010). In our modeling, our best model is cylindrical, but uncertainty on the precise shape remains. Furthermore, it is tempting to speculate on the relationship of the unusually large ULVZ and the close vertical proximity with the hotspot with the largest plume flux (Jellinek and Manga, 2004). Possibly the ULVZ could lie at the base of a whole mantle plume, and entrainment off the ULVZ could be the source of the dichotomy in geochemical isotope measurements in lavas on Hawaii (Weis *et al.*, 2011). The exact relationships between ULVZs, LLSVPs and hotspots remain elusive, but this new class of structures needs to be accounted for in geodynamical and mineral physical studies of the deep mantle.

32.5 Acknowledgements

We thank Akiko To for helpful discussions. This work is supported by NSF/CSEDI grant 067513.

32.6 References

Capdeville, Y., B. Romanowicz, and A. To, Coupling spectral elements and modes in a spherical earth: an extension to the sandwich case, *Geophys. J. Int.*, 154, 44-57, 2003

Jellinek, M. and M. Manga, Links between long-lived hot spots, mantle plumes, D" and plate tectonics. *Rev. of Geophys.*, 42, RG3002, 2004

Mégnin, C. and B. Romanowicz, The three-dimensional shear velocity structure of the mantle from the inversion of body, surface and higher-mode waveforms, *Geophys. J. Int.*, 143, 709-728, 2000

McNamara, A., E. Garnero and S. Rost, Tracking deep mantle reservoirs with ultra-low velocity zones. *Earth Plan. Sci. Lett.*, 299, 1-9, 2010

To, A., Fukao, Y., Tsuboi, SI, Evidence for a thick and localized ultra low shear velocity zone at the base of the mantle beneath the central Pacific, *Earth Plan. Sci. Lett.*, 184, 119-133, 2011

Weis, D., M. Garcia, J. Rhodes, M. Jellinek and J. Scoates, Role of the deep mantle in generating the compositional asymmetry of the Hawaiian mantle plume. *Nature*, 4, 831-833, 2011

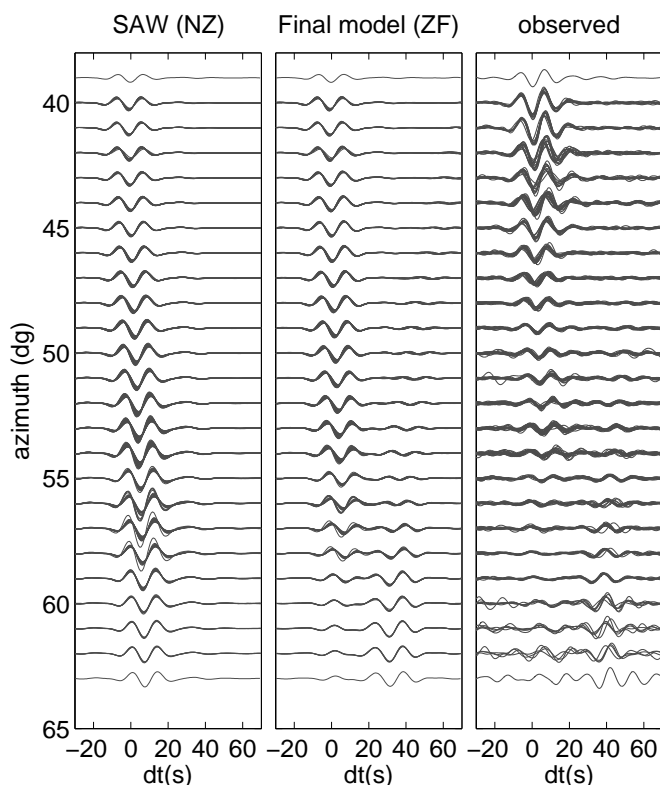


Figure 2.67: *Panel one:* 3D synthetics for shear diffracted phases of the 2010 event. Background model is SAW24B16 (Mégnin and Romanowicz, 2000). Panel shows 316 traces in one-degree azimuth bins. Traces are filtered between 10 and 20s. *Panel 2:* Same data set, but with the preferred cylindrical ULVZ included in the model. *Panel 3:* Observed data, filtered by the same frequency band.

33 Do "double SS precursors" mean double discontinuities?

Zhao Zheng and Barbara Romanowicz

33.1 Introduction

SS precursors are the underside reflections from the upper mantle discontinuities such as those at 410 and 660 km. They are important tools for studying the existence and characteristics of mantle discontinuities both on the global and regional scales (see *Deuss, 2009* for a review). Due to their sensitivity at the midpoint between source and receiver, coverage for oceanic regions is achieved where other methods such as receiver functions and triplications are not feasible. Their amplitudes are generally small (5-10% of the main phase), at or below noise level. Stacking is therefore necessary. Midpoint stacking over geographical bins with radius of 10° has been common. Recently, the deployment of the US Transportable Array (TA) allows unprecedented density of ray coverage and brings new opportunities to try and resolve finer scale discontinuity characteristics for much broader regions.

33.2 Double SS precursors

Here we present observations of SS precursors from an m_b 6.7, depth 38 km earthquake in 2010 recorded at TA (Fig. 2.68). The magnitude is optimal in that the precursor signals are strong, while the source time function is simple. A shallow depth prevents precursor interference. The epicentral distances fall in the range 120 - 150° , which is very suitable for an SS precursor study. We look at the transverse component displacement seismograms filtered in 20-100 seconds. In this particular case, the S660S precursors are strong enough to be identified on individual seismograms across the array without any stacking (Fig. 2.69a). Two signals around the theoretical S660S arrival time can be tracked coherently across the profile. In conventional interpretation, this would imply two discontinuity reflectors in the bounce point region. Vespagram analysis confirms that both signals have a slowness close to the theoretical value for S660S.

We attempt to fit the observations with 1D and 3D modeling. The 1D model is PREM (Dziewonski and An-

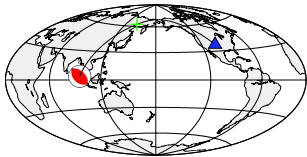


Figure 2.68: SS ray path from the event to TA (triangle). The cross denotes bounce point.

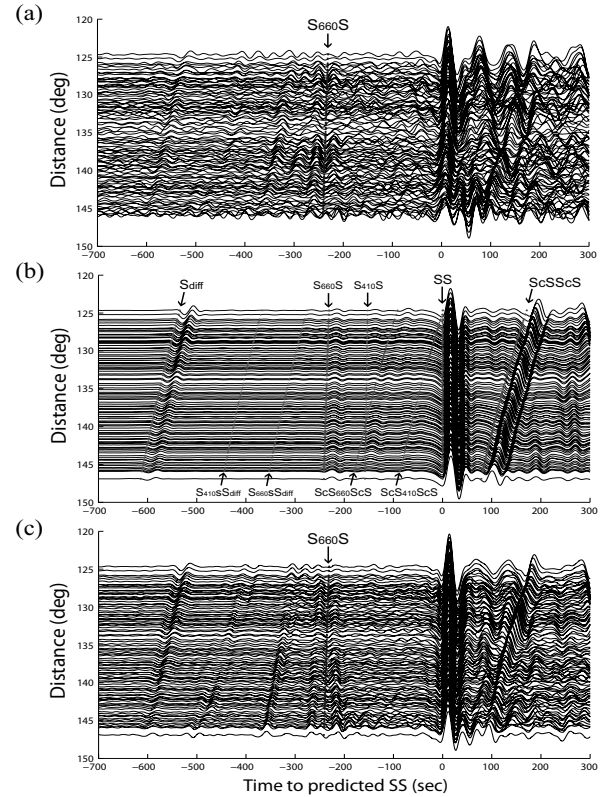


Figure 2.69: Transverse component record sections of (a) observed waveforms, (b) 1D synthetics and (c) 3D synthetics for stations in the azimuth range of 20 - 23° , aligned on the theoretical arrivals of the main phase SS. Major seismic phases and their associated precursors are marked by dotted lines on the 1D synthetics, for reference.

derson, 1981). For the 3D, a global tomographic shear velocity model S362ANI (*Kustowski et al., 2008*) is used with CRUST2.0 (*Bassin et al., 2000*); the Spectral Element Method (*Komatitsch and Tromp, 2002a,b*) is employed for simulation. As Fig. 2.69 shows, while only one S660S is present on the 1D synthetics as expected, "double precursors" are seen on 3D synthetics with correct slownesses, although only one 660-discontinuity is present in the model, which is intriguing.

33.3 The result of double discontinuities?

Next we try to pinpoint the structure that is responsible for the "double precursors" seen on the 3D synthetics. We first consider a modified 3D model in which only the

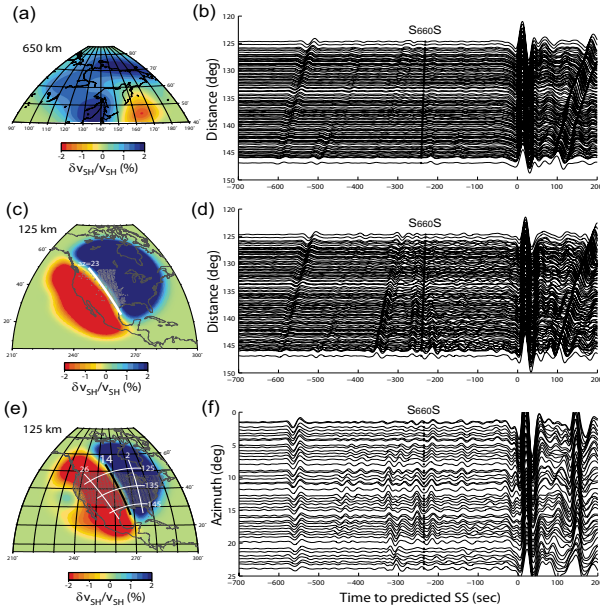


Figure 2.70: 3D models (left panels) and corresponding synthetics (right panels). Top: A model with bounce point 3D structure only. Middle: A model with receiver-side structure only. Dots denote TA stations. Bottom: A modified receiver-side model, in which the velocity boundary is shifted eastward. An expanded set of virtual receivers (dots) is used. The lines indicate equi-azimuth and equi-distance curves. (For color figure, see http://earthquakes.berkeley.edu/annual_report/)

heterogeneities in the bounce point region are preserved (Fig. 2.70a). To our surprise, the "double precursor" phenomenon disappears (Fig. 2.70b). We then try a model with receiver side 3D structure only (Fig. 2.70c). The corresponding synthetics (Fig. 2.70d) turns out to be capable of reproducing the "double precursors". In this velocity model, a sharp contrast between the fast craton east of the Rocky Mountain Front and the slower western US is present in the North American upper mantle, a prominent feature also seen in numerous continental scale tomography studies (e.g. *van der Lee and Frederiksen, 2005; Marone et al., 2007; Nettles and Dziewonski, 2008; Yuan et al., 2011*). This boundary is sub-parallel to the great circle paths for the event studied here, leading to a conjecture that the apparent "double precursors" are in fact artifacts due to scattering at the boundary.

In order to test this conjecture, we construct another model (Fig. 2.70e) in which the boundary is significantly shifted eastwards while its orientation still tracks the great circle ray path direction. We also expand the array of virtual receivers to the entire US in order to cover a broad range of azimuths across the boundary. The corresponding synthetics (Fig. 2.70f) are arranged by increasing azimuth (from east to west roughly). It is seen that for receivers far away from the boundary there is only one precursor (the later one); whereas the other wiggle (the

earlier one) picks up as receivers approach the boundary (azimuth $\sim 14^\circ$), thus confirming the conjecture. Further analysis of particle motions and comparison of transverse and radial component waveforms reveal the "precursors" are radial energy leaking to transverse component due to scattering (*Zheng and Romanowicz, 2012*).

33.4 Conclusions

We find that apparent SS precursors may not necessarily reflect the characteristics of mantle discontinuities in the bounce point region, as often assumed by conventional precursor travel time studies. Heterogeneities away from the bounce point region are able to generate artificial "precursors" in a coherent and therefore misleading way. This raises a caution for identifying and interpreting SS (and PP) precursors. As much as the USArray provides hope for improving resolution of precursor studies, care must be taken.

33.5 Acknowledgements

This work was supported by NSF EAR grant #0738284. We thank Scott French for help to compute SEM synthetics.

33.6 References

- Bassin, C., G. Laske and G. Masters, The current limits of resolution for surface wave tomography in North America, *EOS, Trans. Am. Geophys. Un.*, **F897**, 81, 2000.
- Deuss, A., Global observations of mantle discontinuities using SS and PP precursors, *Surv. Geophys.*, **30**, 301-326, 2005.
- Dziewonski, A. and D. Anderson, Preliminary reference Earth model, *Phys. Earth Planet. Inter.*, **25**, 297-356, 1981.
- Kustowski, B., G. Ekstrom and A. Dziewonski, Anisotropic shear-wave velocity structure of the Earth's mantle: a global model, *J. Geophys. Res.*, **113**, 2008.
- Komatitsch, D. and Tromp, J., Spectral-element simulations of global seismic wave propagation-I. Validation, *Geophys. J. Int.*, **149**, 390-412, 2002a.
- Komatitsch, D. and Tromp, J., Spectral-element simulations of global seismic wave propagation-II. Three-dimensional models, oceans, rotation and self-gravitation, *Geophys. J. Int.*, **150**, 303-318, 2002b.
- Marone, F., Gung, Y. and Romanowicz, B., Three-dimensional radial anisotropic structure of the North American upper mantle from inversion of surface waveform data, *Geophys. J. Int.*, **171**, 206-222, 2007.
- Nettles, M., and Dziewonski, A.M., Radially anisotropic shear velocity structure of the upper mantle globally and beneath North America, *J. Geophys. Res.*, **113**, B02303, 2008.
- Van der Lee, S. and Frederiksen, A., SurfaceWave Tomography applied to the North American Upper Mantle, in *Seismic Earth: Array Analysis of Broadband Seismograms*, eds Nolet, G. and Levander, A., pp. 67-80, Geophysical Monograph Series 157, American Geophysical Union, 2005.
- Yuan, H., Romanowicz, B., Fischer, K. M. and Abt, D., 3-D shear wave radially and azimuthally anisotropic velocity model of the North American upper mantle, *Geophys. J. Int.*, **184**, 1237-1260, 2011.
- Zheng, Z. and Romanowicz, B., Do "double SS precursors" mean double discontinuities?, *Geophys. J. Int.* (submitted), 2012.

34 Inversion of Receiver Functions without Deconvolution

Thomas Bodin, Huaiyu Yuan, Barbara Romanowicz

34.1 Introduction

The coda of teleseismic P-waves contains a large number of phases generated at interfaces beneath the receiver that contain a significant amount of information on seismic structure. However, these phases are buried in microseismic noise, and convolved with the source time function (Figure 2.71). Hence, the vertical $\mathbf{V}(t)$ and horizontal (radial) $\mathbf{H}(t)$ components of a seismogram for a P plane wave can be written as:

$$\mathbf{V}(t) = \mathbf{s}(t) * \mathbf{v}(t) * \mathbf{I}(t) \quad (2.3)$$

$$\mathbf{H}(t) = \mathbf{s}(t) * \mathbf{h}(t) * \mathbf{I}(t) \quad (2.4)$$

Where $s(t)$ is the source time function, $\mathbf{v}(t)$ and $\mathbf{h}(t)$ are the vertical and radial impulse response function of the near receiver structure, and $\mathbf{I}(t)$ is the instrument response.

The problem of isolating the structure effect is overcome by a method developed in the 1970's now widely used in seismology. The idea is to deconvolve the vertical component from the horizontal components to produce a time series called a 'receiver function' (RF) (Vinnik, 1977):

$$\mathbf{R}_{obs}(t) = \frac{\mathbf{H}(t)}{\mathbf{V}(t)} * \mathbf{G}(t) = \frac{\mathbf{h}(t)}{\mathbf{v}(t)} * \mathbf{G}(t) \quad (2.5)$$

where the fraction refers to a deconvolution (or spectral division). Note that the Receiver function is smoothed with a Gaussian filter $\mathbf{G}(t)$ in order to eliminate high frequency errors introduced during the deconvolution (see Figure 2.72). The smoothed receiver function waveform can be directly interpreted by visual inspection, or inverted in the time domain for a S-wave velocity model of the crust and uppermost mantle beneath the receiver.

Although inversion of RFs has been extensively used for the last 30 years, there are two well known drawbacks: 1) The deconvolution is an unstable numerical procedure that needs to be damped. This results in a loss of resolution and introduces errors in the receiver function, with a trade-off between the two effects as shown in Figure 2.71. 2) It is difficult to estimate the nature and level of uncertainties in the observed receiver function. That is, there is no clear way to theoretically propagate the noise present in different components of the seismogram into errors in the deconvolved waveform (Di Bona et al, 1998). Following ideas of Menke and Levin (2003), here we present a novel approach that avoids deconvolution, and hence directly overcomes these two problems.

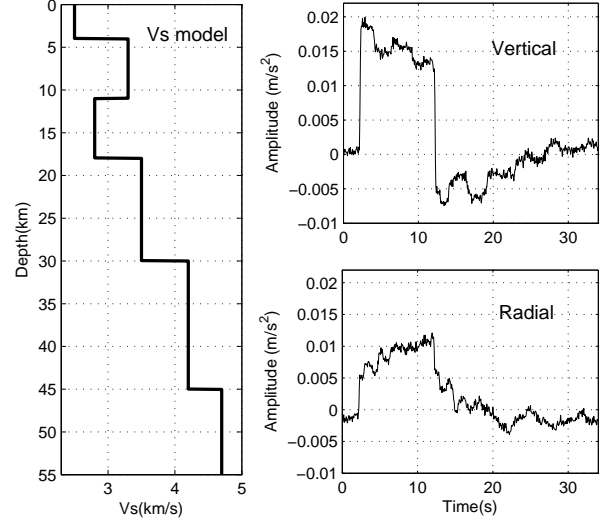


Figure 2.71: Synthetic seismograms computed for an incident plane P-wave traversing layered Earth model. The source time function is a box car function and some white Gaussian noise has been added with standard deviation of 2% the maximum amplitude.

34.2 A Cross-convolution Misfit Function

We use the cross-convolution misfit function that was proposed by Menke and Levin (2003) for inversion of SKS splitting measurements. If $\mathbf{v}_p(t, \mathbf{m})$, and $\mathbf{h}_p(t, \mathbf{m})$ are predicted structure response functions for a given model \mathbf{m} , we can convolve equation (1) by $\mathbf{h}_p(t, \mathbf{m})$, and (2) by $\mathbf{v}_p(t, \mathbf{m})$:

$$\mathbf{h}_p(t, \mathbf{m}) * \mathbf{V}(t) = \mathbf{s}(t) * \mathbf{v}(t) * \mathbf{I}(t) * \mathbf{h}_p(t, \mathbf{m}) \quad (2.6)$$

$$\mathbf{v}_p(t, \mathbf{m}) * \mathbf{H}(t) = \mathbf{s}(t) * \mathbf{h}(t) * \mathbf{I}(t) * \mathbf{v}_p(t, \mathbf{m}) \quad (2.7)$$

The misfit function is then defined as the difference between the left sides of (2.6) and (2.7).

$$\Phi(\mathbf{m}) = \|\mathbf{v}_p(t, \mathbf{m}) * \mathbf{H}(t) - \mathbf{h}_p(t, \mathbf{m}) * \mathbf{V}(t)\|^2 \quad (2.8)$$

which minimizes when $\mathbf{v}_p(t, \mathbf{m}) = \mathbf{v}(t)$ and $\mathbf{h}_p(t, \mathbf{m}) = \mathbf{h}(t)$.

This misfit function is equivalent to the distance between the observed and predicted receiver functions. However, 1) it does not require any deconvolution procedure, no damping parameter needs to be chosen, and hence no processing errors are introduced; 2) The chi-squared χ^2 (or log-likelihood) probability density function can be easily derived from errors statistics in seismograms $\mathbf{V}(t)$, and $\mathbf{H}(t)$.

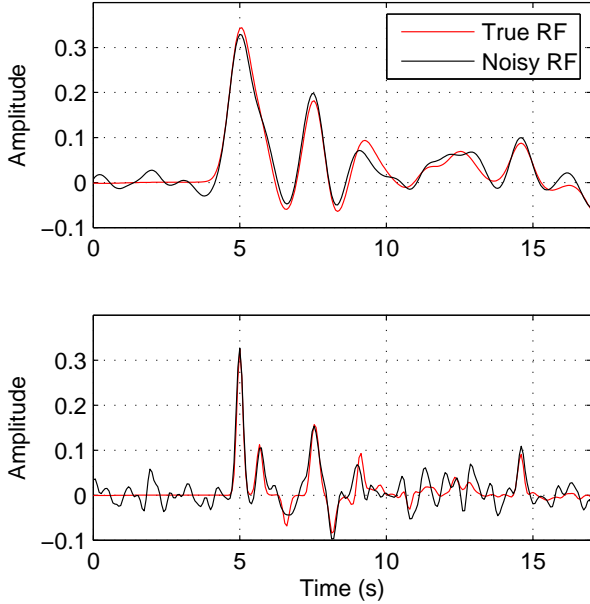


Figure 2.72: Receiver functions computed from seismograms in Figure 2.71 for two Gaussian filters compared with "true" receiver functions. This illustrates the trade-off between resolution and variance. Smoothing the waveform stabilizes the deconvolution at the cost of losing resolution. There is no mathematical model for the noise introduced by deconvolution.

Since discrete convolution in time is a simple summation, and since seismograms can be seen as corrupted by random errors, each sample of the signal obtained after discrete convolution is then a sum of random variables, whose statistics are straightforward to calculate with algebra of random variables. This is not the case with deconvolution schemes.

For example, let us assume as shown in Figure 2.71 a simple case where $\mathbf{V}(t)$, and $\mathbf{H}(t)$ contain independent, and normally distributed random errors (i.e. Gaussian white noise) with standard deviation σ . It can be easily shown that the chi-squared statistic for the misfit function Φ is:

$$\chi^2 = \frac{\Phi}{\sigma^2 (\sum_{i=1}^n (\mathbf{h}_p^i)^2 + \sum_{i=1}^n (\mathbf{v}_p^i)^2)} \quad (2.9)$$

where n is the number of samples in the signal.

34.3 Bayesian Inversion

A correct mathematical form for the chi squared distribution allows us to write the likelihood function which measures the probability that the predicted and observed data are consistent given a mathematical model for the random noise distribution. While error statistics in the data and in the misfit function are not indispensable in

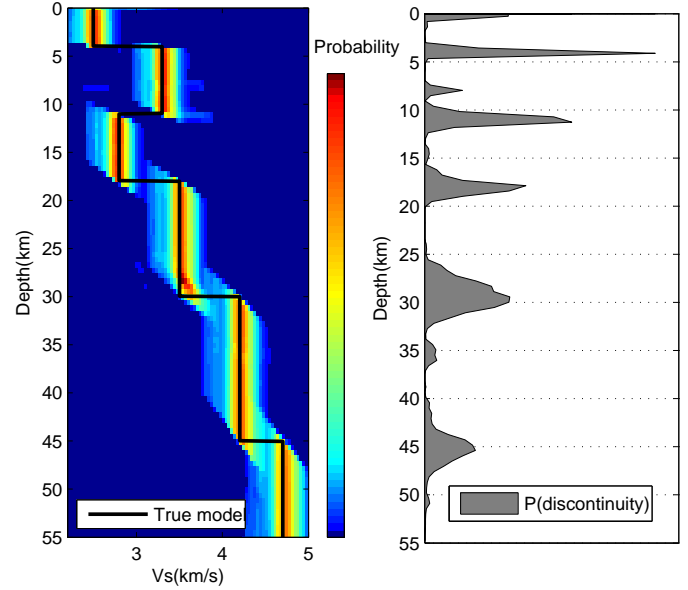


Figure 2.73: Seismograms in Figure 2.71 are inverted for a layered Vs model with an expanded Bayesian Inversion using cross-convolution. The solution is a large ensemble of 1D profiles representing the probability of the model given the data. Left: Probability for Vs at each depth. Right: probability of having a discontinuity at each depth. (For color figure, see http://earthquakes.berkeley.edu/annual_report/)

optimization based inversion, i.e. where one only seeks the maximum likelihood model, they become crucial in a Bayesian sampling framework. This is because uncertainty estimates do not affect the best fitting solution, or peak of the likelihood function, but strongly determine the shape (and width) of the likelihood function in model space. In this way, the cross-convolution misfit function enables us to carry out a proper Bayesian inversion which correctly propagates errors in the data toward model uncertainties (Figure 2.73). Data are taken as they are, with no need of arbitrarily defined stabilization parameters (i.e. water level, or width of Gaussian filters), which may bias the solution in a statistical sense.

34.4 References

- Di Bona, M. and others, Variance estimate in frequency-domain deconvolution for teleseismic receiver function computation, *GJI.*, 134, 2, 634-646, 1998
- Menke, W. and Levin, V., The cross-convolution method for interpreting SKS splitting observations, with application to one and two-layer anisotropic earth models, *GJI*, 154, 2, 379-392, 2003
- Vinnik, L.P., Detection of waves converted from P to SV in the mantle, *Phys. Earth and Plan. Int.*, 95 39-45, 15, 1977.

35 Surface-Wave Methods for Monitoring Subsurface Properties in Permafrost Soils

Shan Dou, Jonathan Ajo-Franklin (LBNL), and Douglas Dreger

35.1 Introduction

Permafrost (frozen ground that remains at or below 0°C for at least two consecutive years) covers 24% of northern circumpolar continents (Zhang *et al.* 1999). Thawing permafrost in a warming climate can cause hazards of serious concern: (1) Significant amounts of greenhouse gases can be released into the atmosphere due to large-scale microbial decomposition of organic matter that are previously preserved in frozen soils; (2) Thermokarst subsidence in ice-rich permafrost can further intensify the thaw of frozen ground as well as cause severe damage to infrastructure and transportation networks. Both incremental processes (e.g. active layer thickening and talik formation) and transient phenomena (e.g. thaw-induced ground surface settlement and slope instability) affect the rate of permafrost degradation and the detrimental impacts on climate change. Substantial amounts of supercooled water (liquid water that stays unfrozen below 0°C) exist in permafrost soils. Such unfrozen water not only enables carbon-related microbial activities even in subzero temperatures but also makes the subsurface water/ice content not directly predictable using only temperature information. All these aforementioned issues point to the necessity of permafrost monitoring in various spatial and temporal scales. Thermal monitoring in deep boreholes, despite being one of the most common monitoring approaches, only provides one-dimensional plot-scale measurements that do not directly indicate ground ice content. In addition, deep boreholes in permafrost are generally scarce because of the high cost and logistical difficulties, especially in remote Arctic and Subarctic regions. In contrast, geophysical monitoring methods can provide information on subsurface properties over field-scale areas (e.g. hundreds of meters laterally and vertically) at a comparatively low cost and with minimal disturbance to the natural environment. Geophysical monitoring approaches also have the potential for automated acquisition using permanent or semi-permanent sensor networks, a distinct advantage in regions that are difficult to access and in inhospitable environments.

Permafrost characterization and monitoring with geophysical methods relies on properties that differ between frozen and unfrozen materials. The most frequently used geophysical properties for studies of periglacial environments include *electrical resistivity*, *dielectric permittivity* and *seismic velocity*. Among other properties of frozen soils, *ground ice content* is a key factor when estimat-

ing risk level of environmental hazard in the context of global warming. Though electrical methods usually require less effort in data acquisition and processing, they often result in difficulties in differentiating between ice and air and are often limited to shallower targets. Seismic methods, on the other hand, do not suffer from such problems and thus are particularly suitable for assessing ground ice content, both as an independent method and a complementary approach to be combined with other geophysical monitoring techniques.

35.2 Methodologies

[1] **Permafrost Analysis Based on Surface Wave Methods (SWMs):** Seismic sources at a free-surface impart approximately 2/3 of the radiated energy to surface waves (Woods, 1968). Rich information is carried by the surface wave train owing to its geometric dispersion properties: Surface waves of different frequencies penetrate into different subsurface depth ranges and thus travel with different apparent velocities. Standard seismic equipment for reflection/refraction acquisitions can be directly used for gathering high quality surface wave data. The propagation of surface waves is primarily controlled by the soil shear velocity, thus potentially providing information on soil frame properties, including ice content as well as shear strength. For subsurface soil profiles that contain pronounced low velocity layers, both near-surface reflection and refraction approaches have limited application. Assuming a reasonable survey geometry, surface wave methods provide an attractive approach for characterizing low velocity layers, a category of structures which includes deep partially thawed regions of interest in permafrost environments.

[2] **Continuous Active Source Seismic Monitoring (CASSM):** Semi-permanently deployed seismic systems with fixed sources and receivers have recently been used in monitoring subsurface processes, including near-surface stress changes (Silver *et al.* 2007), subsurface movement of supercritical CO₂ (Daley *et al.* , 2007, 2011), hydrofracture initiation and propagation (Ajo-Franklin, *et al.*, 2011), and seismic velocity changes in fault zones prior to seismic activity (Niu *et al.* , 2008). This strategy, referred to as continuous active source seismic monitoring (CASSM), allows both high precision in detecting subtle changes and excellent temporal sampling on the order of minutes. CASSM systems, for the purpose of time-lapse seismic measurements, could help us gain an in-depth understanding of subsurface processes

in frozen soils that are both continuous and threshold-driven. Combining CASSM with Multichannel Analysis of Surface Waves (MASW) (e.g. *Park et al.*, 1999) could be a compelling direction for the development of permafrost monitoring systems.

35.3 Preliminary Results

[1] **Development of a Physics-based Four-phase Rock Physics Model:** Rock physics models, which link geophysical observables to microstructure and phase composition, are not only important for interpreting geophysical results but also provide a priori information (e.g. constraints) that is critical for the inverse problem itself. Frozen soils have four constituents: soil particles, ice, liquid water, and air. It is therefore most reasonable to include these four phases into the permafrost model. We selected contact cement theory (CCT) (*Dvorkin et al.*, 1994; *Dvorkin and Nur*, 1996; *Jacoby et al.*, 1996; *Dvorkin et al.*, 1999) to model characteristics of the grain-ice solid skeleton. and White’s patchy saturation model (*White*, 1975; *Dutta and Odé*, 1979a,b; *Dutta and Seriff*, 1979) to account for the effects of water and air. Figure 2.74 shows seismic velocities (predicted based on our rock physics model) as a function of time for Barrow, Alaska. The velocity variations correlate well with the soil temperature changes, and the effect of residual unfrozen water content is clearly visible at the freeze-thaw transition due to unfrozen waters held by fine-grained silty soils below 20 cm from the ground surface.

[2] **May 2012 Seismic Survey at Barrow, Alaska:** An active-source (sledge-hammer) seismic survey was conducted in early May of 2012 at Barrow, Alaska. The survey used 48 vertical 10 Hz geophones with 1.1 m spacing. Preliminary frequency-phase velocity (f-v) domain analyses along the seismic lines have shown strong presence of overtone energy, which could be indicative of the existence of low shear-velocity layers whose effects are dominant within the survey’s sensitivity range. However, the difficulties in identifying and separating the overtones have required adaptations in the inversion method used for analyzing the field data. The approach we are developing, a modeless MASW waveform inversion scheme, will hopefully provide a robust inversion approach for scenarios where the presence of overtones obscures picking for the fundamental Rayleigh mode.

[3] **Development of an MASW CASSM System:** Longer term deployments in the arctic, particularly those monitoring subtle diurnal or seasonal property variations, will require semi-permanent active source surface wave monitoring systems. We have initiated development of such a system based on a combination of a commodity electromechanical transducer and the CASSM acquisition infrastructure developed for borehole measurements (e.g. *Daley et al.*, 2007, *Ajo-Franklin et al.*, 2011). The system is currently being bench tested; we anticipate lo-

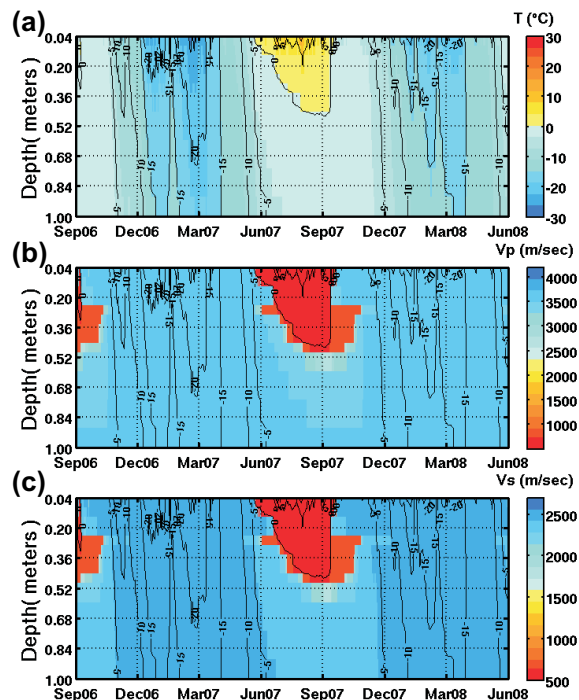


Figure 2.74: (a) Daily soil temperatures at Barrow for the period 09/01/2006 to 06/01/2008; (b) Predicted time-lapse variations of compressional wave velocities for the same time period; (c) Predicted time-lapse variations of shear wave velocities were calculated for the same time period.

cal field deployments in the next quarter followed by tests in the arctic in CY 2013.

35.4 Acknowledgements

This study is sponsored by the Office of Biological and Environmental Research within the U.S. Department of Energy’s Office of Science as part of the Next Generation Ecosystem Experiment (NGEE-Arctic).

35.5 References

Dvorkin, J., J. Berryman, and A. Nur, Elastic moduli of cemented sphere packs, *Mechanics of Materials*, 31, 461-469, 1999.

Ajo-Franklin, J., T. Daley, B. Butler-Veytia, J. Peterson, Y. Wu, B. Kelly, and S.S. Hubbard, Multi-level continuous active source seismic monitoring (ML-CASSM): Mapping shallow hydrofracture evolution at a TCE contaminated site, *SEG Expanded Abstract*, 30, 2011.

Daley, T. M., R.D. Solbau, J.B. Ajo-Franklin, and S.M. Benson, Continuous active-source seismic monitoring of CO2 injection in a brine aquifer, *Geophysics*, 72(5), A57-A61, 2007.

Park, C. B., R. D. Miller, and J. Xia, Multichannel analysis of surface waves, *Geophysics*, 64, 800-808, 1999.